UNIVERSITAT POLITÈCNICA DE CATALUNYA BARCELONATECH

Mixing and chemical reaction hotspots in saline-freshwater mixing zones

Kevin De Vriendt

DOCTORAL THESIS

Mixing and chemical reaction hotspots in saline-freshwater mixing zones

Author:
Kevin DE VRIENDT

Supervisor:
Dr. Marco DENTZ

Supervisor:
Dr. Maria POOL

Tutor:
Dr. Daniel FERNANDEZ

Institute of Enviromental Assessment and Water Research (IDAEA)

Spanish National Research Council (CSIC))

Department of Civil and Environmental Engineering, Program of Geotechnical Engineering, Universitat Politecnica de Catalunya (UPC)

This thesis was funded by the ENIGMA-ITN (European training Network for in situ imaging of dynamic processes in heterogeneous subsurface environments) program. ENIGMA ITN has received funding from European Union's Horizon 2020 research and innovation programme under the Marie Sklodowska-Curie Grant Agreement number 722028.

Abstract

Seawater intrusion presents one of the most unique and ubiquitous groundwater problems in the field of hydrogeology. Its complex boundary conditions coupled with variable density flow results in non-uniform flow which lead to non-trivial mixing dynamics. The mixing of fresh and saline waters in the subsurface is known to play a key role in an array of geochemical reactions. Such reactions include the dissolution and precipitation of calcite which shape the coastal landscape over millennia, as well as reactions associated to anthropogenic contamination of coastal groundwater such as nitrogen reduction or iron oxide precipitation which can act to limit the fluxes of harmful pollutants to vulnerable near shore marine ecosystems. In addition to reactions, understanding the mixing mechanisms is crucial to predicting the movement of the saltwater wedge and the size of the salt-freshwater interface. This has direct implications on the management of fresh groundwater reserves and its risk to salinization.

In this thesis we focus on understanding the influence variable density flow on mixing and the spatial distribution of enhanced geochemical activity along the saline-freshwater interface. First, we look to see the impact of heterogeneity on mixing and reaction for fast calcite dissolution. We find that heterogeneity permits reactions to occur over a greater area of the mixing zone due to enhanced mixing rates than would otherwise be permitted in homogeneous media. Furthermore, we observe unique patterns of enhanced localized reactivity that strongly deviate from the homogeneous case. Our study suggests that karst topology in coastal aquifers may be strongly linked to non-uniform flow induced by variable density flow and strongly linked to the type of heterogeneity present. Since initial stages of karst development are known to dictate the evolution of cave systems and conduits, we hypothesize that heterogeneity plays an integral role in its propagation. Second, we study mixing across the salt-freshwater interface and the influence of compression caused by the flow of freshwater towards the saltwater body. In the absence of transient effects and heterogeneity, we find that mixing interface grow via transverse dispersion until some critical distance at which point it begins to recompress due to accelerating flow resulting from a decrease in area between the confining unit and the interface. Using a modified Glover solution to define the mixing interface, we are able to capture the velocity change along the interface from which a stretching rate (acceleration) can be deduced. We find that the behaviour of interface compression can be well-approximated by assuming a local Bachelor scale, which defines the equilibrium between dispersive growth and compression due to accelerating flow. Finally, we establish a new method to study fast mixing-dependent reactions across the salt-freshwater interface. Our findings lead us to the use of luminol chemiluminescence, which allows for the direct visualization of reaction rates along the saline-freshwater interface. Unlike conservative studies of mixing in sand tank, we bypass the need for complex image analysis techniques required to resolve local concentration gradients needed to evaluate mixing metrics. Results from experiments performed under both steady state and transient conditions consistently confirm local reaction hotspots at both the interface toe and at the head of the interface, which

we attribute to stagnation point flow and accelerating flow respectively. Evaluation of the interface during the transient advance and retreat were also able to capture unique reactive behaviours that capture a shift in mixing behaviour due to a change in the flow field across the mixing zone.

Resumen

La intrusión de agua de mar presenta uno de los problemas más singulares y omnipresentes de aguas subterráneas en el campo de la hidrogeología. Sus complejas condiciones de contorno junto con un flujo de densidad variable dan como resultado un flujo irregular y, consecuentemente, provocando una dinámica de mezcla no trivial. La mezcla de agua dulce y salada en el subsuelo juega un papel clave en una serie de reacciones geoquímicas, tal como la disolución y precipitación de la calcita, que ha dado forma al paisaje costero durante milenios. También controla reacciones asociadas a la contaminación antropogénica de las aguas subterráneas costeras, tal como la reducción de nitrógeno o la precipitación de óxido de hierro,que pueden actuar para limitar los flujos de elementos contaminantes. Dichos elementos son nocivos para las zonas vulnerables cercanas a la costa, como los ecosistemas marinos. Además de las reacciones, comprender los mecanismos de mezcla es crucial para predecir el movimiento de la cuña de agua salada y el tamaño de la interfaz que separa el agua salada de la dulce. Esto tiene implicaciones directas en la gestión de las reservas de agua dulce subterránea y su riesgo de salinización.

En esta tesis nos enfocamos en comprender la influencia del flujo de densidad variable en el proceso de mezcla y la distribución espacial de la actividad geoquímica (mejorada) sobre la interfaz agua dulce y salada. Primero, buscamos ver el impacto de la heterogeneidad hidráulica en la mezcla y reacción para una rápida disolución de la calcita. Encontramos que tal heterogeneidad permite que se produzcan reacciones en un área mayor de la zona de mezcla debido a velocidades de mezcla mejoradas respecto de las que serían posibles en medios homogéneos. Además, observamos patrones únicos de reactividad localizada mejorada que se desvían fuertemente del caso homogéneo. Nuestro estudio sugiere que la topología kárstica en los acuíferos costeros puede estar fuertemente ligada a un flujo no uniforme inducido por un flujo de densidad variable y fuertemente vinculado al tipo de heterogeneidad presente. Dado que se sabe que las etapas iniciales del desarrollo kárstico dictan la evolución de los sistemas de cuevas y conductos, planteamos la hipótesis de que la heterogeneidad juega un papel integral en su propagación. En segundo lugar, estudiamos el proceso de mezcla que se da en la interfaz de agua dulce y salada y la influencia de la compresión causada por el flujo de agua dulce hacia el cuerpo de agua salada. En ausencia de efectos transitorios y heterogeneidad, encontramos que la interfaz de mezcla crece a través de la dispersión transversal hasta una distancia crítica en cuyo punto comienza a comprimirse, debido al flujo acelerado resultante de una disminución en el área entre la unidad confinante y la interfaz. Usando una solución Glover modificada para definir la interfaz de mezcla, podemos capturar el cambio de velocidad a lo largo de la interfaz de la cual se puede deducir una tasa de estiramiento (aceleración). Encontramos que el comportamiento de la compresión de la interfaz se puede aproximar bien asumiendo una escala de Bachelor local, que define el equilibrio entre el crecimiento dispersivo y la compresión debido al flujo acelerado. Finalmente, establecemos un nuevo método para estudiar reacciones rápidas dependientes de la mezcla a través de la interfaz sal-agua dulce.

Nuestros hallazgos nos llevan al uso de quimioluminiscencia de luminol, que permite la visualización directa de la distribución espacial de la tasa de reacción a lo largo de la interfaz agua dulce-salada. A diferencia de la práctica más habitual en estudios de mezcla en tanques de arena, que típicamente utilizan trazadores no reactivos, evitamos aquí la necesidad de resolver gradientes de concentración para computar métricas de mezcla. Los resultados de los experimentos, realizados tanto en condiciones estacionarias como transitorias, confirman consistentemente la generación de puntos calientes de reacción local, tanto en la cuña como en la cabeza de la interfaz, que atribuimos al estancamiento y aceleración del flujo, respectivamente. La evaluación de la interfaz durante el avance y retroceso transitorio también pudo capturar comportamientos reactivos únicos que capturan un cambio en el comportamiento de mezcla debido a un cambio en el campo de flujo a través de la zona de mezcla.

Acknowledgements

I would firstly like to thank my both my supervisors Dr. Marco Dentz and Dr. Maria Pool for supporting and guiding me through out the duration of my PhD. They have with great patience, helped me through all aspects my research and for that I am extremely grateful.

I would also like to express my sincere gratitude to all the people in Rennes during my secondment. I would especially like to thank Dr. Tanguy Le Borgne, Dr. Joris Heyman and Dr. Yves Meheust for providing me with the space and expertise to carry out my experiments. They were all a great source of inspiration and always there to guide and engage in thoughtful discussion especially after many failed experiments. The lab experience would also not have been complete without the presence of fellow experimentalists, Dr. Jayabratah Dhar, Dr. Satoshi Izumoto and Alejandro Fernandez. During our time in the lab together we both suffered and enjoyed each others successes together.

A big thank you to all the students and members of the ENIGMA-ITN group which made the PhD experience that much more fun. My experience in Spain was also incomplete without Alec and Tomas who were always there for me to talk to. I am also very thankful to Dr. Juan Hidalgo who always had his door open for any issues I came across. I also greatly appreciate Dr. Juan Hidalgo and Dr. Aronne Dell'Oca for taking the time to review my thesis. I would also like to extend my gratitude to Dr. Niklas Linde for supervising me during my time in Lausanne. Although this was cut short due to the Corona virus, it was a pleasure to have had the opportunity to visit UNIL.

Of course, none of my success would be possible without the loving support and encouragement from all my family to whom I am eternally grateful. Most of all I am indebted to my Fiancée Ezgi for putting up with me through the duration of my PhD. Thank you for being so patient and looking out for me all along the way.

Contents

List of Figures

List of Tables

CHAPTER 1

Introduction

1.1 Motivation

Seawater intrusion and the subsequent mixing between terrestrial freshwater and seawater is a problem ubiquitous to all coastal landscapes. Due to the importance of mixing and reactions that take place across the salt-freshwater interface (SFI), it commonly referred to as a 'subterranean estuary'; a reference to the fact that they possess fundamental features found in surface estuaries where mixed waters and local aquifer solids can significantly alter the compositions of fluids (Moore, 1999). Previous studies have shown that discharging coastal groundwater may strongly impact ocean nutrient dynamics, thus having the propensity to negatively impact delicate marine ecosystems (e.g. Amato et al., 2016; Lee and Kim, 2007; LaRoche et al., 1997). This comes as no surprise considering coastal plains are some of the most densely populated regions across the globe, accommodating up to 70 % of the worlds population (Jones et al., 1999) and 75% of the worlds megacities (Alencar et al., 2020) . Not only does seawater intrusion risk the degradation of potable drinking water that many coastal cities rely on, but the proximity of industries and agricultural practices results in large fluxes of pollutants into vulnerable coastal aquifers and ultimately fragile ocean ecosystems (Moore, 1999; Valiela et al., 1990).

Studies have found that nutrient concentrations in some coastal ground waters can be over several orders of magnitude greater than in surface waters (Moore, 1999). Along the South Atlantic Bight, for example, fluxes from submarine groundwater discharge (SGD), the flow of water from the seabed to the coastal ocean was found to be over three times larger than that of river discharge (Moore, 2010). These fluxes have been thought to be related to eutrophication (Valiela et al., 1990) and the initiation of algal blooms (LaRoche et al., 1997). While this thesis does not investigate the behaviour of SGD and its influence on marine geochemistry directly, the mixing of geochemically distinct water compositions and the unique flow behaviour along the SFI, has a direct influence of the fate of nutrients of which we are concerned.

The mixing zone has also been attributed to strong geochemical reactions which influence coastal geochemistry as well as the geological landscape. Over larger timescales, the mixing of salt and freshwater end-member compositions has been attributed to the large-scale dissolution features as observed in the Yucatan Peninsula (Back et al., 1979; Back et al., 1986a) and Bahamas (Palmer and Williams, 1982; Mylroie and Carew, 1990). Numerical studies investigating this phenomena have further evidenced the formation of dissolution hotspots resulting from end-member mixing and non-trivial interplay between geochemistry and transport (Rezaei et al., 2005). In many groundwater systems, complex flow patterns induced by heterogeneities or non-trivial boundary conditions can strongly influence the topology of reactive interface which impacts the behaviour and intensity of mixing and subsequently the

reaction dynamics. Interface deformation has been shown to dominate reactive dissolution in convective flow(Hidalgo et al., 2015; Hidalgo and Dentz, 2018) as well as hyporeic zones and hill slopes (Bandopadhyay et al., 2018). A range of other non-uniform geophysical flows, ranging from radial flow to random stratified flow have also been shown to lead to enhanced mixing-induced chemical reaction (Le Borgne et al., 2014). While a direct solution for seawater intrusion problem does not exist, understanding how non-uniform flow impacts mixing and reactions may help elucidate fundamental mechanisms that control geochemical reactions across the salt-freshwater interface. The following section summarizes the state of art regarding mixing and reactions across the salt-freshwater interface. A detailed state of the art is also provided in the introduction of each chapter for the given topic.

1.2 State of Art

Mixing between fresh and salt-water is a fundamental precursor towards understanding seawater intrusion and managing coastal groundwater resources. It is the mixing of variable density fluids via diffusion and mechanical dispersion that ultimately dictates the behaviour of the SFI and the discharge of mixed waters towards the ocean bed. Consequently, substantial effort has been given to understanding the mechanisms that control the extent of mixing across this interface. These processes are of particular interest as mixing zones in real coastal aquifers have been found to vary substantially, ranging from several meters to kilometres (Kroeger and Charette, 2008; Spiteri et al., 2008a; Kim et al., 2007; Price et al., 2003; Langevin, 2003; Barlow, 2003). In contrast, experimental sand-tank studies consistently show very thin mixing zones (e.g., Abarca et al., 2007; Goswami and Clement, 2007; Robinson et al., 2015; Yoshihiro Oda, Tamio Takasu, Hirashi Sato, Atsushi Sawada, 2010).

In order to adequately characterize the geometry, extent and degree of mixing of the SFI under steady-state homogeneous conditions, it is important to consider several key parameters; the relative density of fluids, the groundwater flux and components of the dispersion tensor (Volker and Rushton, 1982). Due to the coupled nature between flow and transport, a change in one these parameters will alter the characteristics of the salt-freshwater interface. To provide a general intuition for the nature of this problem, consider a scenario where local dispersion in the aquifer is increased. The result is a widening of the mixing zone, thus reducing density contrasts which control the rotation of the salt-water wedge thereby resulting in a seaward retreat of the wedge (Kerrou and Renard, 2010).

As previously stated, the extent of mixing across the SFI, for which we are particularly concerned, is dictated by hydrodynamic dispersion. Since flow across the SFI is dominantly orientated along the interface, under steady-state and homogeneous porous media, transverse dispersion is the dominant mechanism controlling the width of the mixing zone (Held et al., 2005; Paster and Dagan, 2007). This is suggested to be the primary reason for the observation of narrow mixing widths in experimental sand-tanks (e.g. Abarca and Clement, 2009; Goswami and Clement, 2007; Yoshihiro Oda, Tamio Takasu, Hirashi Sato, Atsushi Sawada, 2010; Robinson et al., 2016; Masahiro et al., 2018) where transverse dispersivities are typically very small. Narrow mixing zones have also been observed in a number of geological settings such as karsts (Yarkon-Taninim aquifer, Israel) (Paster, 2010), volcanic rocks (Jeju Island, Korea) (Kim et al., 2007) and alluvial sediments (Waquiot Bay, USA) (Spiteri et al., 2008a). Previous studies investigating the role of transverse dispersion across

multiple scales have typically found that transverse dispersivity is not strongly impacted by scale or heterogeneity (Fiori and Dagan, 1999; Klenk and Grathwohl, 2002; Olsson and Grathwohl, 2007; Prommer et al., 2002), which would explain thin mixing zones found in the field. Numerical simulations by Abarca et al. (2007); however, found that longitudinal dispersivity played an equally important role in the average interface thickness and was directly related to the geometric mean of transverse and longitudinal dispersivities. Their study found that transverse dispersivity generally acts to broaden the entire interface and an increase in longitudinal dispersivity shifts high concentration isolines seaward. Despite the importance of dispersivities in predicting the width of the SFI, there is still no clear criterion to assigning these values in the context of seawater intrusion (Rezaei et al., 2005). In many instances, the values adopted in steady-state numerical studies can be arbitrarily large in order to reduce numerical dispersion (Paster, 2010) or to artificially incorporate the effects of geological heterogeneity and transient hydraulic processes. All things considered, it is generally understood that local dispersion alone is not responsible for very wide mixing zones observed in some field settings (Werner et al., 2012). In order explain this phenomena, studies have looked into a range of coastal processes.

The influence of tides in confined aquifers for example, has been shown to increase the extent of the transition zone, specifically for large storage coefficients (Inouchi et al., 1990). Pool et al. (2014) similarly showed that tidal effects in confined aquifer is dictated by the tidal mixing number, which depends on the tidal amplitude, period and hydraulic diffusivity. In general, they showed that tides have the strongest effect for large values of storativity which causes a strong non-uniform hydraulic response. Their study also noted that this response is only valid for the dispersive case, and would not occur if mixing is represented by a constant dispersion coefficient. In contrast, numerical studies looking at unconfined aquifers by Ataie-Ashtiani et al. (1999), found little change in the size of the SFI in response to tidal action. Lu et al. (2009b), incorporated the effects of kinetic mass transfer in addition to tidal oscillation which resulted in significantly wider mixing zones. This was attributed to the unsynchronized behaviour of concentration distributions between mobile and immobile domains (Lu and Luo, 2010). The movement of the SFI back and forth has also been shown to result in the changing of flow directions. When intruding, fresh and salt water flow originate from their boundaries in opposite directions before redirecting across the interface , with a stagnation point located at the toe (Chang and Clement, 2012a). As the wedge recedes, the flow vectors flip landward until a new steady state is achieved, at which point the convection cell is re-established. While the implications of this have not directly been discussed with respect to mixing behaviour, an experimental study by Robinson et al. (2015) and Abdoulhalik and Ahmed (2018) have shown that the average mixing width show a marked increase during recession, and negligible change during intrusion. Despite a large body of literature dedicated to using experimental sand tanks to further our understanding of seawater intrusion, there are no experiments that look into how such movements would influence reactive mixing across the SFI.

There has also been growing attention focused on the influence of tidal action in unconfined aquifers which lead to an upper saline plume within the intertidal zone (Heiss et al., 2017; Liu et al., 2017; Xin et al., 2015; Xiaolong Geng, James W. Heiss, Holly A. Michael, 2017; Abarca et al., 2013). This zone incorporates additional layers of complexity as it involves additional processes such as wave run up, and unsaturated flow dynamics. While this aspect of salt-freshwater mixing has an important

role in describing coastal nutrient dynamics and biogeochemical cycling, in this thesis we focus on mixing across the main salt-water body.

The influence of heterogeneity in the form of random permeability fields, has also been shown to consistently result in wider mixing zones and a recession of the saltwater wedge and for both the diffusive (Henry problem) and dispersive case. In 3D numerical simulations however, Kerrou and Renard (2010) showed that an increase in the degree of heterogeneity results in the toe to penetrate further landward. This has been attributed to the impact of statistical anisotropy on the effective hydraulic conductivity. Using homogenization theory, Held et al. (2005), found that for the Henry problem, the effective dispersion coefficients from equivalent homogeneous mediums were sufficient to describe the behaviour in heterogeneous permeability fields. Abarca (2006) similarly found that for the dispersive problem under moderate heterogeneity, effective dispersion for seawater intrusion in heterogeneous media is close to the value of local dispersion. Larger scale heterogeneities such as geological stratification have also been shown to widen mixing zones. Lu et al. (2013), for example showed both experimentally and numerically that a low hydraulic conductivity layer between an upper and lower high conductivity layer will result in a considerable increase in mixing width in the middle layer. While an abundance of studies have focused on role of heterogeneity in widening the SFI, there are still no studies investigating the its role in reactive-mixing.

As aforementioned, mixing hotspots resulting from the mixing of geochemically distinct water compositions has been found to result in dissolution hotspots along the interface (Sanford and Konikow, 1989; Rezaei et al., 2005). These studies provide important insight into the non-trivial interplay between chemistry and transport, highlighting the fact that one-dimensional mixing model alone cannot predict reactive hotspots in heterogeneous flow fields. While their results shed light on the importance of mixing-induced reactions in explaining carbonate dissolution in homogeneous media, little is known for these processes under spatial heterogeneity.

The significance of heterogeneous flow on mixing and reactions have been highlighted in a growing number of studies. At the field scale, non-uniform flow can arise from large scale geological heterogeneities (e.g. fractures and sedimentary layers) as well as complex boundary conditions. The resulting flow fields can result in strong stretching and compression of mixing fronts resulting from strong velocity gradients and streamline topology (Rolle and Le Borgne, 2019). In such cases, mixing is enhanced by increasing the surface area available for diffusive mass transfer (Ottino, 1989). A notable example of such a behaviour is the flow focusing which was investigated by Werth et al. (2006). The convergence of streamlines entering high permeability inclusions resulted in increased transverse mass transfer between streamlines which was found to enhanced mixing and reaction. In an investigation of mixing dynamics in hyporheic zones and hillslopes, Bandopadhyay et al. (2018) also found that streamline patterns result in shear flow which can lead to transient mixing hotspots and an overall acceleration of mixing dynamics within flow cells. A range of heterogeneous flow scenarios from ranging radial flow to stratified random flow and their influence on mixing induced reaction have also been evaluated by Le Borgne et al. (2014). In this thesis we use these concepts and methods to shed light on mixing and reaction coastal aquifer.

1.3 Objectives

Main Objective The main objective of this thesis is to investigate mixing dynamics across the salt-freshwater interface and elucidate processes that lead to chemical reaction hotspots.

Despite an extensive body of literature aimed towards understanding seawater intrusion, the assessment of mixing dynamics across the salt-freshwater interface and its influence over chemical reactions remains a largely open area of study. In order to develop new insight to these processes, we set the following specific objectives for this thesis.

1. to illustrate the influence of different types of heterogeneity on mixing and reactions across the salt-freshwater interface;
2. to quantify the behaviour of mixing along the salt-freshwater interface in response to non-uniform flow;
3. to develop an experimental method that can be used to visualize fast mixing-limited reactions across fluid interfaces
4. to implement the experimental method obtained from the previous point to describe reactive-mixing during seawater intrusion.

1.4 Thesis Outline

- In Chapter 2, we outline the basic principles surrounding seawater intrusion and the general flow and mixing dynamics that manifest in coastal aquifers under variable density flow. We also introduce basic concepts pertaining to conservative and reactive transport and the metrics and methods commonly used to quantify their behaviour
- In Chapter 3, we cover objective 1. Here, we study the impact of mixing and calcite dissolution across the salt-freshwater interface in heterogeneous media. In this chapter we look at how heterogeneity can strongly affect local and global mixing patterns which manifest in dissolution hotspots. Here, we gain some general insight into the complex nature of karstic systems observed in coastal carbonate systems.
- In Chapter 4, we cover objective 2. In doing so, we take a step back and investigate the mixing behaviour across the salt-freshwater interface under steady-state homogeneous conditions. We analyse the local mixing behaviour along the length of the interface in an attempt to further understand the mixing dynamics that may result in localised reaction hot spots across the interface. To do so, we evaluate the mixing width from the interface toe to the head and examine how changes in flow influences local mixing processes.
- In Chapter 5, we cover objective 3. we present a chemical reaction that can be used to probe reactive mixing across mixing interfaces.
- In Chapter 6, we implement the reaction developed in chapter 5 in a milifluidic cell to investigate reactive-mixing across a stagnation point. We compare results obtained from these experiments to scaling laws derived using the reactive lamella approach.

- In Chapter 7, we cover objective 4. To do so, we use the methodology described in chapter 5 to investigate the reactive mixing across the salt-freshwater interface in response to different hydraulic head gradients. We also investigate the reactive behaviour during seawater intrusion and retreat.
- In Chapter 8 we provide general conclusions to the thesis with some perspectives for future work

CHAPTER 2

Basics

2.1 Variable Density Flow

Variable density flows in porous media appear across a broad range of environmental problems. Understanding the behaviour of fluids with different densities are paramount to describing many groundwater contamination problems such as radioactive waste disposal, leaching of contaminants in landfills, agricultural irrigation as well as geothermal energy to name a few (Simmons et al., 2001). Naturally, the source of density variations may be either anthropogenic or naturally induced. In the shallow subsurface, density differences typically arise from pollution of non-aqueous phase fluids or variations in salinity. At greater depths, density differences are typically induced by changes in pressure or temperature (Holzbecher, 1998). In conditions where a denser fluid overlies a lighter fluid (unstable stratification), instabilities may arise resulting in the formation of cells, columnar plumes or fingers (Simmons et al., 2002; Wooding et al., 1997; Hidalgo and Dentz, 2018). Free convection in this scenario can strongly enhance hydrodynamic mixing (Hidalgo and Dentz, 2018). In the opposite case, where a lighter fluid over lies a denser one, we have stable flow as is the case for seawater intrusion. In this scenario mixing is controlled by diffusive and dispersive mechanisms (Cooper, 1959). This thesis is focused around variable density flow as it pertains to the seawater intrusion problem.

2.2 Seawater Intrusion

Under scenarios where the mixing zone is very narrow relative the the overlying freshwater body, the interface has commonly be approximated by a sharp interface. In such cases, the steady state interface is reduced to a stagnant saltwater body and with only freshwater flow considered. One of the most commonly known analytical models for the sharp interface is based on the Ghijben-Herzberg principle. This principal relies on the Dupuit assumption, that considers vertical flow negligible. Practically speaking, this renders the 2D problem into a one dimension flow problem (Jiao and Post, 2019). Since we assume the saltwater body is stagnant, the saltwater head below the interface remains constant and equal to the sea level. Where the two waters meet, their water pressures must therefore also be equal. The depth to the interface from sea level can therefore be given as,

$$z = \frac{\rho_f}{\rho_s - \rho_f} h_f, \tag{2.1}$$

where ρ_f and ρ_s are the fresh and salt water densities respectively and h_f is the fresh water head. Given classical values of fresh and seawater densities of 1000 and 1025 kg/m^3 respectively, this yields the typical approximate,

$$z = 40h_f. \tag{2.2}$$

Another common analytical approach is that from Strack (1976), which uses a single potential function for confined and unconfined flow. This method provides the exact solution for Dupuit interface flow and is particularly attractive as the potential function can be written as one expression as a function of the horizontal coordinates. While sharp interface approximations have proven an efficient tool in many groundwater studies, many problems necessitate knowledge about the transition zone. Considering that even 1% salt water renders freshwater undrinkable, from a groundwater management perspective, sharp interface solutions do not offer conservative predictions for salt-water intrusion. Although a number of solutions exist that incorporate interface mixing, they are typically limited in use, e.g, the boundary layer approximation by Paster and Dagan (2007) considers high Pèclet flows ($Pe = b/\alpha_t >> 1$), where the width is assumed to controlled only by transverse pore-scale mixing, resulting in a very narrow transition zone. Henry (1964) had also provided a solution for variable density flow under steady state conditions, famously dubbed 'The Henry Problem'. While this solution has been particularly useful for numerical bench marking it provides little utility as it does not incorporate dispersion, which is typically required for an adequate characterization of the interface (Abarca et al., 2007). To overcome these limitations, numerical models are typically employed in order to describe seawater intrusion. In the following we present the problem formulation for steady state flow and transport,

We describe flow in porous media using the Darcy equation,

$$\mathbf{q}(\mathbf{x}) = -\mathbf{K}(\mathbf{x})\Big(\nabla p(\mathbf{x}) + \rho(\mathbf{x})g\mathbf{e_z}\Big), \tag{2.3}$$

where $\mathbf{q}(\mathbf{x})$ is the fluid flux, $\mathbf{K}$ is the hydraulic conductivity, $p(\mathbf{x})$ is the fluid pressure, g is gravitational acceleration, $\rho(\mathbf{x})$ is the fluid density which is a function of the fluid concentration and $\mathbf{e_z}$ denotes the unit vector in the vertical direction. Under steady state conditions in the absence of sources or sinks, fluid continuity is given by,

$$\nabla \cdot \rho(\mathbf{x})\mathbf{q}(\mathbf{x}) = 0. \tag{2.4}$$

The fluid density, $\rho(\mathbf{x})$ is a function of the salt concentration, $c(\mathbf{x})$ and is typically represented by the linear relationship below,

$$\rho(\mathbf{x}) = \rho_f\left(1 + \epsilon\frac{c(\mathbf{x})}{c_s}\right), \tag{2.5}$$

where c_s is the concentration of salt in sea water and ϵ is the relative density contrast between salt and freshwater, also commonly referred to as the buoyancy factor,

$$\epsilon = \frac{\rho_s - \rho_f}{\rho_f}. \tag{2.6}$$

While we often simplify the density of fluids as being a function of their salinity, it is also influenced by temperature variations which in turn also influences viscosity.

In this thesis, the influence of these factors are neglected in order to simplify the problems being investigated. The transport of salt is described by the steady-state advection dispersion equation,

$$\mathbf{q}(\mathbf{x})\nabla c(\mathbf{x}) - \nabla(\mathbf{D}(\mathbf{x}) + \phi D_m \mathbf{I})\nabla c(\mathbf{x}) = 0. \tag{2.7}$$

Here $\mathbf{D}(\mathbf{x})$ represents the dispersion tensor, D_m is the molecular diffusion coefficient, ϕ is the porosity and $\mathbf{I}$ is the identity matrix. Under isotropic conditions, the components of the dispersion tensor can be given by [Bear 1972],

$$\mathbf{D}_{i,j} = \partial_{i,j}\alpha_T + (\alpha_L - \alpha_T)\frac{q_i q_j}{|q|}, \quad i,j = x,y,z, \tag{2.8}$$

where $\partial_{i,j}$ is the Kronecker delta, α_L and α_T are the longitudinal and transverse dispersivities respectively. These governing equations are commonly reformulated in equivalent freshwater hydraulic head,

$$h_f(\mathbf{x}) = \frac{p(\mathbf{x})}{\rho_f g} + z. \tag{2.9}$$

Substituting equations (2.9) and (2.5) into (2.3) gives Darcy equation into terms of the equivalent freshwater head,

$$\mathbf{q}(\mathbf{x}) = -\mathbf{K}(\mathbf{x})\left(\nabla h_f(\mathbf{x}) + \mathbf{e_z}\frac{\rho(\mathbf{x}) - \rho_0}{\rho_0}\right). \tag{2.10}$$

Given that the direction of flow under steady state conditions is almost orthogonal to the density gradient we can make use of the Oberbeck-boussinesq approximation and equation (2.4) becomes,

$$\nabla \cdot u = 0. \tag{2.11}$$

Substituting equations (2.4) and (2.10) into (2.7) we can transform the steady-state transport equation in terms of the freshwater head (Dentz et al., 2006),

$$\mathbf{K}(\mathbf{x})\nabla h_f(\mathbf{x}) \cdot \nabla c(\mathbf{x}) + \mathbf{K}(\mathbf{x})\frac{c(\mathbf{x})}{c_s}\frac{\partial c(\mathbf{x})}{\partial z} + \nabla(\mathbf{D}(\mathbf{x}) + \phi D_m \mathbf{I})\nabla c(\mathbf{x}). \tag{2.12}$$

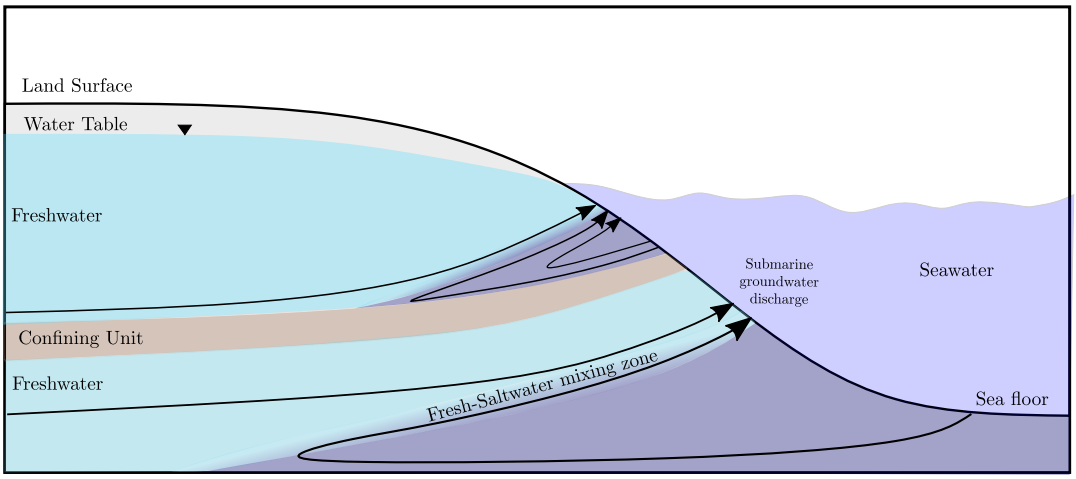

FIGURE 2.2.1: Conceptual schematic of seawater intrusion and it's common features, modified from Swarzenski et al. (2004)

.

2.3 Mixing dynamics and mixing controlled reactions

In the context of seawater intrusion, mixing generally refers to the blending of fresh and brackish water in coastal aquifers. The quantification of the size of the SFI is of particular importance as it pertains directly to the management of groundwater resources and dictates the risk of groundwater contamination (salinization of fresh groundwater). From a hydrogeochemical standpoint, understanding the blending of geochemically distinct water compositions plays a vital role in describing chemical reactions as it brings initially segregated species into contact. In order to predict where and how quickly reactions take place is however a challenging task due to the presence of non-uniform flow that is inherent in porous media flows. This is further complicated when considering the spatial and temporal scales over which mixing and reactions take place (Valocchi et al., 2018; Rolle and Le Borgne, 2019).

In the following we summarize typical geophysical flows and mixing mechanisms that influence mixing-limited reactions that can be applied to both pore scale and Darcy scale flows and the typical methods used in order to quantify their behaviour.

2.3.1 Mixing Mechanisms

In order to understand reactive transport of solutes in porous media, it is crucial to have a good understanding of the mixing processes involved. It is well known that non-uniform flows in the subsurface resulting from either geological heterogeneity or complex boundary conditions can strongly influence the nature of mixing (Le Borgne et al., 2014; Bandopadhyay et al., 2018; Engdahl et al., 2014). Flow patterns such as those depicted in Figure 2.3.1 can lead to considerable flow deformation which have been attributed to enhanced mixing of solutes. For completeness we first briefly discuss mixing at the pore-scale followed by how typical flow patterns that are known to influence mixing in Darcy scale flows.

At the pore-scale, mixing is influenced by a range of factors including the pore size distribution, grain geometry and orientation which can lead to unique streamline topologies and velocity distributions (de Anna et al., 2013b; de Anna et al., 2014; Jiménez-Martínez et al., 2017; Willingham et al., 2008; Kang et al., 2014), which an

be linked back to elementary flow patterns presented in Figure 2.3.1. Mixing at this scale consequently leads to poor mixing of solutes where patterns such as fingering can develop (de Anna et al., 2013b; Jiménez-Martínez et al., 2017). These finger patterns lead to elongation of mixing fronts which can enhance the rate of mixing by increasing the area over which diffusive mass transfer occurs while also intensifying concentration gradients (Ottino, 1989; Le Borgne et al., 2014; Villermaux, 2019). The consequence of such mixing patterns results in incomplete mixing at the pore scale. This has been attributed to a reduction in reaction efficiency compared to that predicted by Fickian descriptions of dispersion which assume well-mixed conditions (Gramling et al., 2002; Jose and Cirpka, 2004).Here, we focus on how non-uniform flow impacts mixing at the Darcy scale.

Flow patterns described in Figure 2.3.1 are ubiquitous in many subsurface flow problems. Shear flow (Figure 2.3.1a), describes velocity gradients transverse to the main direction of flow. At the pore-scale, shear results due to large velocity gradients adjacent to fluid-solid interface (de Anna et al., 2013b). In Darcy scale flow, this type of flow deformation can result from geological stratification (Bolster et al., 2011) as well as due to non-uniform boundary conditions such as found in hyporheic zones and hillslopes (Tóth, 2009), resulting in differential flow between streamlines. The latter has been found to accelerate mixing dynamics and generate transient mixing hotspots (Bandopadhyay et al., 2018). Flow focusing and defocusing occurs in heterogeneous porous media which forces streamlines to converge in higher permeability lenses. This impacts mixing by reducing the residence time within these inclusions and also decreases the distance between streamlines allowing for increased mass transfer to occur (Werth et al., 2006; Rolle et al., 2009). Stagnation point flow (Figure 2.3.1c), resulting in exponential compression of mixing interfaces has also been shown to play an important role in describing mixing and calcite dissolution in convective flow patterns (Hidalgo et al., 2015; Hidalgo and Dentz, 2018). More recent experimental investigations in Hele-shaw and porous media by Izumoto (2021) have also confirmed the influence of stagnation points in enhancing mixing and reaction. In more complex heterogeneous formations within 3-D systems, streamlines can also exhibit twisting as well as other complex topologies (Rolle and Le Borgne, 2019). Twisting streamlines have been evidenced experimentally (Ye et al., 2015) which result in considerable enhancement in mixing. While not exhaustive these few examples demonstrate the variability of flows that exist in field settings which may drastically influence mixing dynamics.

2.3.2 Quantification of Mixing

There are a number of different metrics that have been proposed to quantify subsurface mixing and reaction dynamics which include: the dilution index proposed by Kitanidis (2005); the concentration variance (Kapoor and Kitanidis, 1998) and the mixing rate otherwise known as the scalar dissipation rate (Pope, 2000). In this thesis we focus principally on the evaluation of the latter. For a passive scalar this is given by,

$$\chi(\mathbf{x}) = \nabla c(\mathbf{x}) \cdot [\mathbf{D}(\mathbf{x}) + \phi D_m] \nabla c(\mathbf{x}). \tag{2.13}$$

Physically speaking, this represents elementary mass transfer mechanisms distinguished by the creation of concentration gradients and their attenuation by diffusion (Le Borgne et al., 2014). This metric is of particular interest as it is intrinsically related to the reaction rate in fast equilibrium reactions (De Simoni et al., 2007).

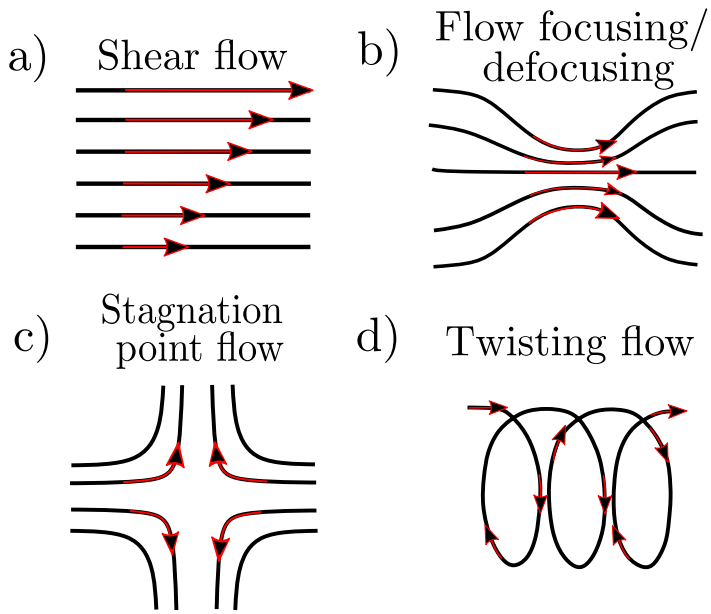

FIGURE 2.3.1: Examples of typical flow patterns in porous media and their resulting streamlines including: a) shear flow, b) flow focusing and defocusing c) stagnation point flow and d) twisting flow (Adapted from (Rolle and Le Borgne, 2019)

.

2.3.2.1 Lamella theory

This technique allows one to quantify how the local flow deformation alters the evolution of the concentration field. A typical example to illustrate this concept is provided in Figure 2.3.2. Here, the invasion of a solute through a stratified medium results in local shear that strongly deforms the mixing front into a collection of independent lamellae. This method quantifies mixing using the Lagrangian framework where transport of a solute is considered in the coordinate system attached to a material fluid element.

In this framework we neglect concentration gradients in the stretching direction, z since they are much smaller then in the perpendicular direction, n where compression is dominant. The advection dispersion equation written in this coordinate system is given by Ranz (1979),

$$\phi \frac{\partial c(n,t)}{\partial t} - \gamma(t) n \frac{\partial c(n,t)}{\partial n} - D \frac{\partial^2 c(n,t)}{\partial n^2} = 0, \tag{2.14}$$

where D is the local dispersion coefficient, ϕ is the porosity and γ is the stretching rate, which is defined in terms of the lamella elongation as,

$$\gamma = \frac{1}{\rho} \frac{d\rho}{dt}, \tag{2.15}$$

where ρ is the relative lamella elongation, $\rho = l/l_0$; l_0 being the initial lamella length and l the current. The evolution of the lamella width, s can also be determined via the centred second moment of $c(n,t)$ given by,

$$g(t) = \frac{\int dz z^2 c(n,t)}{\int dz c(n,t)}. \tag{2.16}$$

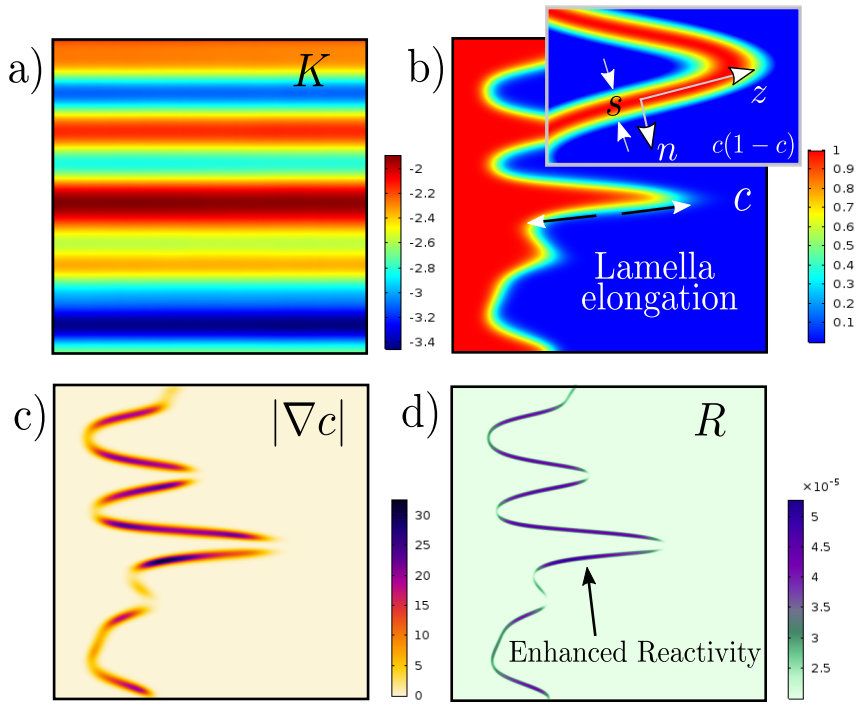

FIGURE 2.3.2: Reaction along mixing interface in stratified random flow. Image adapted from (Le Borgne et al., 2014)

.

After setting the lamella width $s = \sqrt{g(t)}$ into (2.14) we are left with the equation for the evolution of the mixing scale (Villermaux and Duplat, 2006),

$$\frac{1}{s(t)}\frac{ds(t)}{dt} = -\gamma(t) + \frac{D}{s(t)}, \tag{2.17}$$

which efficiently describes the interplay between advective compression and diffusive expansion (Villermaux, 2012; Le Borgne et al., 2015). For a constant compression rate, which is characteristic to flow toward a stagnation point, the mixing width decays exponentially fast towards the Batchelor scale (Batchelor, 1959),

$$s_b = \sqrt{D/\gamma}. \tag{2.18}$$

For an initial Guassian concentration profile with an initial concentration c_0, has the solution (Le Borgne et al., 2013),

$$c(n,t) = \frac{c_0 exp\left[\frac{z^2\rho(t)^2}{s_0^2(1+4\tau(t)}\right]}{\sqrt{1+4\tau(t)}}, \tag{2.19}$$

where $\tau(t)$ is the warped time defined by,

$$\tau = \frac{D}{\phi s_0^2}\int_0^t dt'\rho(t')^2. \tag{2.20}$$

For the maximum lamella concentration c_m, found along the interface center ($n = 0$), this reduces to,

$$c_m(t) = \frac{c_0}{\sqrt{1+4\tau(t)}}. \tag{2.21}$$

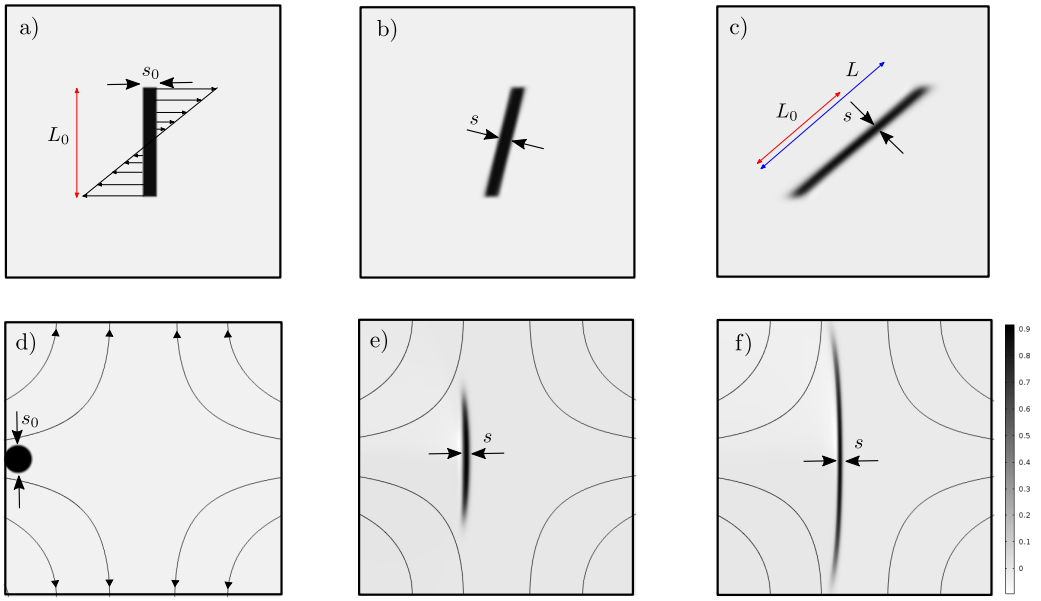

FIGURE 2.3.3: a-c) Simulation of a lamella with an initial length, L_0 and initial width, s_0 undergoing advection and diffusion in a laminar shear flow. d-f) Solute blob advecting and diffusing in a saddle point flow

.

In the following we illustrate the effect of linear stretching, resulting from shear (see Figure 2.3.2). The elongation rate and warped time becomes,

$$\rho(t) = \frac{s_0}{\sqrt{1+\gamma^2 t^2}}, \tag{2.22}$$

$$\tau(t) = \frac{D}{s_0^2}\left(t + \frac{1}{3}\gamma^2 t^3\right). \tag{2.23}$$

We therefore have an elongation rate that grows as $\rho \sim t$, and consequently $\tau(t) \sim t^3$. Inserting this into the expression for concentration maximum, we attain a decay following $c_m(t) \sim t^{-3/2}$. Note that in the case of diffusion in the absence of fluid stretching, $\gamma = 0$ and $\rho = 1$. The warped time therefore simplifies to $\tau(t) = (D/s_0^2)t$ leading to $c_m(t) \sim s_0/\sqrt{Dt}$. In this simple case, it is clear that shear flow can strongly enhance mixing by stretching the interface, thereby enhancing concentration gradients and increasing the area available for diffusive mass transfer to occur. While at early times compression dominates, after some time this is overcome by diffusion (Le Borgne et al., 2015; Jiménez-Martínez et al., 2017). The cross over between two regimes is referred to the mixing time, t_m (Villermaux, 2012). The cross over time for shear flow can be obtained by equating the evolution of s due to shear which decreases as $s = s_0/\rho$ to the influence of diffusive expansion, $s = \sqrt{Dt}$, leading to,

$$t_m = \left(\frac{s_0^2}{D\gamma^2}\right)^{1/3}. \tag{2.24}$$

The analytical solutions presented here have been validated experimentally in microfluidic cells (Souzy, 2017) and have been used to describe mixing and reactions in millifluidic pore-scale experiments (Jiménez-Martínez et al., 2017; de Anna

et al., 2013b). Naturally, the lamella framework can be used to explore different elementary flow patterns as well as in more complex flows induced by heterogeneity that lead to random elongation and aggregation of lamellae (Le Borgne et al., 2015). The extension of the lamella theory for reactive transport will also be briefly covered in the following section.

2.3.3 Mixing and Reactions

Mixing plays a fundamental role when attempting to quantify chemical reactions. Naturally, for a reaction to occur, it necessitates initially segregated reactants to meet, which is initiated by mass transfer processes (i.e., advection and diffusion). Based on the time scales of mass transfer and reactions, chemical reactions can be limited by reaction kinetics or by mixing which dictates the time required for reactants to come into contact in solution or in the solid phase (Le Borgne et al., 2014). Whether the reaction is kinetically limited or mixing limited can be described by the Damköhler number,

$$\mathrm{Da} = \tau_m / \tau_r, \tag{2.25}$$

where τ_m is the characteristic mass transfer time scale (e.g. advective, τ_a or diffusive, τ_d) and τ_r is the characteristic reaction time scale. In the case the reaction is kinetics limited, $\mathrm{Da} \ll 1$. For the mixing limited condition $\mathrm{Da} \gg 1$. In Darcy scale flows, reactive transport is described by the advection-dispersion reaction equation

$$\phi \frac{\partial c_i(\mathbf{x}, t)}{\partial t} + \nabla \mathbf{q} c_i(\mathbf{x}, t) - \nabla \mathbf{D} \nabla c(\mathbf{x}, t) = r(t), \tag{2.26}$$

where c_i is the concentration of species i and r is the reaction rate described by the kinetic rate law,

$$\frac{dc_i(t)}{dt} = r(t). \tag{2.27}$$

To understand how reactions are enhanced by flow deformations, we can write (2.26) given lamella framework (Ranz, 1979; Le Borgne et al., 2014),

$$\frac{\partial c_i}{\partial t} - \gamma(t) n \frac{\partial c_i}{\partial n} - \mathbf{D} \frac{\partial^2 c_i}{\partial n^2} = r(t). \tag{2.28}$$

In Figure 2.3.3c-d) we can see how the formation of lamella due to flow deformation result in enhanced concentration gradients due to a decrease in mixing width, thereby also increasing chemical reactivity (Le Borgne et al., 2014). One of the most common reactive systems used to study mixing-dependent reactions is fast irreversible bimolecular reactions $A + B \rightarrow C$. The local reaction for this type of reaction is described by,

$$\frac{dC_A}{dt} = -k C_A C_B, \tag{2.29}$$

where k denotes the rate constant. This type of reaction has been used in a number of experiments that highlight the importance of incomplete mixing on reaction rates (de Anna et al., 2013b; Gramling et al., 2002; Oates and Harvey, 2006; Jose and

Cirpka, 2004). In these studies the total mass of product generated across the mixing front is typically calculated. This is otherwise known as the effective reaction rate,

$$R = \frac{dm_C}{dt}. \tag{2.30}$$

In many cases, the chemical reaction used in experimental porous media studies is fast enough that it can be assumed to occur instantaneously (infinite Damköhler limit). In the experimental investigation by de Anna et al. (2013b), the effective reaction rate approximated by,

$$\frac{dm_C(t)}{dt} \approx \frac{DL(t)C_0}{s(t)}. \tag{2.31}$$

In this case, the lamella framework describing the deformation of the mixing front due to shear was able to accurately predict the evolution of the reaction product. More recently, the influence of mixing on fast irreversible reactions in shear flows was also studied for arbitrary Damköhler numbers (Bandopadhyay et al., 2017). Their study provided analytical solutions for effective reaction rates and the evolution of reactive interface widths. This was able to highlight further complexity due to the strongly coupled nature of flow deformation, diffusion and reaction kinetics.

Another common reaction system studied is fast reversible reactions, $A + B \rightleftharpoons C$. The reaction rate for this sytem is limited by the availability of reactants and is triggered due to a perturbation of the local chemical equilibrium resulting from mixing. An example of such a reaction is the precipitation of mineral C, where the concentration of A and B can be given by the mass action law,

$$K = C_A C_B, \tag{2.32}$$

where K is the equilibrium constant. Assuming the same diffusive properties of the reactive species, the local equilibrium reaction rate can be given by (De Simoni, 2005),

$$r(\mathbf{x}, t) = \frac{1}{\phi} \frac{d^2 C_A}{dc^2} \nabla c(\mathbf{x}, t) \cdot \mathbf{D} \nabla c(\mathbf{x}, t), \tag{2.33}$$

where $c = C_A - C_B$ is the conservative component that satisfied equation 2.26 for $r(t) = 0$. The first term in this expression represents the non-linearity in speciation, and can be obtained by speciation codes to determine the concentration of reacting species (De Simoni et al., 2007). The second term however defines he scalar dissipation as described in 3.4. Using the lamellar representation of fluid mixing, effective reaction rates for fast reversible reactions have also been examined by Le Borgne et al. (2014), for a range of different geophysical flows, highlighting the link between reaction efficiency and the type of flow field at hand. This framework has similarly been used to model reactive mixing across stratified salt-freshwater interfaces (Pool and Dentz, 2018), dissolution patterns in unstable flows (Hidalgo et al., 2015).

In this chapter we have presented a non-exhaustive overview on the role of mixing and its influence over reactions in the subsurface. We have also shown different approaches that can be used to describe and quantify its behaviour in different flow systems. Although not all techniques will be revisited in the thesis, it provides a general idea to the concepts discussed in the following chapters.

CHAPTER 3

Heterogeneity-induced mixing and reaction hotspots facilitate Karst propagation in coastal aquifers [1]

ABSTRACT

The fresh-seawater mixing zone is a critical region for enhanced chemical reactions arising from chemical disequilibrium and variable density flow. While studies using homogeneous representations of carbonate systems have highlighted the novel reactive behavior of calcite dissolution across the saline-freshwater mixing zone, little knowledge exists highlighting the influence of heterogeneity on mixing and reactive dynamics even for steady state configurations. We shed light on the behavior of mixing and reactions by considering simplified representations of heterogeneity by implementing both large scale stratified aquifers as well as random log-normal hydraulic conductivity fields in the form of multi-Gaussian, connected and disconnected fields. Using a simplified modeling approach to incorporate fast-calcite dissolution, we illustrate the importance of mixing and chemical reactions in heterogeneous formations for steady state variable density flow system. Our results hope to shed light on the importance of heterogeneity on the propagation of karst formation in coastal carbonate aquifers.

[1] This Chapter is based on De Vriendt et al. - Heterogeneity-induced mixing and reaction hotspots facilitate Karst propagation in coastal aquifers. Geophysical Research Letters (2020)"

3.1 Introduction

The mixing of freshwater and seawater in coastal carbonate formations has been long associated with zones of high porosity development and elaborate cave networks (Back et al., 1986b). The presence of caves in the Yucatan peninsula (Back et al., 1979; Back et al., 1986b; R.K. Stoessell, W.C. Ward, B.H. Ford, 1989) and enhanced porosity observed from cores collected in the Bermudas Andros island (Smart et al., 1988) for example, have been directly attributed to mixing dynamics across the salt-freshwater mixing zone. Despite this, limited accessibility to deeper portions of the mixing zone has prevented large scale surveys of caves which may otherwise be available further inland. Since the topology of many karstic networks and their subsequent geomorphological characteristics are strongly linked to their flow regimes and local geology (Jouves et al., 2017), understanding the behaviour of mixing and reactions under variable density flow in coastal systems under the influence of various types of heterogeneity may offer insight into the localization of preferential calcite dissolution, which may be particularly important during the initial stages of karst propagation.

Numerical studies have previously demonstrated that calcite dissolution across the seawater-freshwater interface occurs dominantly across the fresher spectrum of the mixing zone where mixing waters are most strongly undersaturated with respect to calcite (Sanford and Konikow, 1989; Rezaei et al., 2005). Moreover, Sanford and Konikow (1989) found that dissolution takes place in fresher water then what would be expected by simple mixing alone. Interestingly, two reactive hotspots were also observed; one in fresher portion of the mixing zone at the toe and one in saltier portion of mixing waters at the discharge zone. These behaviours have been attributed to an initial mixing effect at the toe, which gives way to the highest potential for undersaturation and enhanced dispersive mixing at the discharge zone. While these homogeneous studies have provided valuable insight into the interplay between transport and chemical reactions, they fall short of explaining the maze-like conduit networks observed in real karst aquifers.

Coastal carbonate aquifers present heterogeneous discontinuities, such as fractures, dikes, and large scale stratification, which may induce complex salinity distributions leading to irregular patterns of enhanced local mixing and reactive hotspots, i.e. zones of enhanced reactivity. It is well known that heterogeneity of hydraulic properties strongly controls solute spreading and mixing in porous media (Dagan, 1987; Gelhar, 1993; Gelhar, 2003; Dentz et al., 2011). Heterogeneity has also been suggested as an important mechanism toward realistic representations of mixing and offshore submarine groundwater discharge (Michael et al., 2016). However, only few studies have addressed heterogeneity for variable density flow systems and, in particular, for seawater intrusion problems (see, e.g., Held et al., 2005; Abarca, 2006; Kerrou and Renard, 2010; Sebben et al., 2015; Pool et al., 2015; Kreyns et al., 2020). In general, it has been shown that heterogeneity leads to increased spreading of the freshwater-seawater mixing zone. While it is evident that heterogeneity plays a strong role in mixing in many subsurface groundwater problems, its impact on mixing-limited reactions such as calcite dissolution in coastal variable density flow systems remains an open question.

In this paper we investigate the effect of heterogeneity and connectivity on mixing and chemical reactions across the salt-freshwater interface under steady-state conditions. We consider a fast calcite dissolution reaction to explore karstification processes induced by mixing in coastal aquifers. Two-dimensional variable density flow and transport simulations are performed considering large scale hydraulic

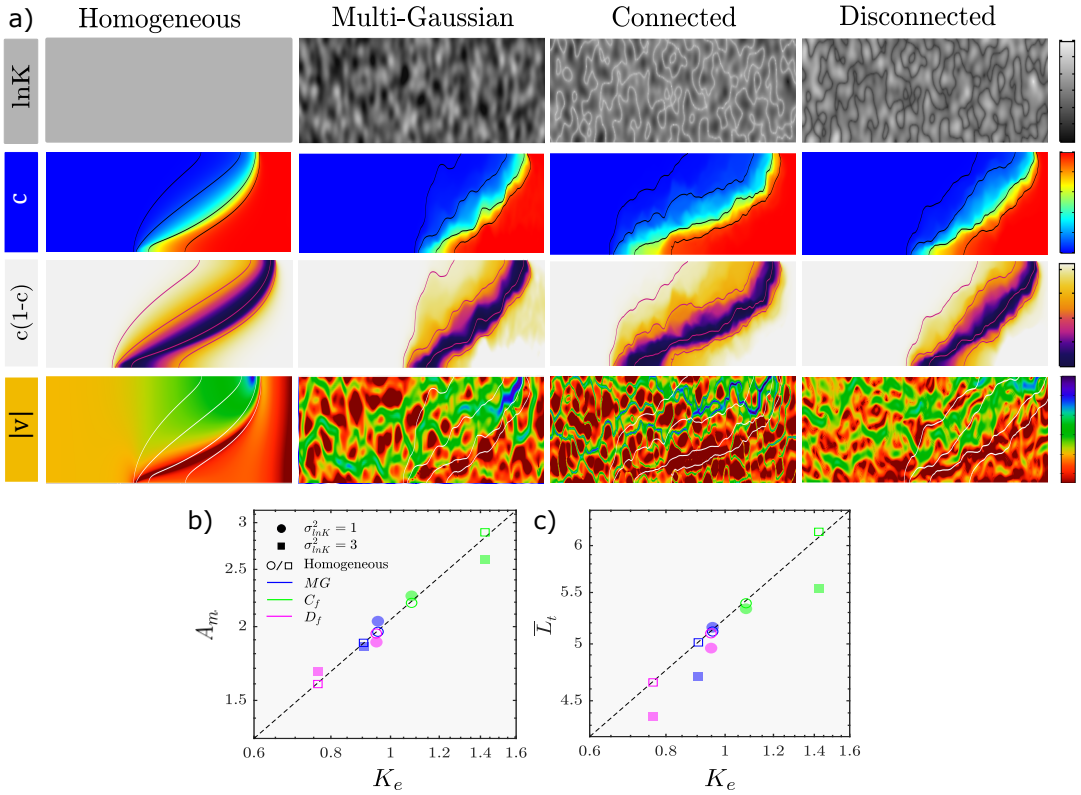

FIGURE 3.1.1: Maps showing examples of (from top to bottom) the hydraulic conductivity field for the homogeneous and heterogeneous fields ($\sigma^2_{lnK} = 1$), the mixing ratio (c), $c(1-c)$ and the logarithm of the velocity modulus ($|v|$). b) The non-dimensional average mixing area ($\overline{A}_m$) and c) the toe position ($\overline{L}_t$) against their non-dimensional hydraulic conductivity (K_e). The dashed lines denote the dependence of the mixing area and toe position on hydraulic conductivity for an equivalent homogeneous medium. Mixing ratio contours displayed in the maps correspond to mixing ratios of 1%, 10%, 50% and 95%.

.

conductivity stratification and log-normally distributed multi-Gaussian hydraulic conductivity fields. In addition, more complex heterogeneous fields characterized by connected and disconnected patterns of high and low conductivity are considered. We analyze the mixing and reaction dynamics by focusing on the local and global reaction and mixing rates. Our results aim to provide insight into the role of heterogeneity in non-uniform flow fields such as that induced by seawater intrusion.

3.2 Methods

We study mixing and calcite dissolution patterns under steady variable density flow in two-dimensional heterogeneous coastal aquifers. Density-dependent flow is described by the Darcy equation

$$\mathbf{q}(\mathbf{x}) = -K(\mathbf{x}) \left[\nabla h_f(\mathbf{x}) + \frac{\rho(\mathbf{x}) - \rho_f}{\rho_f} \mathbf{e}_z \right], \tag{3.1}$$

where $\mathbf{x} = (x, z)^\top$ is the coordinate vector, $\mathbf{q}(\mathbf{x})$ the specific discharge, $K(\mathbf{x})$ hydraulic conductivity, $h_f(\mathbf{x})$ the equivalent freshwater head, $\rho(\mathbf{x})$ the fluid density, ρ_f

the density of freshwater and $\mathbf{e}_z$ is the unit vector in z-direction. Fluid mass conservation in the absence of sources and sinks implies $\nabla \cdot \rho(\mathbf{x})\mathbf{q}(\mathbf{x}) = 0$. The fluid density depends on the mixing ratio $c(\mathbf{x})$ between fresh and seawater and is assumed to be linearly dependent on the salt mass fraction $\omega(\mathbf{x})$ (mass of salt dissolved per unit mass of fluid) given by $\rho(\mathbf{x}) = \rho_f[1 + \beta c(\mathbf{x}, t)]$ where β is the buoyancy factor given by $\beta = (\rho_s - \rho_f)/\rho_f$ and ρ_s is the density of seawater. The mixing ratio is given by $c(\mathbf{x}) = \omega(\mathbf{x})/\omega_s$ with $\omega(\mathbf{x})$ the salt mass fraction in the mixture and ω_s the salt mass fraction of seawater. Thus, it obeys the steady state advection-dispersion equation (Voss and Provost, 2002),

$$\mathbf{q}(\mathbf{x}) \cdot \nabla c(\mathbf{x}) - \nabla \cdot [\mathbf{D}(\mathbf{x}) + \phi D_m] \nabla c(\mathbf{x}) = 0, \tag{3.2}$$

with $\mathbf{D}(\mathbf{x})$ the dispersion tensor (Bear, 1988), D_m molecular diffusion and ϕ porosity.

The flow domain is 1500 m long and 100 m wide with a prescribed freshwater flux of 250 m/a and zero mixing ratio at the inland boundary at $x = 0$ and hydrostatic saltwater at the seaward boundary. The mixing ratio and the inland boundary is set to 0, while the mass flux at the seaward boundary is set equal to the advective flux of seawater if the horizontal component of $\mathbf{q}$ point inland and equal to the advective flux of the local mixing ratio otherwise. A detailed relation of the numerical set-up can be found in section 3 of the appendix. Hydraulic conductivity $K(\mathbf{x})$ is modelled as a two dimensional spatial random field. We consider multi-Gaussian (MG), as well fields of connected high (C_f) and low hydraulic conductivity (D_f). All fields are characterized by log-normal point statistics with variances of the log-hydraulic conductivity $\sigma^2_{lnK} = 1$ and 3. The connected high (C_f) and low hydraulic conductivity (D_f) serve to mimic the presence of channels or fractures.

In order to highlight the influence of heterogeneity on mixing and reaction efficiency, we compare the results from the heterogeneous to equivalent homogeneous scenarios. For each type of heterogeneity and log-K variance, 10 equally probable realizations are considered. The observables presented in the following are obtained by averaging over the set of realizations for each heterogeneity type (averaged quantities are denoted by an overline). While we consider only a limited number of realizations due to computational constraints, the variability between realizations is low such that the average can be considered representative for the heterogeneity impact on the mixing and reaction behaviour. Furthermore, in order to illustrate reactive patterns that may emerge in the presence of large scale discontinuities, we consider in Section 3.3.3 two realizations of a stratified multi-Gaussian aquifer structure characterized by infinite longitudinal correlation length, transverse correlation length of 10 m and $\sigma^2_{lnK} = 1$ and 3. Details are given in Section 4 of the appendix.

Figure 3.1.1a illustrates maps of the mixing ratio and velocity magnitude for homogeneous, multi-Gaussian, connected and disconnected hydraulic conductivity fields. The mixing area $\overline{A}_m$ between fresh and seawater shown in Figure 3.1.1b is defined as the area comprised between the 0.95 and 0.01 isolines of the mixing ratio. The penetration depth $\overline{L}_t$ of the seawater wedge shown in Figure 3.1.1c is defined as the distance of the 0.5 isoline of the mixing ratio from the seaside boundary. Note that both these quantities are averaged across all realizations. The mixing area and penetration depth are non-dimensionalized in terms of the characteristic length scale l_c, which here is identified with the height of the domain.

In order to investigate the influence of heterogeneity on mixing and reaction efficiency, we compare the results from the heterogeneous realizations to equivalent homogeneous media. In order to determine the effective hydraulic conductivity of the equivalent media, a constant hydraulic head gradient is imposed between the

inland and the seaside boundaries for each heterogeneous realization, with the horizontal boundaries defined as no flow boundaries. The effective hydraulic conductivity K_e is given by the ratio between the total flow rate across the seaside boundary and the average hydraulic head gradient. The effective hydraulic conductivity is non-dimensionalized by the geometric mean conductivity K_g, which for all fields under consideration is $K_g = 5 \cdot 10^{-4}$ m/s. Note that for isotropic multi-Gaussian fields, K_g is equal to the effective conductivity (see, e.g. Renard and Marsily, 1997; Sanchez-Vila et al., 2006). As evidenced in Figure 3.1.1 (b-c), $\overline{K}_e$ corresponds well to the level of connectivity of each field. As found by Zinn and Harvey, 2003, connectivity results in an increase in $\overline{K}_e$. Furthermore, as observed for multi-Gaussian heterogeneous media (Abarca, 2006; Kerrou and Renard, 2010), we see in Figure 3.1.1 (b-c) that both $\overline{L}_t$ and $\overline{A}_m$ decrease with increasing heterogeneity This can be directly linked to a decrease in $\overline{K}_e$. For the connected fields $\overline{K}_e$ increases with increasing heterogeneity. In general we see that increase or decrease in $\overline{K}_e$ directly corresponds to increase or decrease in toe length and mixing area for both the homogeneous and heterogeneous fields.

The mixing and reaction behaviour and its impact on karst propagation are studied through the process of mixing-induced calcite dissolution. In the considered setting, we use the two representative end-members of freshwater and seawater according to Rezaei et al., 2005. The seawater composition represents water collected from boreholes in a coastal aquifer from Grand Cayman (Ng and Jones, 1995) while the freshwater compositions represents distilled water in equilibrium with calcite, see Table 1 in the appendix for the details of the chemical system. When the respective equilibria are perturbed due to mixing, the new chemical equilibrium of the mixture is established instantaneously. This is a reasonable assumption for coastal aquifers where calcite dissolution is fast relative to the residence times of water (Sanford and Konikow, 1989; Rezaei et al., 2005). We consider the chemical system detailed in De Simoni et al. (2007) under conditions that lead to undersaturation upon mixing and thus calcite dissolution. Note that this study does not incorporate any feedback between chemical reactions and the flow and transport properties. The equilibrium reaction rate can then be written in the form

$$r(\mathbf{x}) = \Lambda(\mathbf{x})\chi(\mathbf{x}), \tag{3.3}$$

where $\chi(\mathbf{x})$ is the local mixing rate,

$$\chi(\mathbf{x}) = \nabla c(\mathbf{x}) \cdot [\mathbf{D}(\mathbf{x}) + \phi D_m] \nabla c(\mathbf{x}). \tag{3.4}$$

Reaction and mixing rates are non-dimensionalized in the following according to $r' = r l_c / q_f \sqrt{K_{eq}}$, and $\chi' = \chi l_c^2 / \alpha_g q_f$ where α_g is the geometric mean of the longitudinal and transverse dispersivities, q_f is the inland freshwater flux and K_{eq} is the solubility product for calcite dissolution. In the following, we omit the primes for simplicity of notation. The mixing rate χ measures the dynamics of conservative mixing between fresh and saltwater. The chemistry is contained in the speciation intensity Λ as outlined in detail in Section 2 of the appendix. Note that the term equilibrium reaction rate may appear contradictory, however, it describes the rate of reaction due to fast chemical equilibration of two end-members upon mixing. Therefore it is dominated by the mixing rate χ, whose magnitude depends on both concentration gradients and dispersion coefficients. In our analysis we assess the average scalar dissipation rate $\langle\chi\rangle$ and reaction rate $\langle r\rangle$ per unit mixing area. This facilitates the intercomparison of heterogeneous fields with respect to the corresponding

homogeneous scenarios.

3.3 Results and Discussion

We discuss here the impact of heterogeneity on mixing and dissolution patterns and their subsequent implications on the propagation of karsts.

3.3.1 Influence of Heterogeneity on Mixing Rate

Figure 3.3.1 shows the strong impact that the presence of heterogeneity has on both the mixing and reaction rate across the interface. At the top of the transition zone, high velocities induced by the freshwater discharge translate to strong dispersive mixing (Rezaei et al., 2005). This is reflected in χ for both the homogeneous and heterogeneous media. It can be observed that heterogeneity-induced velocity variations lead to both greater variability, and the steepening of concentration gradients resulting in enhanced mixing along the mixing interface. As expected, since χ depends on both the presence of concentration gradients and dispersion, the largest values are localized in high-K zones, where velocities and thus dispersion are large. Note that while χ is generally highest along the 50% mixing ratio contour, near the toe it extends into the fresher portion of the mixing zone. This can be likely attributed to enhanced interface compression that accompanies stagnation points (see, e.g., Ranz, 1979; Hidalgo and Dentz, 2018), which for the seawater intrusion problem, exists at the toe. This observation suggests that the localised hotspot at the toe is not simply the result of the previously mentioned initial-mixing effect (Sanford and Konikow, 1989; Rezaei et al., 2005), but also due to strong flow deformation.

As shown in Figure 3.3.1c, $\langle\chi\rangle$ decreases linearly with increasing effective hydraulic conductivity for homogeneous media. There are two factors dominating $\langle\chi\rangle$. We first observe that the presence of hetereogeneity in general and the value of log-K variance in particular result in an increase of $\langle\chi\rangle$ for all fields with respect to their homogeneous equivalent. This is most notable for the connected scenarios, for which the mixing rate increases up to a factor of 2. Additionally, we see that K_e strongly controls the behaviour of $\langle\chi\rangle$ for homogeneous and weakly heterogeneous fields. This may be understood as follows. For high K_e, the interface penetrates further and is flatter than for low K_e. Thus, at high K_e, there is a lower velocity contrasts between the flowing freshwater body and the convection cell at the seaside boundary. Reduction of velocity contrast leads to a reduction of concentration contrast, which in turn reduces the mixing rate.

3.3.2 Influence of Heterogeneity on the Reaction rate

In accordance with the studies of Sanford and Konikow (1989) and Rezaei et al. (2005), zones of enhanced calcite dissolution are shown to occur near the fresher spectrum of the mixing zone see Figure 3.3.1a. This is once again due to the fact that the speciation intensity, which is a non-linear function of the mixing ratio, concentrates at the freshwater dominated part of the mixing zone. In fact, reaction hotspots may be due to a high local speciation intensity in a moderate mixing background, or due to a high mixing rate in a background of moderate speciation intensity. For the homogeneous scenarios, as expected, one observes two significant reaction hotspots at the top and bottom of the mixing zone. The reaction hotspot at the top of the aquifer coincides with the mixing hotspot, while the reaction hotspot at the toe is determined by high speciation intensity in the presence of moderate mixing. Our

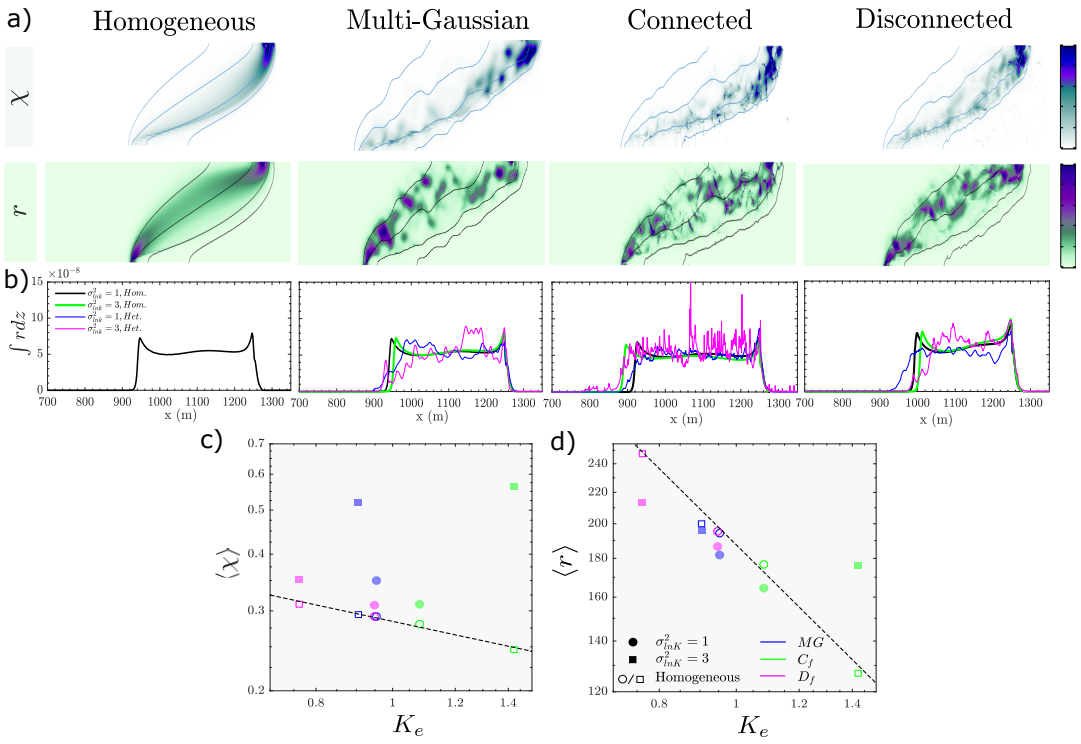

FIGURE 3.3.1: Examples of maps for ($\sigma^2_{lnK} = 3$) corresponding to (from top to bottom) the average mixing and reaction rates and the vertically integrated reaction rate for the homogeneous, multi-Gaussian (MG), connected (C_f) and disconnected fields (D_f). The scatter plot at the bottom shows the average non-dimensional mixing rate ($\langle\chi\rangle$) and non-dimensional reaction rates ($\langle r\rangle$) for their corresponding non-dimensional effective hydraulic conductivities $\overline{K_e}$. Mixing ratio contours displayed in the maps correspond to mixing ratios of 1%, 10%, 50% and 95%. The dashed lines denote the dependence of the mixing and reaction rate on hydraulic conductivity for an equivalent homogeneous medium

simulations reveal that heterogeneity induces highly irregular distributions of reaction rates that strongly deviate from the homogeneous case.

This is further evidenced in Figure 3.3.1b, which shows the vertically integrated heterogeneous reaction rate profiles compared to their respective effective homogeneous behaviour. In the presence of heterogeneity, distinct reaction hotspots emerge along the interface whose density and intensity increase with increasing heterogeneity and also with the connectivity. Thus, spatial heterogeneity broadens the spectrum of local reaction rates towards high values compared to homogeneous media. In Figure 3.3.1d, we observe that, for the exception of the high variance connected field, $\langle r\rangle$ is smaller for heterogeneous fields compared to the respective homogeneous case. This can be understood by the increased segregation of high-K zones, where reactions preferentially occur. In the case of the high variance connected field, an increase in $\langle r\rangle$ compared to the homogeneous scenario can be attributed to the strongly enhanced mixing rates observed in Figure 3.3.1c, which permits reactions to occur over a larger portion of the mixing zone.

While the spatial variability of reactions are strongly impacted by the presence of heterogeneity, we see that, similar to the behaviour of $\langle\chi\rangle$ for homogeneous and weakly heterogeneous scenarios, $\overline{K_e}$ exerts a strong control over $\langle r\rangle$, even for the

higher log-K variance disconnected and multi-Gaussian fields. It should be reiterated that while an increase in $\overline{K}_e$ lengthens the interface, which increases the area over which mass-transfer can occur, the velocity and concentration contrasts at the mixing interface are higher when the toe is closer to the seaside boundary, resulting in higher averaged reaction rates per unit area.

3.3.3 Influence of Heterogeneity on Reactive Patterns

The type of imposed heterogeneity manifests in particular patterns of enhanced reactivity in the presence of the non-uniform flow field. Multi-Gaussian fields for example, are characterized by hotspots that radiate concentrically, while connected field hotspots are predominantly isolated in high-K channels that are orientated vertically, parallel to the local direction of flow. For the disconnected field, reaction patterns are qualitatively similar to multi-Gaussian fields, but they also contain zones of enhanced reaction that straddle low-K channels, perpendicular to the local direction of flow, as can be seen in Figure 3.3.2. It is interesting to note that despite the apparent connectivity of the imposed heterogeneous structures, zones of enhanced reactivity tend to emerge as unconnected features. This suggests that during early stages of diagenesis, the spatial location and orientation of hydraulic features during seawater intrusion may strongly control the transient evolution of caves. It is possible however, that in the presence of temporal fluctuations, the movement of the wedge back and forth over large time scales may be the precursor to connecting these localised reactive hotspots into the maze-like features we observe today.

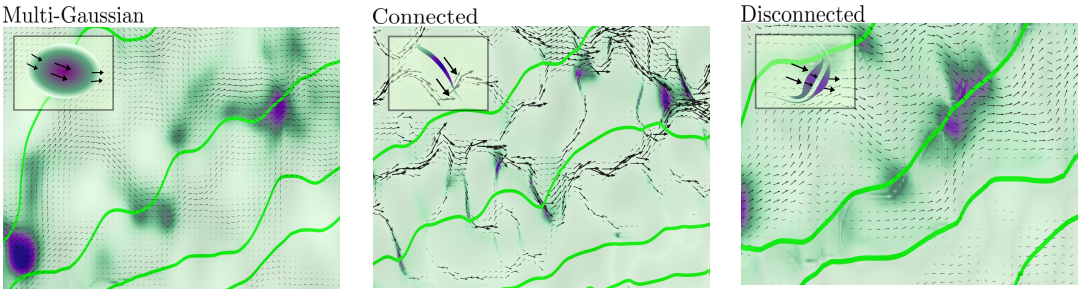

FIGURE 3.3.2: Zoomed in sections of the Reaction field overlaid with their corresponding hydraulic conductivity field. Arrows represent flow directions whose length is proportional to the logarithm of velocity.

Unlike linear fractures, which are prevalent in carbonates, the field presented till now are far more non-linear and tortuous. In the following, we investigate the impact of horizontally stratified conductivity fields, which although are not segmented, allows us to gain insight to calcite dissolution in the presence of large scale connectivity. Future studies, may however greatly benefit by looking into similar behaviour using discrete fracture networks. We observe that vertical changes in hydraulic conductivity causes strong velocity and concentration contrast across the mixing interface which manifests as narrow, elongated zones of enhanced reactivity. In Figure 3.3.3, we see that by increasing the log-K variance, the strong concentration gradient along the low-K layers lead to enhanced reactions. In addition to the stratified multi-Gaussian fields, simulations for discrete low-high-low (1:10:1) and high-low-high (10:1:10), further isolates these dynamics. We see that when a low-conductive material sandwiches a high-conductive layer, strong dissolution occurs at the base of the high-K zone, whereas strongest dissolution is observed at the top

of the stratified layer for the high-low-high K scenario. This illustrates that reaction is enhanced when flow is directed from a low to high-K medium, which sheds light on the preferential development of karstic systems.

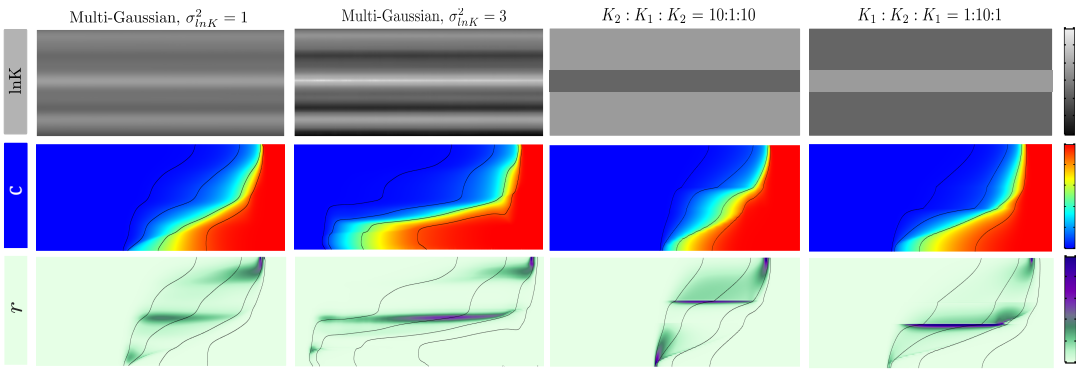

FIGURE 3.3.3: Horizontally stratified hydraulic conductivity fields. From top to bottom are the log-K, the mixing-ratio, and reaction rate fields. The two left-most columns show the results for the multi-Gaussian stratified scenario for $\sigma^2_{lnK} = 1$ and 3 while the two right-most columns show the results for an aquifer whose hydraulic conductivity is discretely layered. The third column shows the results for a K-ratio of 10:1:10 while the fourth column shows the result for a K-ratio of 1:10:1.

3.4 Concluding remarks

The topology of karst conduits have been strongly linked to their spatial location and the governing flow characteristics (e.g., Palmer, 1992; Audra and Palmer, 2015; Gabrov et al., 2014). For example, anastomosic caves, defined by their braided patterns, typically occur across bedding planes in the epiphreatic zone, whereas angular mazes tend to be associated with fractured media due to seepage from overlying insoluble rocks (Jouves et al., 2017). While near-surface features such as flank margin caves (Mylroie and Carew, 1990) can be observed in many coastal carbonate environments along the salt-freshwater mixing zone, limited accessibility has prevented large-scale speleological surveys of karst conduits in coastal aquifer. Consequently, no formal characteristics exist to describe dissolution patterns at depth across the mixing zone. It is therefore possible, that many hydraulically dominant karstic features may exist outside our current ability to observe.

Our study suggests that the initial stages of karst development, also known as the laminar flow phase (Lowe, 1992), may be a crucial period which influences the subsequent evolution of a karstic conduit. The importance of early-stage karst development was also investigated by Groves and Howard (1994), who found that enlargement of conduits in coastal carbonate aquifers occurs very selectively during the laminar flow regime. Geomorphological studies on phreatic karstic caves have shown that over 70% of conduits develop along discrete bedding planes in limestones (Filipponi et al., 2009), known as 'inception horizons' (Lowe, 1992). Such features are the result of physical, lithological and chemical deviations from the central carbonate facies. Cave surveys have shown that inception horizons may play a strong role during the most early stages of karst formation (Filipponi et al., 2009). In the simplest case of large scale horizontal stratification, our study suggests that

in coastal environments, due to the density-driven convection and subsequent upward re-circulation of flow, even simple changes in hydraulic conductivity could be very sensitive to enhanced dissolution. Sanford and Konikow (1989) showed that a migrating seawater wedge in a homogeneous media results in increased permeability which would consequently shift the wedge further inland. One could therefore imagine that large-scale sea level and tidal fluctuations could generate elongate karstic features that extend many kilometres inland.

It should be noted that, while karstification is inherently a 3D process, our study sheds light on the fundamental mechanisms relating medium structure, flow heterogeneity, and mixing and dissolution. While it is likely that in 3D we would see an increase in connectivity which would alter stretching dynamics, due to their fundamental nature, we expect them to be qualitatively similar in 2D. This paper refers particularly to the finding that the initial structure of the aquifer and its impact over the mixing and reaction patterns plays a key role for understanding the development of realistic karstic systems observed across modern coastlines.

Appendix

3.A Appendix

In this appendix we provide additional information surrounding the numerical model employed and the diagnostics used in order to evaluate the results. We also provide additional supporting figures and tables referred to in the main text.

3.A.1 Chemical system

We consider the two end-member chemical composition specified by Rezaei et al., 2005. In order to attain the local reactions rates across the salt freshwater interface we employ a mixing-ratio based method for reactive transport. Since this method decouples the solute transport and chemical speciation components of the problem, the mixing ratios must first be found by solving the conservative transport problem. The concentrations of the reacting species can then be found using a general speciation code. In this work, PHREEQC was employed. In order to calculate the concentrations of our reacting species, PHREEQC is provided with the chemical compositions of the fresh and saline groundwater. For this we use the end-member compositions given in the table provided below (see Table 4.2). PHREEQC performs the speciation calculations for a given set of mixing ratios ranging between 0 an 1. From here we can now plot the second derivative of our secondary species (Ca^{2+}) with respect to the mixing ratio ($\delta^2 Ca^{2+}/\delta^2 \alpha$) against our range of mixing ratios which will be used to solve the local reaction rates across the mixing zone (see Figure 3.A.1).

TABLE 3.A.1: Chemical composition of end-members used in speciation calculations. All concentration units are in $mmol \cdot kg^{-1}$

Solution	**pH**	**Ca**	**Mg**	**Na**	**K**	**Cl**	**log** P_{CO_2}	I
Seawater	7.21	9.64	22.43	496.53	9.28	564.13	-2.01	6.25
Freshwater	7.30	1.65	0.00	0.00	0.00	0.00	-2.00	0.005

3.A.2 Numerical flow and transport model

3.A.2.1 Field generation

We generate multi-Gaussian (MG) random fields with a geometric mean of $5 \cdot 10^{-4}$ m/s and log-conductivity variances of $\sigma^2_{\ln k}$=1 and 3 using a discrete fourier transform technique (e.g. Cirpka and Kitandis, 2002). The Multi-Gaussian fields are characterized by an Gaussian covariance function with isotropic correlation length of 10 m. From the respective MG fields, fields of connected high and low values are obtained following the method of Zinn and Harvey, 2003.

3.A.2.2 Variable density flow and transport

Fluid-density-dependent saturated flow and transport simulations were performed with COMSOL Multiphysics®. The governing equations for variable density flow

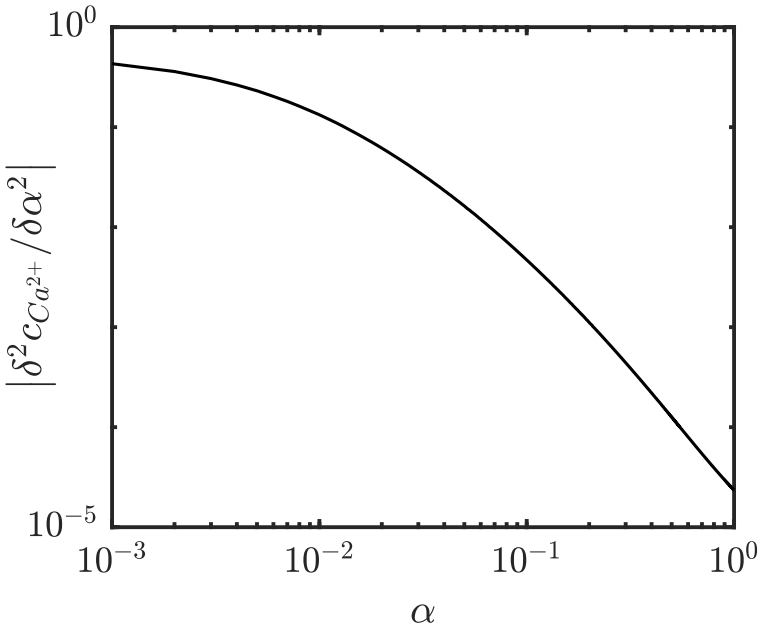

FIGURE 3.A.1: Dependence of the absolute of $\delta^2 Ca^{2+}/\delta^2\alpha$ on α

and transport are described by the Darcy law and the steady state advection-dispersion equation, see Equations 4.1 and 4.2 in the main paper. Note that while it is common to use a transverse to longitudinal dispersivity ratio of 0.1, we choose a ratio of 0.5 which has also been observed in seawater intrusion experiments (e.g. Abarca and Clement, 2009; Robinson et al., 2015). The model set-up is similar to that of Sanford and Konikow, 1989 and Rezaei et al., 2005 with a model extent of L_x=1500m and a constant thickness of L_z =100m. The shoreline was established at x = 1250 m. The model was discretized into 2×2 m^2 regular cells. The discretization satisfies the mesh peclet number criterion (Voss and Souza, 1987) such that

$$Pe_m = \frac{q_f \Delta L}{D_m + \alpha_L q_f} \leq 4, \tag{3.5}$$

where ΔL is the grid size. This criterion ensures oscillations in the concentration distribution are minimized. The mixing ratio is defined by the normalized salt mass fraction $c = \omega/\omega_s$ with ω the salt mass fraction of the fluid and ω_s the seawater salt mass fraction. The boundary conditions adopted consist of a prescribed constant freshwater flow rate of q_f at the inland boundaries and prescribed hydrostatic pressure along the offshore boundaries as shown in Figure 3.A.2. The mixing ratio at the vertical inland boundary is given by the Dirichlet condition $c(\mathbf{x}) = 0$ at $x = 0$, and at the vertical offshore boundary by the Neumann boundary condition $\frac{\partial c(\mathbf{x})}{\partial x} = 0$ at $x = L_x$. The latter implies that water with $c = 1$ enters the aquifer at the locations at which $q_x < 0$ and water with the formation mixing ratio c exits where $q_x > 0$. The bottom boundary is a no-flow boundary for both salt mass fraction and water. The numerical values of the modeling parameters are provided in Table 3.A.2. A schematic of the modeling domain and the applied boundary conditions is shown in Figure 3.A.2. Models were run until the steady state for both heads and concentrations was reached. An adaptive timestepping scheme is used which automatically adjusts the time step in order to maintain the desired relative tolerance. We consider for each heterogeneity setup 10 equally probable realizations.

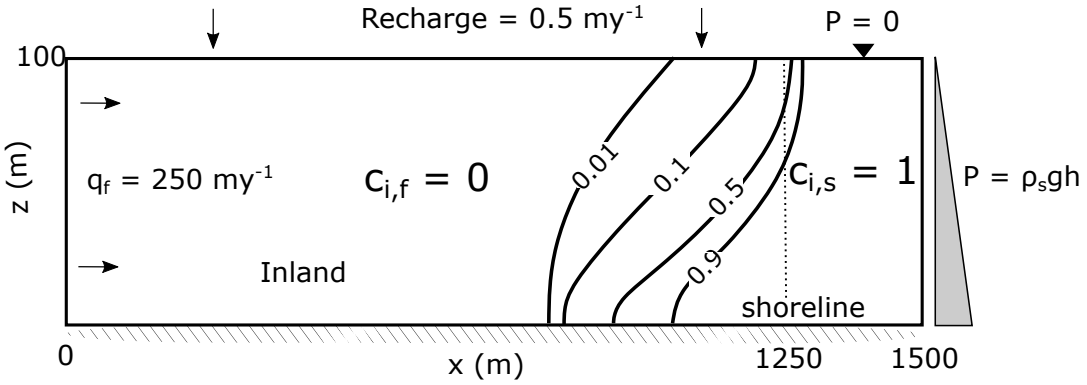

FIGURE 3.A.2: Boundary conditions and initial conditions for the of the given saline intrusion problem.

TABLE 3.A.2: Summary of key parameters values used in the numerical simulations

Parameter	Description	Value	Unit
K_G	Geometric mean conductivity	5e-4	ms^{-1}
q_f	Inland freshwater flux	250	myr^{-1}
ϕ	Porosity	0.3	-
α_L	Longitudinal dispersion	6	m
α_T	Transverse dispersion	3	m
R	Recharge	0.5	$my^{-}1$
ρ_f	Freshwater density	1.00e3	kgm^{-3}
ρ_s	Seawater density	1.025e3	kgm^{-3}
ρ_s	Fluid viscosity	1.00e-3	$kgm^{-3}s^{-1}$

3.A.3 Observables

The observables are obtained by ensemble averaging over the realizations for each heterogeneity type. While we consider only a limited number of realizations due to computational constraints, the variability between realizations is low such that the average can be considered representative for the heterogeneity impact on the mixing and reaction behavior.

3.A.3.1 Effective hydraulic conductivity

In order to approximate the effective hydraulic conductivity for each heterogeneous realization (multi-Gaussian, connected and disconnected fields), a hydraulic head difference of Δh =5 m was imposed across the length of the domain using two constant head boundaries with the upper and bottom boundaries defined as no flow. The mean flux was then calculated across the left boundary in order to determine the effective hydraulic conductivity as

$$K_{eff} = \frac{1}{\Delta h}\frac{L_x}{L_z}\int_0^{L_z} dz q_x(L_x, z). \tag{3.6}$$

The average effective conductivity is obtained by averaging over the realizations as

$$\overline{K}_{eff} = \frac{1}{N}\sum_{i=1}^{N} K_{eff}^i \tag{3.7}$$

Figure 3.A.3 shows the average effective conductivity for the different conductivity fields along with the error bars. The average seems to stabilize after only 10 realizations.

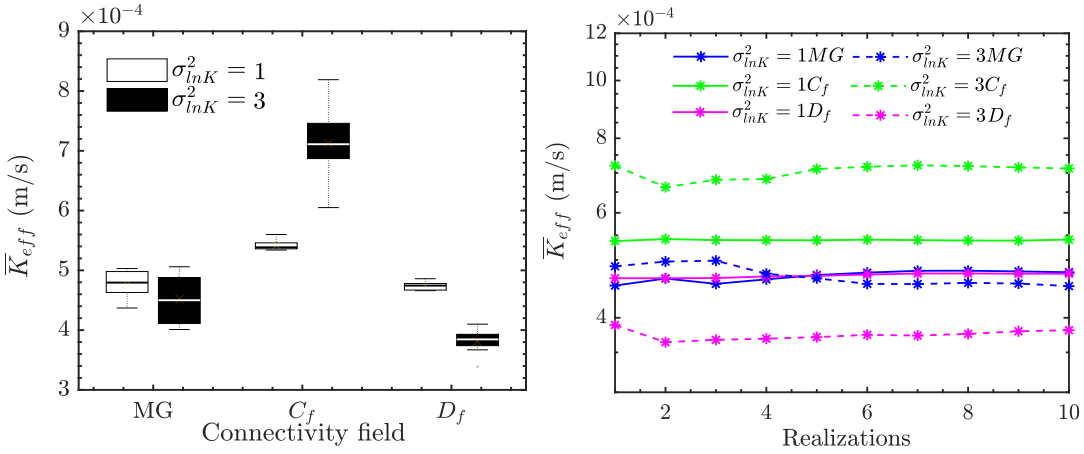

FIGURE 3.A.3: Box plot (left) showing the average effective conductivity ($\overline{K}_{eff}$) for $\sigma^2_{lnK} = 1, 3$. $\overline{K}_{eff}$ is shown for each additional realisation (right).

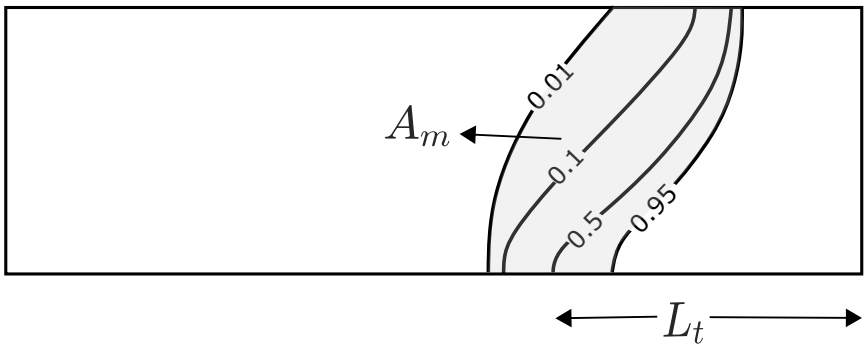

FIGURE 3.A.4: Schematic showing variables of interest for saltwater mixing wedge. The diagram shows mixing ratio contour lines 0.01, 0.1, 0.5 and 0.95. The bounded shadowed area is A_m which is between mixing ratio lines 0.01 to 0.95. The arrow at the bottom of the schematic illustrates the measured length toe position (L_t).

3.A.3.2 Toe position

The toe position L_t is defined by the distance of the intersect of the $c = 0.5$ isoline with the bottom boundary and the seaward domain boundary,

$$L_t = F^{-1}(0.5), \qquad F(x) = c(x, 0) \tag{3.8}$$

The average toe position is obtain by ensemble averaging as

$$\overline{L}_t = \frac{1}{N} \sum_{i=1}^{N} L_t^i \tag{3.9}$$

Figure 3.A.5 shows the average toe position for the different hydraulic conductivity fields.

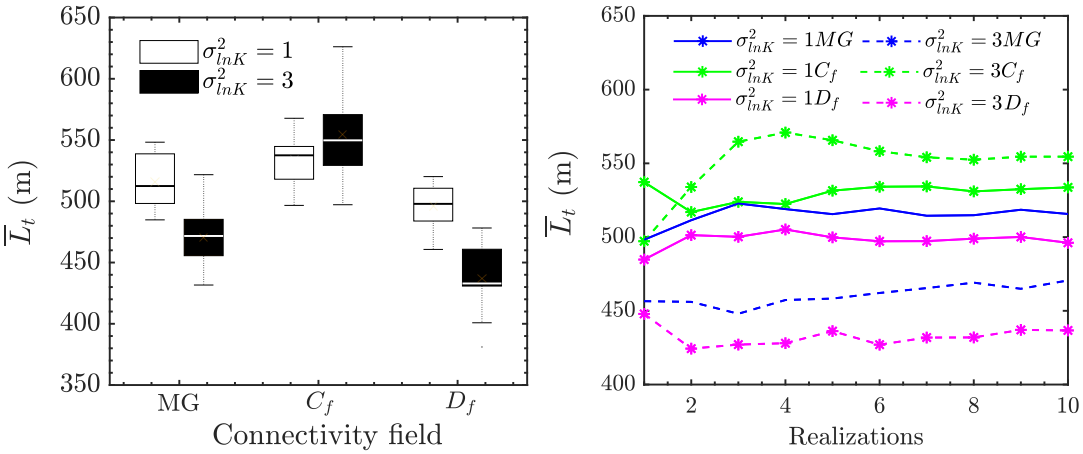

FIGURE 3.A.5: Box plot (left) showing the average toe position ($\overline{L}_t$) for $\sigma^2_{lnK} = 1, 3$. $\overline{L}_t$ is shown for each additional realisation (right).

3.A.4 Mixing area

The Mixing Area (A_m) is defined by the area bounded between the $c_{min} = 0.01$ and $c_{max} = 0.95$ isolines of the mixing ratio,

$$A_m = \int H\left[c(x,z) - c_{min}\right] H[c_{max} - c(x,z)]\, dxdz \tag{3.10}$$

where H is the heaviside step function. The range was chosen in order to capture where the majority of mixing and reactions would occur. Rather than bound the mixing area by the more traditional 0.1-0.9 mixing ratio isolines we extend the dilute end to 0.01, since the fresher spectrum of mixing is important for calcite dissolution. The average mixing area is defined by

$$\overline{A}_m = \frac{1}{N} \sum_{i=1}^{N} A_m^i \tag{3.11}$$

Figure 3.A.6 shows the average mixing area. We show that the average mixing area also stabilizes over the chosen number of realizations simulated.

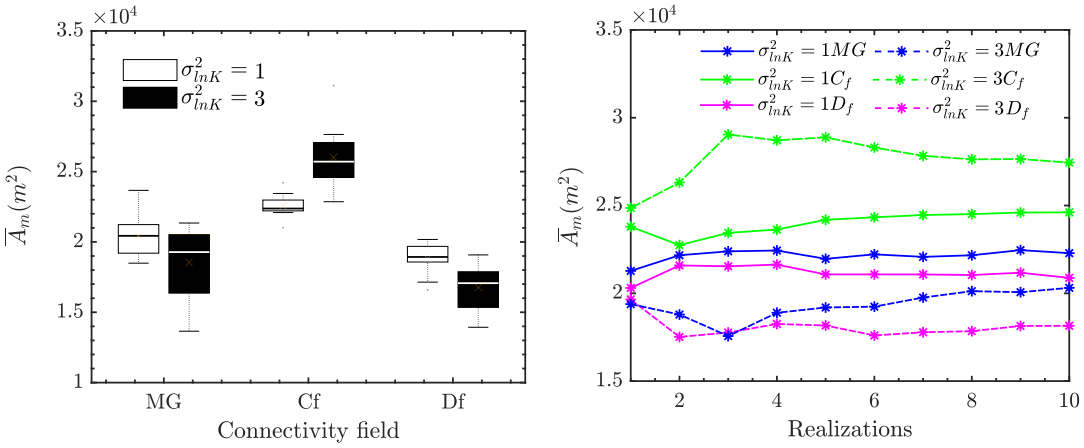

FIGURE 3.A.6: Box plot (left) showing the average mixing area ($\overline{A}_m$) for $\sigma^2_{lnK} = 1, 3$. $\overline{A}_m$ is shown for each additional realisation (right).

3.A.4.1 Effective interface width

The effective interface width is defined as the ratio between the mixing area and the toe position

$$w_m = \frac{A_m}{L_t}. \tag{3.12}$$

It is a measure for the interface width because the length of the interface is proportional to the toe position. The average mixing width is therefore defined as,

$$\overline{w}_m = \frac{1}{N} \sum_{i=1}^{N} w_m^i \tag{3.13}$$

3.A.4.2 Mixing and reaction rate statistics

The statistics of the mixing and reaction rates are sampled within the mixing zone Ω_m delimited by the $c_{min} = 0.01$ and $c_{max} = 0.95$ isolines of the mixing ratio

$$\Omega_m = \{\mathbf{x} | c_{min} < c(\mathbf{x}) < c_{max}\}. \tag{3.14}$$

Thus, the probability density function (PDF) of the mixing rate $\chi(\mathbf{x})$ is obtained by sampling the local values in each realization and constructing a normalized histogram as

$$p_\chi(\chi) = \frac{1}{N}\sum_{i=1}^{N}\frac{1}{A_m}\int_\Omega dxdz \frac{\mathbb{I}[\chi < \chi^i(\mathbf{x}) \leq \chi + \Delta\chi]}{\Delta\chi} \tag{3.15}$$

where the indicator function $\mathbb{I}(\cdot)$ is 1 is the argument is true and 0 else and $\Delta\chi$ is the bin size used to sample mixing rate data. The PDF of the reaction rates is defined in analogy as

$$p_r(r) = \frac{1}{N}\sum_{i=1}^{N}\frac{1}{A_m}\int_\Omega dxdz \frac{\mathbb{I}[r < r^i(\mathbf{x}) \leq r + \Delta r]}{\Delta r}. \tag{3.16}$$

Figure 3.A.7 shows the PDFs of the mixing and reaction rates for the different hydraulic conductivity fields. The average mixing and reaction rates $\overline{\chi}$ and $\overline{r}$ are given by

$$\overline{\chi} = \int d\chi \chi p_\chi(\chi) = \frac{1}{N}\sum_{i=1}^{N}\frac{1}{A_m}\int_\Omega dxdz\chi^i(\mathbf{x}) \tag{3.17}$$

$$\overline{r} = \int dr r p_r(r) = \frac{1}{N}\sum_{i=1}^{N}\frac{1}{A_m}\int_\Omega dxdz r^i(\mathbf{x}) \tag{3.18}$$

3.A.4.3 Horizontal Stratification

In order to provide an example for a reaction and mixing pattern that would result from horizontal stratification, we simulate seawater intrusion with a multi-Gaussian field described with an infinite longitudinal correlation length and a transverse correlation length of 10 m. This was performed for log-conductivity variances of $\sigma^2_{\ln k}$=1 and 3 with a K_g of 5e-4 m/s. Note that we still idealise all layers as the same carbonate sequence, only with different hydraulic conductivities.

3.A.4.4 Flow deformation

The deformation of the field largely controls the presence of enhanced mixing and reactions. The deformation rate tensor is defined by

$$\boldsymbol{\epsilon}(\mathbf{x}) = \begin{pmatrix} \frac{\partial v_x(\mathbf{x})}{\partial x} & \frac{\partial v_x(\mathbf{x})}{\partial z} \\ \frac{\partial v_z(\mathbf{x})}{\partial x} & \frac{\partial v_z(\mathbf{x})}{\partial z} \end{pmatrix} \tag{3.19}$$

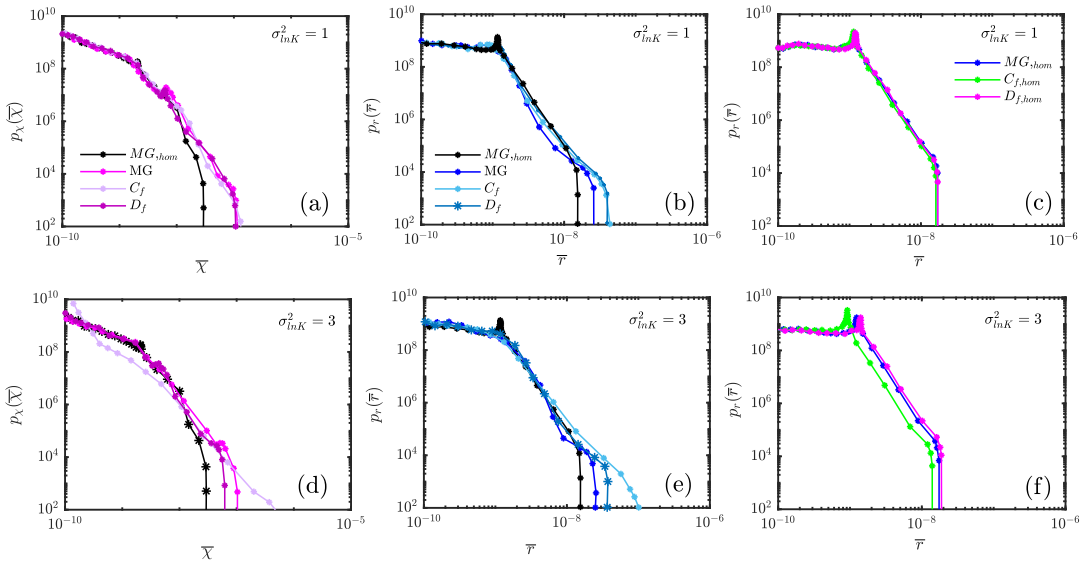

FIGURE 3.A.7: PDF of the effective local mixing and reaction rates for the homogeneous field, the multi-Gaussian field (MG_{eff}), the connected field ($C_{f,eff}$) and the disconnected field ($D_{f,eff}$) for variances a-b) $\sigma^2_{lnK} = 1$ and c-d) $\sigma^2_{lnK} = 3$.

The strain tensor is given by $\mathbf{\Theta}(\mathbf{x})$

$$\mathbf{\Theta}(\mathbf{x}) = \frac{1}{2}\left[\mathbf{\Theta}(\mathbf{x}) + \mathbf{\Theta}(\mathbf{x})^\top\right], \tag{3.20}$$

where the superscript $\top$ denotes the transpose. The strain rate $\sigma(\mathbf{x})$ is defined as the determinant of the strain tensor,

$$\sigma(\mathbf{x}) = \epsilon_{11}^2 + (\epsilon_{12} + \epsilon_{21})^2. \tag{3.21}$$

It is a measure for the local stretching of a fluid element.

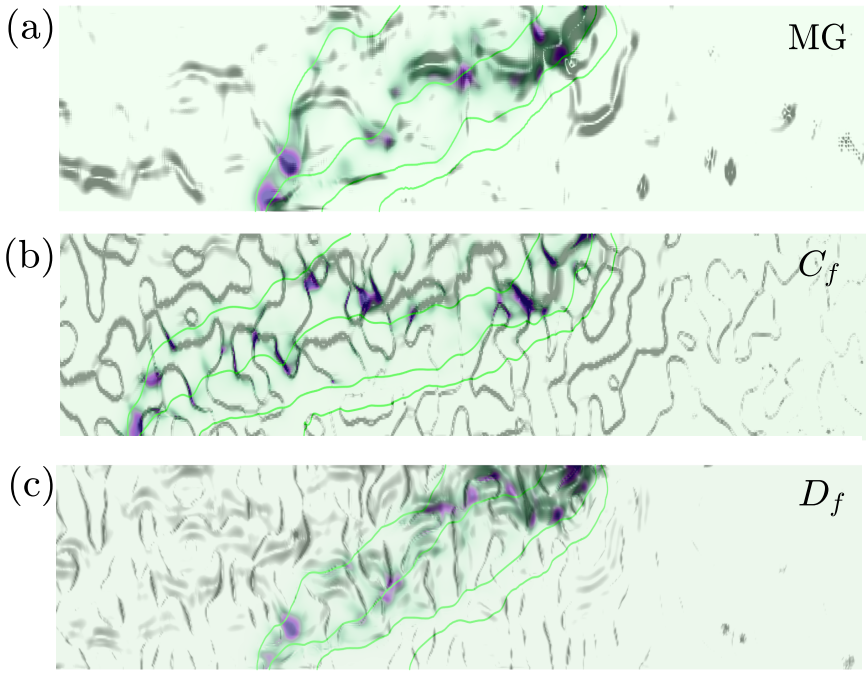

FIGURE 3.A.8: Example of reaction rate maps overlying the distribution of strain rates for σ^2_{lnK} = 3 for a) multi-Gaussian field (MG), (b) the connected field (C_f) and (c), the disconnected field (D_f).

CHAPTER 4

Mixing dynamics across the salt-freshwater interface [1]

ABSTRACT

Mixing processes in salt-freshwater interfaces have important implications for water quality and biogeochemical reactions in coastal aquifers. Hot spots of mixing and chemical reactions along the salt-freshwater interface exert critical controls on the transport and transformation of nutrients and contaminants in coastal ecosystems. We investigate mixing dynamics along salt-freshwater interfaces using numerical simulations of steady state density-dependent flow and transport. We use these insights to derive an approximate analytical solution that quantifies the evolution of the mixing width along the interface and predicts the development of mixing hot spots induced by stretching in the accelerating flow of the discharge zone. These findings demonstrate that non-uniform flow fields, inherent to seawater intrusion in coastal aquifer, result in spatially variable mixing behaviour along the interface. Our model captures simulated mixing dynamics over a range of freshwater flows and dispersivities and provides a new framework for understanding and modelling mixing and reaction processes in coastal aquifers.

[1] This Chapter is based on the paper "K.De Vriendt et al. - Mixing Dynamics across the Salt-Freshwater Interface, *in preparation*".

4.1 Introduction

Coastal aquifers are some of the most vulnerable groundwater resources sustaining dense coastal populations globally (Ferguson and Gleeson, 2012). These subsurface environments are subject to significant anthropogenic pollutants that negatively impact ocean ecosystems (Slomp and Cappellen, 2004; Moore, 2010; Kroeger and Charette, 2008). Moreover, their inherently non-stationary flow dynamics on different temporal scales (tides, seasons and glacial cycles) leads to a range of geochemical processes across coastal landscapes. A notable example is mixing-enhanced carbonate dissolution and karstification processes in coastal zones (Back et al., 1986b). Over large time scales, Seawater Intrusion has acted as primary mechanism to observable land features such as the formation of 'Flank Margin Caves' near the mixing discharge zone (Mylroie and Carew, 1990; Back et al., 1979), or cave and conduits formation in Bermudas (Palmer, 1992), Bahamas (Palmer and Williams, 1982) and Yucatán (Back et al., 1986a). Freshwater discharge in coastal aquifers has also been associated with a variety of other biogeochemical reactions in beach environments. A well-known example is the enhanced iron oxide precipitation in Waquiot Bay (termed 'iron curtain') Charette and Sholkovitz, 2002; Spiteri et al., 2008a which attenuates contaminants such as phosphates and arsenic. Such reactions may hold a strong propensity in regulating the flux of terrestrial pollutants towards coastal marine ecosystems.

While ideal reaction kinetics and ideal redox conditions are surely strong precursors to these reactive hotspots, their interplay with the non-uniform velocity field and mixing dynamics in coastal aquifers remains poorly understood. Sanford and Konikow (1989) and Rezaei et al. (2005) demonstrated numerically that the mixing of salt and freshwater in coastal aquifers induces local dissolution hotspots at both the discharge zone as well as at the toe of the salt-water wedge. Studies have since also highlighted the importance of heterogeneity across the salt-freshwater interface (SFI) in generating local reaction hotspots (De Vriendt et al., 2020).

A key challenge for capturing mixing and reaction hot spots is to quantify the width of the mixing zone between freshwater and saltwater. Under steady-state and homogeneous conditions, mixing across the SFI is dominantly controlled by density effects and transverse dispersion (Paster and Dagan, 2007; Abarca et al., 2007). Laboratory-scale experiments (e.g., Abarca et al., 2007; Goswami and Clement, 2007; Robinson et al., 2015; Yoshihiro Oda, Tamio Takasu, Hirashi Sato, Atsushi Sawada, 2010) and some field observations (Paster et al., 2006), have shown narrow mixing zones. On the other hand, large-scale field studies have observed mixing zones ranging from tens to hundreds of meters (Kroeger and Charette, 2008; Spiteri et al., 2008a; Kim et al., 2007; Price et al., 2003; Langevin, 2003; Barlow, 2003). Widening of the mixing zones in real-world coastal aquifers has mainly been attributed to transient effects such as tides (e.g., Ataie-Ashtiani et al., 1999; Pool et al., 2014; Pool et al., 2015), as well as heterogeneity (Abarca Cameo, 2006; Kerrou and Renard, 2010; Lu et al., 2013) or kinetic mass transfer (Lu et al., 2009b). However, while all these investigations provide valuable insight into water-resources management and general mixing dynamics, in these studies the width of the mixing zone has been addressed mainly through averaging across the saltwater-freshwater interface (e.g., Abarca et al., 2007; Kerrou and Renard, 2010; Lu et al., 2013; Pool et al., 2014). Hence it is not known how the mixing width varies across the interface and what are the mechanisms driving the formation of mixing hot spots, which may dictate reactive processes.

Recent theoretical developments have demonstrated that fluid stretching in non-uniform flow fields can lead to increased local mixing and reactions (e.g., Le Borgne et al., 2014; Bandopadhyay et al., 2018). Here, we apply these concepts to investigate the impact of flow on mixing dynamics across the SFI. Modifying the flow rate pushes the SFI seaward or landward, thereby respectively elongating or compressing the interface and changing its geometry.

We quantify the evolution of the mixing width along the SFI for a range of freshwater flow rates and dispersivities and relate these dynamics to the stretching rate driven by non-homogeneous flow along the interface. We derive an approximated analytical solution which provides accurate predictions of the mixing dynamics along the SFI and allows understanding and modeling the development of mixing hot spots. We discuss the implications of our findings regarding their impact on mixing and reaction rates in coastal aquifers.

4.2 Governing Equations

4.2.1 Flow and Transport

We study mixing under steady variable density flow in two-dimensional heterogeneous coastal aquifers. Density-dependent flow is described by the Darcy equation

$$\mathbf{q} = -K\left[\nabla h_f + \frac{\rho - \rho_f}{\rho_f}\mathbf{e}_z\right], \tag{4.1}$$

where $\mathbf{q}$ is the specific discharge, K is the hydraulic conductivity, h_f the equivalent freshwater head, ρ the fluid density, ρ_f the density of freshwater and $\mathbf{e}_z$ is the unit vector in y-direction. Fluid mass conservation in the absence of sources and sinks implies $\nabla \cdot \rho\mathbf{q} = 0$. The fluid density is assumed to be linearly dependent of the salt mass fraction ω (mass of salt dissolved per unit mass of fluid) given by $\rho = \rho_f[1 + \epsilon' c]$, where ϵ' is the buoyancy factor given by $\epsilon' = (\rho_s - \rho_f)/\rho_f$ with ρ_s the density of seawater and c is the normalized salt concentration defined as $c = \omega/\omega_s$ with ω_s the salt mass fraction of seawater. The concentration c evolves according to the advection dispersion equation, which in steady state reads as

$$\mathbf{q} \cdot \nabla c - \nabla \cdot [\mathbf{D} + \phi D_m]\nabla c = 0, \tag{4.2}$$

with $\mathbf{D}$ the dispersion tensor Bear (1988), D_m molecular diffusion and ϕ porosity. The flow and transport equations in dimensionless form read, respectively, as

$$\frac{\partial^2 h'_f}{dx'^2} + \frac{\partial^2 h'_f}{dy'^2} + \mathsf{Ng}\frac{\partial c}{\partial y'} = \frac{\mathbf{q}'\epsilon \cdot \nabla' c}{1 + \epsilon' c}, \tag{4.3}$$

$$\mathbf{q}' \cdot \nabla' c - \nabla' \cdot [\mathsf{Pe}_I^{-1}\mathbf{D}' + \mathsf{Pe}_{II}^{-1}\mathbf{I}]\nabla' c = 0, \tag{4.4}$$

where dimensionless coordinates (primed variables) are defined in terms of the aquifer thickness b, the dimensionless Darcy's velocity in terms of the specific freshwater discharge from inland q_f and the dimensionless equivalent freshwater head is defined as $h'_f = hK/q_f b$. The gravity number, Ng indicates the competition between gravity-induced flow and forced convection and is given by $\mathsf{Ng} = K\epsilon'/q_f$. The strength of coupling between flow and salt transport increases with Ng (Dentz et al., 2006). The dimensionless dispersion tensor is defined as $D'_{i,j} = \delta_{i,j} r_\alpha |\mathbf{q}'| + (1 +$

$r_\alpha)(q'_i q'_j)/|\mathbf{q}'$, where $r_\alpha = \alpha_t/\alpha_l$ with α_l and α_t the longitudinal and transverse dispersivities, respectively (see Abarca et al., 2007). Pe_I and Pe_{II} are two Pèclet numbers which describe the relative importance of advective and dispersive and diffusive transport mechanism (Abarca et al., 2007) given by

$$\mathrm{Pe}_I = \frac{b}{\alpha_t} \qquad (4.5) \qquad\qquad \mathrm{Pe}_{II} = \frac{q_f b}{\phi D_m}. \qquad (4.6)$$

In this study we change both the fresh water flux, q_f and longitudinal and transverse dispersivities, α_l and α_t respectively. Therefore, the dynamics of the problem are governed by both the Pèclet number, Pe and the gravity number, Ng.

4.2.2 Numerical model

We consider a shallow coastal aquifer of constant thickness b and length L extended offshore with a specific freshwater discharge from inland q_f. The connection with the sea is represented as a prescribed head along the offshore model top and the offshore vertical boundaries. The base case scenario used in this study is largely inspired from the study of Spiteri et al. (2008a). Note that, as discussed in the following the general relationship between fluid stretching and mixing dynamics derived from this numerical example are expected to apply more generally over a large range of coastal aquifer systems.

TABLE 4.1: Literature derived values of coastal aquifer properties

Publication	**Type**	K [m/s]	q_f [m/d]	b [m]	α_l (m)	α_t (m)
Paster (2010)	Field	1.73×10^{-3}	-	600-1000	-	0.04
Abarca et al. (2013)	Field	1.74×10^{-4}	2.3×10^{-2}	11	0.1	0.01
Heiss and Michael (2014)	Field	2.9×10^{-4}	-	12-18	0.15	1.5×10^{-2}
Spiteri et al. (2008a)	Field	6.86×10^{-4}	0.13	11	0.5	5×10^{-3}
Robinson et al. (2007)	Field	1.16×10^{-4}	6.6×10^{-2}	30	0.5	5×10^{-2}
Abarca and Clement (2009)	Experimental	1.2×10^{-2}	-	0.3	5×10^{-4}	5×10^{-5}
Robinson et al. (2015)	Experimental	2.3×10^{-3}	-	0.14	1×10^{-3}	5×10^{-4}
Masahiro et al. (2018)	Experimental	-	-	0.25	7×10^{-4}	2.5×10^{-5}

Numerical studies have shown that the longitudinal and transverse dispersivities α_l and α_t are important parameters when considering mixing dynamics and the width of the SFI (e.g. Abarca et al., 2007; Nick et al., 2013; Spiteri et al., 2008b). Unlike the evolution of plumes over time, there exists no clear criterion for assigning the value of dispersivities (Rezaei et al., 2005). This is further confounded by the fact that it is a parameter that is generally difficult to measure and is scale dependent (Neuman, 1990). Numerical studies of field sites often adopt arbitrarily large dispersivity values in order to overcome numerical dispersion caused by poor grid refinement in numerical codes (Paster, 2010), or to artificially incorporate the effects of tides and heterogeneity (Werner et al., 2012). However, large dispersion likely lead to an overestimation of mixing induced reaction rates. In this study, longitudinal and transverse dispersivities used in the simulations were selected based on literature values where field data has previously been calibrated by numerical simulations (Table 4.1). In these examples, Pe_I and Pe_{II} are consistently larger than unity as typically found in field studies and laboratory experiments.

For the range of freshwater fluxes evaluated in this study, the Pèclet number (for lowest to highest q_f) ranges between 4.82×10^3 - 1.16×10^4, while the gravity number ranges between 17.3-7.2.

TABLE 4.2: Parameters used in numerical simulations

Parameter	Value	Description
$K[ms^{-1}]$	1e-4	Hydraulic conductivity
$b[m]$	10	aquifer thickness
$L[m]$	100	aquifer Length
$\phi[-]$	0.3	porosity
$\alpha_l[m]$	0.1-0.5	Longitudinal dispersivity
$\alpha_t[m]$	0.01-0.05	Transverse dispersivity
$q_f[md^{-1}]$	0.0125-0.03	freshwater flux
D_m $[m^2/s]$	1e-9	Molecular diffusion
$\epsilon'[-]$	0.025	Buoyancy factor

4.2.3 Mixing Measures

We define four measures to gain a quantitative understanding of local mixing along the SFI: the mixing width (e.g. Le Borgne et al., 2015), the scalar dissipation rate (e.g. Le Borgne et al., 2010), the gradient of concentration (e.g. Bandopadhyay et al., 2018) and the rate of strain (e.g. De Barros et al., 2012). First, the width of the mixing zone normal to the principal direction of flow is determined. To this end, we compute the distance across $c(1-c)$ at half its maximum, denoted here as κ (see inset of Fig. 4.2.1a). Due to the proximity of the toe to boundary, the full width at half maximum cannot be attained directly at the bottom and are omitted. For a symmetric profile of $c(1-c)$, we can relate this back to the square root of the second central moment (variance) of $c(1-c)$,

$$s = \frac{\kappa}{2\sqrt{2\ln 2}}, \tag{4.7}$$

where s defines the mixing width. The local mixing rate is quantified by the scalar dissipation rate (Fig. 4.2.1c),

$$\chi_l = \nabla c \cdot \left(\mathbf{D}\nabla c\right). \tag{4.8}$$

For mixing-limited reactions, this measure is directly proportional to the reaction rate De Simoni, 2005. Additionally, the gradient of concentration(see Fig. 4.2.1b) is evaluated in order to emphasize the role of (velocity-dependent) dispersion by comparison with the scalar dissipation rate.

$$\theta_l = \|\nabla c\|, \tag{4.9}$$

where $\|\cdot\|$ denotes the L^2-norm. All quantities are evaluated along the curvilinear length of the interface, where $z = 0$ directly at the toe. We compare the scalar dissipation rate and the gradient of concentration by evaluating their maximum values along the length of the interface, denoted by θ_m and χ_m, respectively. Finally, we evaluate the deformation rate tensor to determine zones of enhanced fluid strain across the interface,

$$\boldsymbol{\epsilon} = \begin{pmatrix} \frac{\partial v_x}{\partial x} & \frac{\partial v_x}{\partial z} \\ \frac{\partial v_z}{\partial x} & \frac{\partial v_z}{\partial z} \end{pmatrix}, \tag{4.10}$$

and the rate of strain (Okubo, 1970; Weiss, 1991; De Barros et al., 2012) to quantify high local stretching and shear deformation (see Fig. 4.3.2d),

$$\Theta_\zeta = \alpha^2 + \sigma^2, \tag{4.11}$$

where $\alpha = 2\epsilon_{11}$ is the stretching deformation and $\sigma = \epsilon_{21} + \epsilon_{12}$ is the shear deformation.

Figure 4.2.1 shows the general mixing and flow features for a salt water wedge at steady state. Salt and freshwater start mixing at the toe at the bottom of the aquifer (Figure 4.2.1e). Note that the streamlines converge at the fresher portion of the mixing zone, resulting in an oblique stagnation point and a resulting dividing streamline. This stagnation point is associated with stronger local concentration gradients and scalar dissipation rates then would be expected under uniform flow conditions, and results in locally enhanced strain (Figure 4.2.1d). Along the interface, scalar gradients are oriented tangential to the line of zero horizontal gradient. Towards this line, velocities fall sharply resulting in a sheared interface. Thus, the resulting profile of θ_l normal to the interface is significantly asymmetric (see inset in Figure 4.2.1), with the highest values occurring along the zero horizontal gradient before dropping off steeply towards the high concentration isolines. Note that even in simulations with larger dispersivities, that enlarge the SFI, specifically at the toe (e.g. Abarca et al., 2007), the local mixing behaviour along the interface is still preserved (see Appendix Section 1.). As we move along the interface from the aquifer bottom, concentration gradients are attenuated by dispersion leading to a decrease in the local scalar dissipation rate. Close to the discharge zone, salt water streamlines approaching the interface become dominantly aligned with the mixing interface (Oz et al., 2015) (Figure 4.2.1g) and the interface becomes compressed due to accelerating flow. As a result, the discharge zone shows enhanced strain and local mixing.

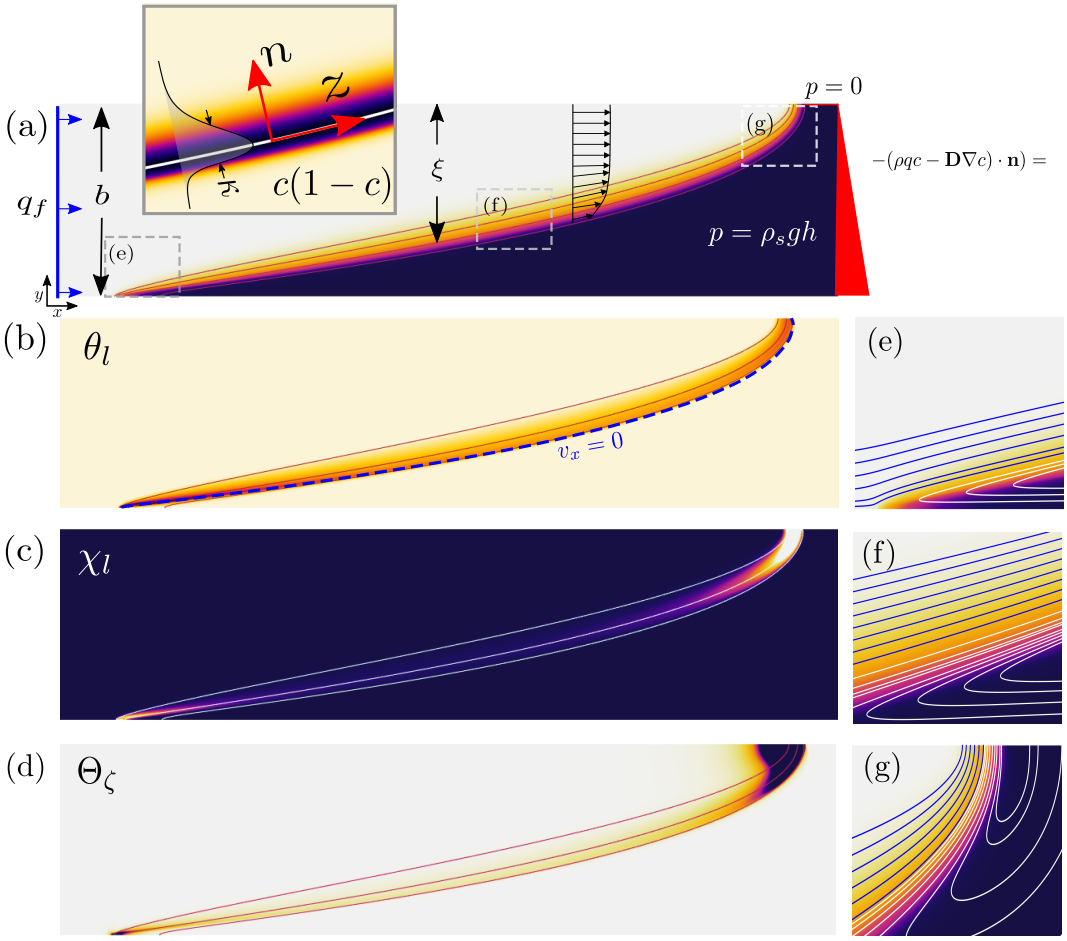

FIGURE 4.2.1: (a) Steady state simulation result for q_f = 2.5 m/d. (b) Schematic representation of seawater intrusion problem and associated boundary conditions. (c) The normalized salt concentration c. (d) The concentration gradient. (e) The Scalar dissipation rate.(e-g) Zoomed in normalized concentration overlain by the flow streamlines.

4.3 Control of flow on mixing dynamics

In order to assess the main factors controlling mixing across the SFI, we first investigate the effect of freshwater flow rate (quantified by Pe_{II} and Ng) on the mixing dynamics. Since the diffusion coefficient and buoyancy factor are fixed in our analysis, we limit our analysis by evaluating the mixing measures with respect to Pe_{II}. It should nevertheless, be noted that the gravity number plays a fundamental role in the movement of the wedge and has also been shown to play an important role on mixing in stable stratification problems (Dell'Oca et al., 2018).

The local mixing widths along the interface for each q_f are shown in Figure 4.3.1(a-c). The SFI is initially most narrow at the toe where the two fluids initially mix. From here s broadens to a maximum value, s_m before narrowing again towards the discharge zone. A similar behaviour is observed from the experiment of (Abarca and Clement, 2009), where the delineated mixing width was found to be narrowest at the toe followed by a broadening of the mixing zone upwards. While it has been speculated that under velocity-dependent dispersion the mixing width should increase with increasing freshwater flux (Werner et al., 2012), we show in Figure 4.3.1a) that the overall interface is smaller at higher Pe_{II}. In Figure 4.3.1c we further show that all curves can be collapsed by scaling s by s_m and z by the interface length, L_i. L_i grows roughly proportional to the increase in the freshwater flux, $L_i \propto \mathrm{Pe}_{II}^{-1}$ while $s_m \propto \mathrm{Pe}_{II}^{0.4}$. The mixing width grows diffusively as $s \propto z^{1/2}$ before transitioning to a decay after reaching its maximum value s_m.

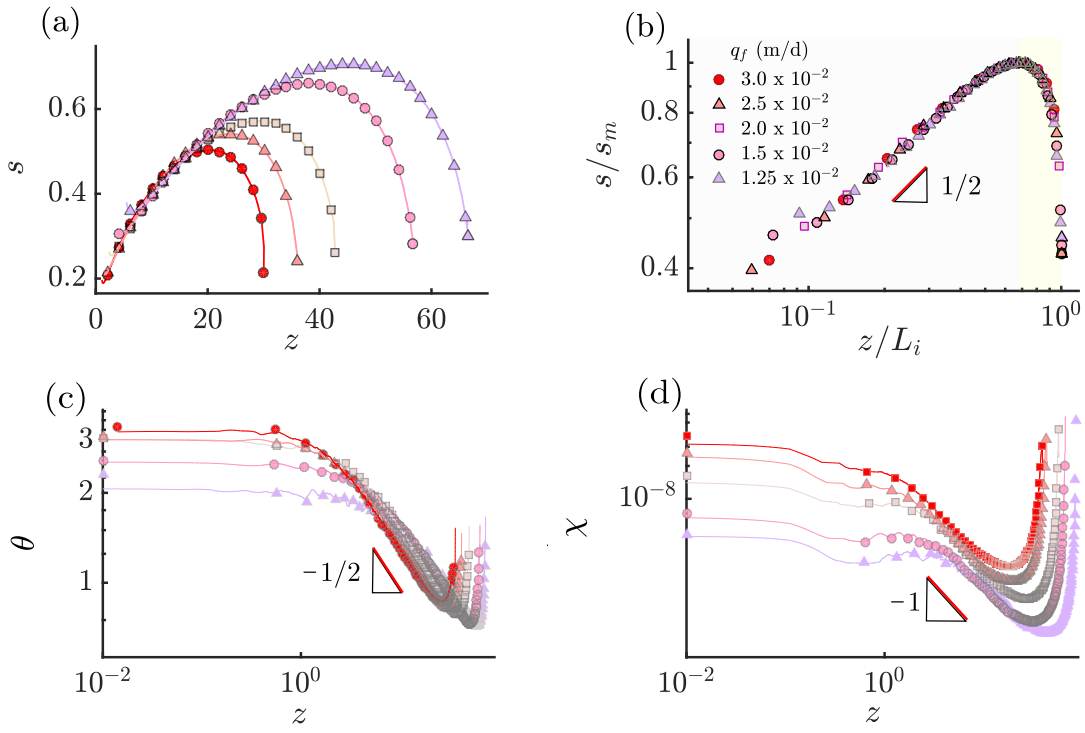

FIGURE 4.3.1: (b) Mixing width along the interface for each q_f. (c) Mixing Width scaled by the maximum interface width s_m and the interface length, L_i.(d) Maximum concentration gradient, θ_m along the interface. (e) Maximum Scalar dissipation rate, χ_m along the interface.

The diffusive growth of the mixing width in the first regime suggests that transverse dispersion is the main mechanism driving mixing in this regime. This is conceptually similar to the mixing behaviour observed when two initially segregated solutes come into contact. Under this hypothesis, the mixing width would evolve as $s = \sqrt{D_t t}$ where t is the time available for mixing from the toe to a given position z along the interface and D_t is the transverse dispersion coefficient, $D_t = D_m + \alpha_t v_a$. To evaluate the mixing width along z, we note that $t = z/v_a$. Where v_a is the average linear velocity dictated by the freshwater flux. We further simplify by omitting D_m such that mechanical dispersion prevails and so $D = \alpha_t v$. Accordingly, the growth of s along the interface can be given as,

$$s \approx \sqrt{\alpha_t z}, \tag{4.12}$$

which is consistent with the growth of the interface for a range of dispersivities (see Appendix Figure 4..1). The dynamics of the local maximum concentration gradient and scalar dissipation rate are shown respectively in Fig. 4.3.1c and d. At the toe, θ and χ both grow with Pe_{II} before decaying. At the toe we find that $\theta \propto \mathrm{Pe}_{II}^{1/2}$, suggesting enhanced compression resulting from the locally converging flow (see Appendix Figure 4..2c). Then, the mixing rate quickly transition to a behaviour driven by dispersive growth, leading to a decay $\theta \propto z^{-1/2}$ and $\chi \propto z^{-1}$. These evolutions are indeed recovered when approximating the gradient as $\nabla c \sim c/s$ and assuming that s grows diffusively (eq. 4.12). At the transition zone, the interface begins to compress and we find θ_m to scale close to $Pe_{II}^{1/4}$. The mixing rate however, decreases strongly with a reduction of q_f, scaling as $\mathrm{Pe}_{II}^{3/2}$ (see Appendix Figure 4..2f).

The transition between dispersive growth and compression that occurs as z_m, corresponds to the crossover between two competing mixing mechanisms. In this particular problem, dispersive growth is overcome by accelerating flow towards the discharge zone which stretches the interface, thus narrowing the mixing width. A similar behaviour was observed by Eeman et al. (2011) when investigating upwelling of saline water across a freshwater lens into a ditch. The authors found that despite increasing velocities towards the outlet, the mixing width continued to narrow due to converging streamlines.

To derive approximated analytical solutions for the mixing width at the cross over distance and in the compression regime, we consider the sharp interface solution of Glover (1959) that predicts the position of the interface as,

$$\zeta^2 = \frac{2Q_f}{K\epsilon'} z + \frac{Q_f^2}{K^2 \epsilon'^2}, \tag{4.13}$$

where $Q_f = q_f b$, recalling q_f is the freshwater flux and b is the domain height. To account for the influence of mixing we incorporate the empirical correction factor for the buoyancy factor, ϵ', as introduced by Pool (2011),

$$\epsilon = \epsilon' \left[1 - \left(\frac{\alpha_t}{b} \right)^{1/4} \right]^{-1}. \tag{4.14}$$

We implement the factor $1/4$ suggested by Lu and Werner, 2013 as it provides a better fit against the numerical simulations (see Figure 4.3.2a). We transform equation 4.13 such that the coordinate origin begins at the toe. In order to do so, we must define the position of the toe, z_t. At the toe position where $\zeta = b$ and using

equation 4.13, we can solve for z_t which is estimated as,

$$z_t = \frac{-b(q_f^2 - K^2\epsilon^2)}{2Kq_f\epsilon}. \tag{4.15}$$

After inserting this term into 4.13 and rearranging we obtain,

$$\xi^2 = \frac{-2b}{\mathsf{Ng}'}z + b^2. \tag{4.16}$$

To simplify the expression further, we have substituted in a modified gravity number, $\mathsf{Ng} = K\epsilon/q_f$. We approximate the velocity along the interface as the average velocity in the freshwater section,

$$v = \frac{Q_f}{\sqrt{\frac{-2b}{\mathsf{Ng}'}z + b^2}}. \tag{4.17}$$

The stretching rate resulting from flow acceleration along the interface can therefore be given by the velocity gradient along the interface,

$$\gamma = \frac{dv}{dz} - \frac{q_f b^2}{\mathsf{Ng}'\left[-\frac{2b}{\mathsf{Ng}'}z + b^2\right]^{3/2}} \tag{4.18}$$

In Figure 4.3.2b we plot the predicted stretching rate along z. The results show good agreement with the numerical model with no fitting parameter. Discrepancies can be seen at the toe where there is local deceleration due to the stagnation zone. In addition, since we assume flow is forced through a finitely smaller outlet rather than a gap, γ is overestimated as it asymptotes near the outlet. The stretching rate shows a transition between an approximately exponential increase in γ and a super exponential increase of γ. The transition position z_m is located approximately at the position where the stretching starts increasing sharply, which induces the mixing width compression. The dynamics of the mixing scale may be understood by considering the local Batchelor scale (Batchelor, 1959) given by,

$$s_b = \sqrt{\frac{D}{\gamma}}. \tag{4.19}$$

The Batchelor scale is the characteristic mixing scale for systems characterized by a stretching rate and defines the mixing scale at which diffusion is balanced by stretching (Villermaux, 2019). Here the stretching rate is constant at a given position but varies spatially. Thus, the Batchelor scale may be locally reached if the local travel time is larger than the characteristic mixing time needed to reach the Batchelor scale.

Given the nature of stretching towards the outlet, dispersive growth should be arrested when the mixing distance $\sim v/\gamma$ becomes sufficiently small that a local Batchelor scale can be established. Notice for example that even though velocities along the interface increase which would suggest increasing mixing width due to velocity-dependent dispersion, here it is compressing instead . This condition is only met so long as $s_b < s$. In Figure 4.3.2c, we see that s_b is initially larger than s, however shifts just after z_m, after which the mixing width shows good agreement

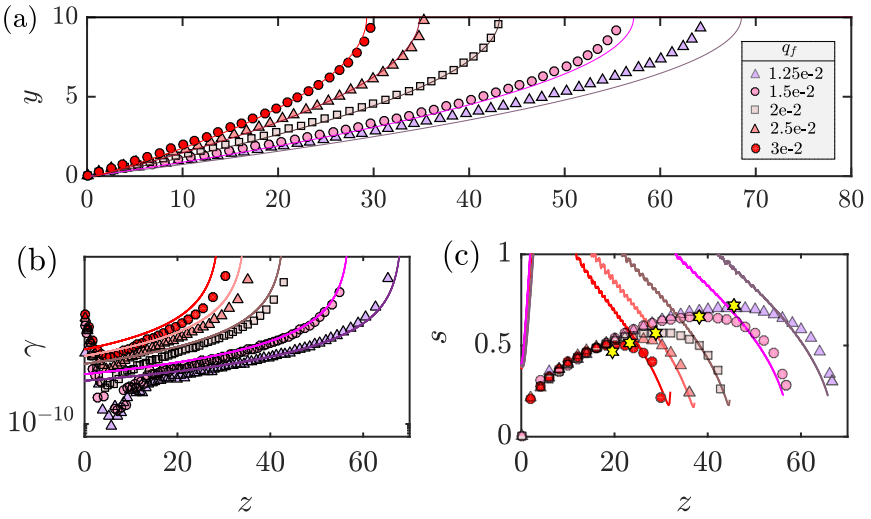

FIGURE 4.3.2: (a) Saltwater interface defined by the 50% concentration isoline. Symbols denote numerical simulation results and solid lines denote the Glover solutions.(b) Numerically determined Stretching rate and stretching rates determined by Glover solution (solid lines) (c) Numerical mixing width compared against the numerically derived batchelor scale (solid lines) and approximated mixing distance and width (pentagon) .

with s_b. This leads us to an expression for s_b,

$$s_b = \left[\alpha_t \left(b\mathrm{Ng}' - 2z\right)\right]^{1/2}. \tag{4.20}$$

At the z_m, dispersive broadening is balanced by the stretching rate. Equating (4.12) and (4.20) yields the mixing distance,

$$z_m = \frac{b\mathrm{Ng}'}{3}. \tag{4.21}$$

Substituting (4.21) into (4.16) yields the depth at which the transition occurs,

$$\xi_m = \frac{b}{\sqrt{3}}. \tag{4.22}$$

Over the range of q_f used in the base case, we find that z_m/L_i ranges between 0.68-0.67 while ξ_m/b is fixed at 0.57 as it is only dependent on the domain height. We can now approximate the maximum mixing width by substituting (4.22) into (4.12). This, however overpredicts s_m due to the cross over distance. We find that for the numerical simulations under consideration a factor 3/4 is required for sufficient representation of s_m.

$$s_m \approx \frac{3}{4}\sqrt{\alpha_t z_m}. \tag{4.23}$$

It should be emphasized that the Glover solution used in this study is simply a means to approximate the position of the interface for this given problem. Naturally, for problems with different boundary conditions, such as in experimental sand tanks, the interface position and and velocity field, may deviate from the idealized scenario studied here and therefore require further evaluation.

In Figure 4.3.12c-d we saw that the local maximum concentration and scalar gradients are not uniform along the interface. In general, we see from Figure 4.3.1b that s also compresses to half the size of s_m. By this simple metric, given that $\nabla c \sim c_m/s$, the concentration gradients at the outlet alone is already twice as large as at the transition point. As for the mixing rate, the ratio of χ at the outlet compared to its local minimum, which we define as the mixing enhancement, ME, grows with a decrease in q_f. For the lowest q_f simulation in particular, ME is approximately 100, which suggests accelerating flow can drastically enhance local mixing. From the expression provided in (4.9), we find that the mixing enhancement, can be estimated by the ratio of the velocity at the discharge zone, v_d to the velocity measured at the transition zone, v_{zm}, such that $ME \approx 4(v_d/v_{zm})$.

4.4 Implications on coastal biogeochemistry and outlook

Enhanced mixing rates across the SFI resulting from variable density induced non-uniform flow, may strongly influence our understanding of mixing-limited reactions in coastal landscapes. This is particularly relevant when evaluating the chemical composition of submarine groundwater discharge (SGD), which is often altered by biogeochemical reactions resulting from the mixing of salt and freshwater (Moore, 1999). Given that high concentrations of nutrients in coastal groundwater have been associated with eutrophication and the onset of algal blooms (Valiela et al., 1990; LaRoche et al., 1997), understanding mixing dynamics that lead to the transformation of chemicals along the interface warrants careful consideration.

Strong mixing at the discharge zone is of particular interest as it has been linked to an array of geochemical activity (e.g. Mylroie and Carew, 1990; Charette and Sholkovitz, 2002; Kroeger and Charette, 2008). A notable example is the precipitation of iron oxide in Waquiot Bay, USA (Charette and Sholkovitz, 2002; Spiteri et al., 2006). According to Spiteri et al. (2008a), given the efficiency of iron-oxides in attenuating inorganic phosphate, these natural geochemical barriers could act to regulate nutrient dynamics prevent coastal eutrophication. It has also been shown to attenuate arsenic (Bone et al., 2006; Hun et al., 2009). Given the proximity of the discharge zone to the surface, it is also often subject to favourable redox conditions, for which the fate of groundwater nitrogen and phosphorous is highly dependent (Slomp and Cappellen, 2004). In the case of oxidative iron precipitation, a constant source of oxygen from wave and tidal action (e.g. Ullman et al., 2003; Kroeger and Charette, 2008; Charbonnier et al., 2013) in addition to strong mixing may explain the strong localization of iron oxides. It has also been suggested that even in coastal aquifers with low oxygen concentration, pH gradients across the SFI may act as the main driver in the precipitation (Spiteri et al., 2006). The non-trivial interplay between transport and chemical reactions at the discharge zone was also highlighted by Rezaei et al. (2005) in their modelling of calcite dissolution across the SFI. They emphasized that the saturation index calculation provides information of where calcite may be most undersaturated. However, it does not predict the location and magnitude of dissolution, for which 2D simulations are required. In their particular study, although calcite is always found to be most under saturated in the fresher portion of the mixing zone, dissolution was always largest along the saline portion of the discharge zone due to the active convection cell resulting in strong dispersive mixing.

This study may also provide general insight into the behaviour of mixing across the SFI resulting from a change in inland fluxes or sea-level rise, both of which act to

shift the mixing interface further inland or seaward. If we consider the example of mixing-induced calcite dissolution in carbonate aquifers, our findings may elucidate the shaping of coastal landscapes over large time scales. Over large time scales, the movement of the wedge to new quasi-steady state positions may influence the local and global reactivity across the interface. For example, preliminary results by Pool et al. (2019a) found that global calcite dissolution was largest when the sea level was highest, however locally they are largest when the sea level was lowest. Therefore, over long time scales, the distribution and pattern of preferential dissolution may change significantly. While the movement of the wedge seaward and landward due to transient processes result in different flow patterns (Chang and Clement, 2012b), and thus mixing mechanisms , it is clear that even in simple steady state scenarios, the interplay between transport and chemical reaction are not trivial.

4.5 Conclusion

Our study has examined mixing dynamics for seawater intrusion under steady-state conditions. Evaluation of the mixing width along the salt-freshwater interface has highlighted several mixing processes that are influenced by non-uniform flow from the mixing of saline and freshwater bodies. We find that the mixing width initially grows due to transverse dispersion up to some mixing distance where it then re-compresses due to accelerating flow towards the discharge zone. Interface compression near the outlet is accompanied by enhanced concentration gradients and mixing rates. We also attribute stronger mixing rates near the interface toe to enhanced local compression resulting from opposing flow which results in a stagnation point. Decreasing the freshwater flux results in the saltwater wedge to intrude further inland, which in turn increases the interface length. This allows the interface width to grow larger before narrowing near the outlet. Although this results in lower mixing rates along the center of the interface, mixing is still strongly enhanced near the outlet, which is comparable to the high freshwater flux scenarios. Furthermore, using a sharp interface analytical model, we derive simple analytical solutions that are capable of describing the compression of the interface near the outlet.

While it is clear that our homogeneous model may not capture the mixing behaviour of the SFI in more complex flow systems, e.g., in the presence of heterogeneity, 3D effects and transient forcings, it sheds light on the basic mechanisms dictating mixing across the SFI for which future work may build upon.

Appendix

In Figure 4..2, we see that increasing α_l has negligible impact on the overall mixing width compared to α_t. For example, increasing α_l by a factor of 5 for α_t = 0.01 m, results in almost no change in s_m. This is not surprising given the bulk of the interface resides where flow is tangential to the principal direction of flow. Flow from the seaside however approaches the interface orthogonally with velocities approximately an order of magnitude lower than the freshwater flux. This is by no means suggesting α_l does not play a role. (Abarca et al., 2007) showed that increasing α_l leads to the seaward displacement of high concentration isolines, with a particlarly strong influence at toe. Therefore for larger values of α_l table 4.2, equation 4.12) may no longer provide provide a good fit. For small dispersivities however, α_t alone seems to sufficiently characterizes the growth of s.

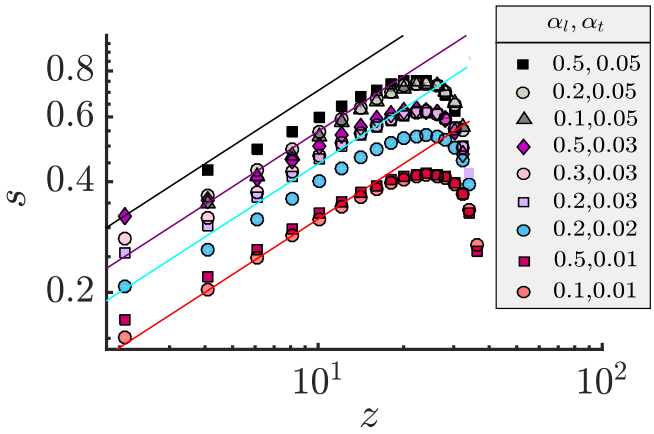

FIGURE 4..1: Mixing width for varying dispersivities. Solid lines indicate interface growth for the numerical transverse dispersivity.

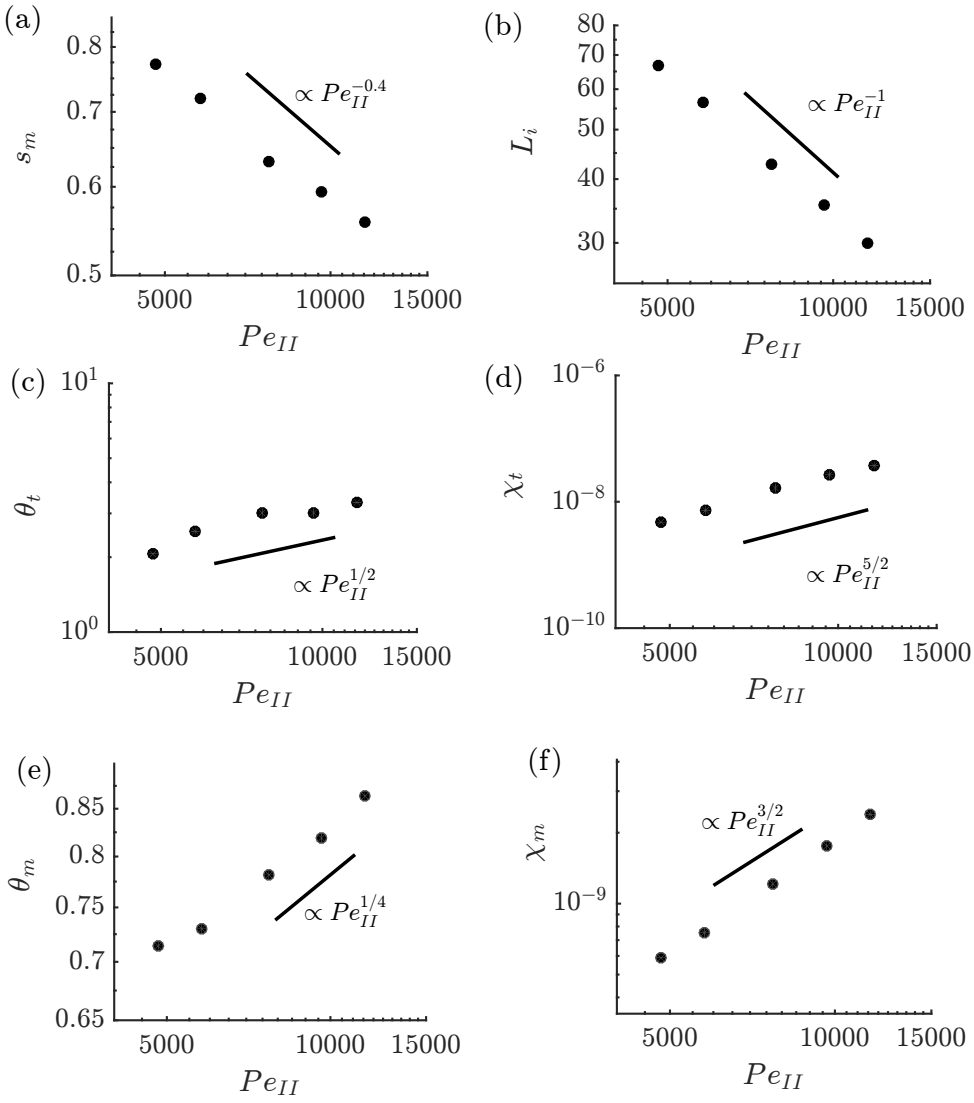

FIGURE 4..2: a) Maximum mixing width, s_m b) interface length, L_i, c) maximum concentration gradient at the toe, θ_t d) maximum scalar dissipation rate at the toe, χ_t e) maximum concentration gradient at s_m, θ_m and f) maximum scalar dissipation rate at s_m, χ_m as a function of Pe_{II}

CHAPTER 5

A new reaction to probe mixing-induced reactions at fluid interfaces

5.1 Introduction

Chemical reactions that occur due to the mixing of different fluids are of great interest when predicting the fate and transport of contaminants. Understanding the processes leading to chemical reactions across fluid interfaces are particularly relevant in many subsurface environmental applications such as aquifer remediation, groundwater management, waste storage and artificial recharge. Reactive mixing, across fluid interfaces can exhibit interesting behaviours depending on the spatial and temporal scales of interest and can be enhanced by spatially non-uniform variations of the flow field triggered by complex boundary conditions, natural heterogeneity or temporal perturbations of the flow (e.g., tides and seasonal recharge).

In order to better understand the processes that lead to reactions, many studies have looked to non-invasive optical measurement techniques (Oates and Harvey, 2006). To evaluate reactive mixing in porous media, notable studies have employed adsorption imaging techniques through the use of colorimetric reactions (Gramling et al., 2002; Oates and Harvey, 2006). In such reactions, two initially colourless reagents react and form a coloured product which can be quantitatively measured in transparent porous media (Oates and Harvey, 2006). In the study by Gramling et al. (2002), a copper sulphate-EDTA reaction is employed which produces a dark blue product. The amount of light absorbance can then be related to the concentration of a particular species through the Beer-Lambert law, which considers the attenuation of light through the tank thickness. The light absorbance values can then be used to determine the concentration of $CuEDTA^{2-}$ using a pre-determined calibration curve (Gramling et al., 2002). A disadvantage of such methods is the non-linear relationship between concentration and the transmitted light. Smaller variations in concentrations results in smaller variations in transmitted light which makes it difficult to resolve small concentration gradients (de Anna, 2013). To overcome this issue, de Anna et al. (2013b) used a peroxyoxalate chemiluminescent reaction (Jonsson and Irgum, 1999) to characterize reactive mixing. Unlike light absorption imaging, this method allows for direct visualisation of local reactions rates. The emitted light detected from this reaction is directly proportional to the amount of reaction taking place at the mixing front (Mendenhall, 1993; Blum, 1997). While this reaction has been previously performed in a Hele-Shaw cell, a similar reaction has yet to be performed in Darcy-scale experiments. While the concept of chemiluminescence is

indeed an attractive method to study reactive mixing in porous media, the particular chemiluminescent reactions employed by de Anna et al. (2013b), has a number of limitations that make it difficult to employ in larger experimental set-ups. To overcome some of this issues, we introduce the use of luminol chemiluminescence as an alternative method to probe reactive mixing across fluid interfaces. The main benefit of this reaction is that it omits the use of highly toxic compounds and uses water as the solvent. This is not only easier to handle in larger experimental set-ups, but can also significantly reduce experimental costs.

The principal objective of this chapter is to demonstrate the applicability of luminol chemiluminescence in studying fast irreversible reaction, $A + B \rightarrow C$. To this end, batch experiments performed with the chemluminescent reaction are presented in this chapter which will serve as the basis for the experiments performed in chapter 6 and 7, where it is then implemented in a millifluidic cell and sand tank, respectively.

5.2 Characterization of Local Reactions across the Interface

The primary goal of the experiment is to develop a chemical reaction to probe mixing at deformed fluid interfaces. In search of an appropriate reaction to achieve this, the following general attributes were sought,

- Reaction kinetics are fast enough to be limited by mixing processes ($Da \gg 1$). In other words, once the reactants are locally mixed, they become chemically depleted in a very short time and the reaction stops.
- Reaction intensity is sufficient to be detected with the sensor at a distance that captures the entire tank.
- The nature of the reaction would not impede variable density flow

To achieve this, we make use of a fast (flash-type) chemiluminescent reaction. In this type of reaction, light is emitted when an intermediate species in an excited state returns to the ground state. The amount of emitted light is directly related to the reaction rate. A similar method was previously used by de Anna et al. (2013b), who studied mixing and reaction kinetics in a Hele-Shaw pore scale study using a peroxyoxalate chemiluminescent reaction described by Jonsson and Irgum (1999). The spatial light distribution resulting from chemiluminescence in a single pixel allows us to measure the derivative in time of the concentration product C. For a given time of measurement, this gives the reaction rate which is quantified as,

$$R_{i,j} = \frac{P_{i,j}}{\tau_{exp}}, \tag{5.1}$$

where $P_{i,j}$, is the pixel value at the coordinate indices (i, j) and τ_{exp} is the exposure time set on the camera.

5.2.1 Luminol Chemiluminescence

Since we aim to employ the chemiluminescent reaction at the sand-tank scale under variable density flow, rather than the peroxyoxalate chemiluminescent reaction used in de Anna et al. (2013b), we consider a luminol chemiluminescent reaction. The main advantages of this reaction compared to the latter are two-fold:

1. We omit the use of highly toxic compounds such as as 1,8-diazabicyclo-[5,40]-undec-7-end (DBU) and aminofluoranthene (3-AFA).

2. The solvent used for the reaction is water as opposed to acetonitrile (density, ρ = 787 kg/m^3 and viscosity, μ = 3.4 x 10^{-4} kg^2/(m·s)). From a practical point of view, access and handling of purified water is significantly easier. In larger sand-tank experiments, where several litres of fluid may be needed in a single experiment this drastically lowers the cost associated to performing a single experiment (100 ml of acetonitrile can cost up to 70 euro). In the context of variable density transport using purified water also allows us to control the density of seawater solution using salt alone.

General mechanism

The chemiluminescent reaction involving luminol (5-amino-2,3-dihydrophtalazine-1,4-dione) proceeds via a number of intermiediate steps. While the mechanism through which luminol is oxidised is still poorly understood (Rose and Waite, 2001; Bustos et al., 2001), studies have isolated the main steps that lead to the resulting chemiluminescence. A detailed summary of these mechanisms are outside the scope of this study, however we summarize below the major pathway leading to luminol chemiluminescence. This has been shown to occur in three basic steps (Merenyi et al., 1990). As depicted in Figure 5.2.1, Luminol is first oxidised to the α-hydroxyperoxide intermediate whose decomposition leads to the excited state and the emission of light.

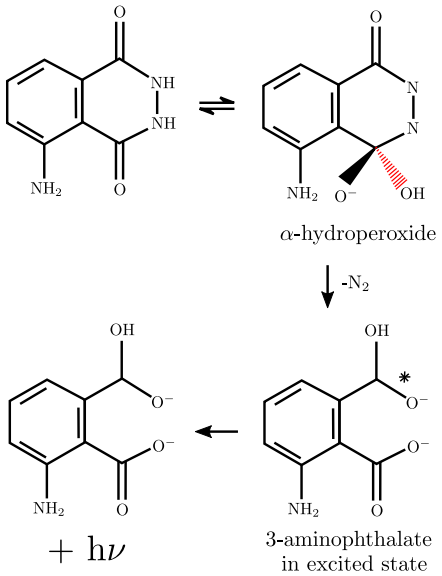

FIGURE 5.2.1: Simplified reaction mechanism for luminol chemiluminescence. Image adapted from Dodeigne et al. (2000)

.

The oxidation of luminol to α-hydroperoxide, requires the primary oxidation of luminol to a luminol radical followed by a secondary oxidation to the intermiediate. The primary oxidation step can be achieved by many different strong oxidants including trace metals such as cobalt, copper, iron, manganese and magnesium (Klopf and Nieman, 1983; Burdo and Seitz, 1975) as well as horseradish peroxidase (Dodeigne et al., 2000). While other mechanisms have been proposed depending on the oxidants used, there is a general consensus that the production of the key intermiediate α-hydroxy hydroperoxide is a precurser for luminol chemiluminescence

(Rose and Waite, 2001). The first step is strongly dependent on the composition of the reacting system, e.g. the concentration of solutes, nature of the oxidant and pH. In this study we also employ cobalt as our primary oxidant, which in combination with hydrogen peroxide has been shown to greatly increase the intensity of chemiluminescence (Klopf and Nieman, 1983; Burdo and Seitz, 1975). Note that hydrogen peroxide itself does not contribute to chemiluminescence, but its decomposition to OH radicals plays a major role in the reaction. According to Burdo and Seitz (1975), the reaction mechanism in the presence of this metal involves the formation of a cobalt-peroxide intermediate complex which reacts with luminol in basic aqueous solution to produce a luminol radical in the rate determining step. The luminol radical then reactions with hydrogen peroxide to produce the light emission. Results from Burdo and Seitz (1975) and Klopf and Nieman (1983) have also indicated the strong sensitivity of this reaction to the luminol and hydrogen peroxide concentration and pH, all of which can lead to non-monotonic changes in the prevailing light emission intensity. For example at low pH increasing concentration of hydronium ion will react with the cobalt-peroxide complex causing its dissociation, however at very high pH, the hydroxide ion will increasingly react with the complex to generate cobalt hydroxide, which is non-light producing (Burdo and Seitz, 1975).

5.2.2 Batch tests

In order to demonstrate the applicability of luminol chemiluminescence to investigate fast mixing-limited reactions we perform batch tests. These tests were carried out to ensure the reaction kinetics were optimized such that light emissions are largest and the reaction was sufficiently fast. We record the emitted light after mixing the reactants within a well-mixed beaker with a magnetic stirrer using a sCMOS camera (Hamamatsu ORCA flash 4.0)(see Figure 7.2.1c). Solution B, is first placed in a beaker with the magnetic stirrer. A small volume of solution A is then quickly added using a syringe while recording the light emission. While this method was not highly controlled, it provided a means to evaluate the reaction kinetics.

Procedure

To carry out this reaction, we prepare two solutions which upon reacting follows, $A + B \rightarrow C$. In solution A we mix luminol with cobalt chloride hexahydrate ($CoCl_2 \cdot 6H_2O$) where the pH has been adjusted to 12 using sodium hydroxide. Solution A is tested with and without salt to determine whether this has any influence over the reaction kinetics. The salt concentration used is 35 g/L which is required for the variable density flow experiment in Chapter 7. We also test the influence of changing the concentration of hydrogen peroxide. After a series of batch tests, the chosen concentrations of reagents used in solution A was 1 x 10^{-3} M luminol, 5 x 10^{-4} M Co(II). The concentration of H_2O_2 in solution B is 1 x 10^{-4} M.

5.3 Results and Discussion

Results from the optimized batch test are presented in Figure 5.3.1. After mixing solutions A and B, the emitted light quickly reaches a maximum. At this point the mixture is homogeneous and then begins to decline as the reactants are depleted.

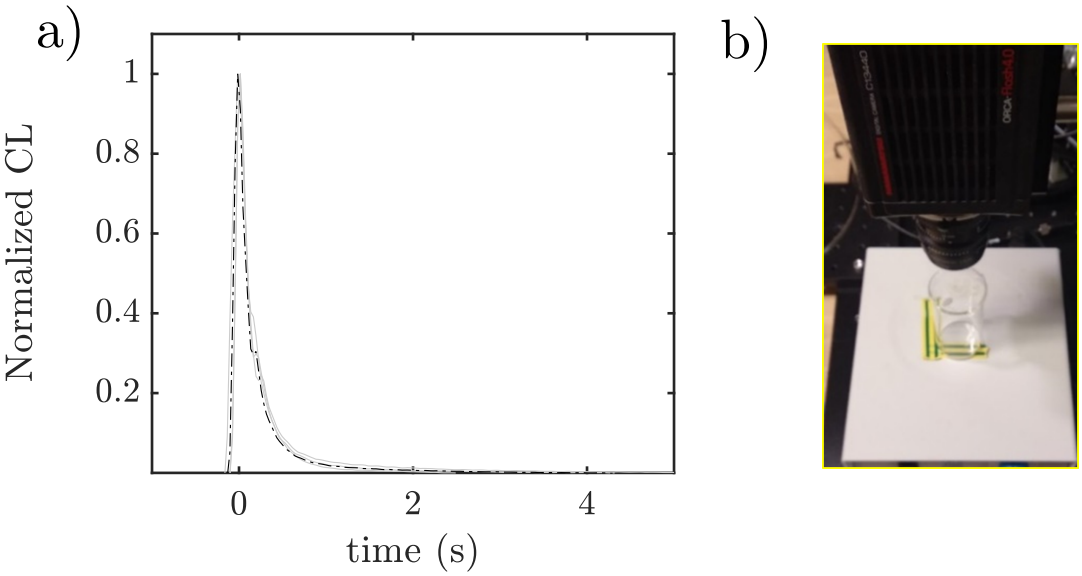

FIGURE 5.3.1: a) Example of a batch test performed with the optimized reagent concentrations using the salt solution. Light grey lines denote four repeated tests and the dashed dark blue line denotes the average. Light emissions have been normalized by the maximum light intensity. b) Image of batch test set-up with a beaker placed upon a magnetic stirrer and the camera fixed above

We compare the results from Figure 5.3.1a to the reaction kinetics observed in the study by de Anna et al. (2013b). This is done by comparing the characteristic reaction time, τ_r, which is the time for the reaction to reduce the emitted light by a factor of 10 in a well-mixed volume (de Anna et al., 2013b). Note that the characteristic reaction time obtained is approximately 0.5 s, which is lower than the one obtained by de Anna et al. (2013b). Thus the Damköler number, defined as the the ratio of advection to reaction time scale (τ_a/τ_r), with $\tau_a = \xi/\bar{v}$ in terms of the pore-length (ξ) and the average velocity ($\bar{v}$), leads to a Da = 300, using the parameters defined in de Anna et al. (2013b) (ξ = 12 mm and $\bar{v}$= 0.08 mm/s).

With obtained characteristic reaction time, we can similarly define a Da for a generic sand tank experiment, where the velocity is controlled by a hydraulic head gradient, ΔH. In this scenario, the characteristic advection time can given by $\tau_a = l_c/v_c$, where l_c is the characteristic length, which could be defined by the transverse dispersivity, α_t and v_c is the characteristic velocity which can be approximated by $K\Delta H/\phi L$, where L is the length of the domain. Using values representative of typical sand tank experiments using 1 mm glass beads (e.g. Abarca and Clement, 2009), ΔH is 9 mm, K = 1e-2 m/s, ϕ = 0.3 and L = 0.5, and α_t = 0.5 mm ,this would give Da $\sim$ 17.5. While this is a magnitude smaller than the the expected values in the Hele-Shaw experiment of de Anna et al. (2013b), we still achieve our goal of having Da $\gg$ 1.

Figure 5.3.2b illustrates the impact of increasing the concentration of hydrogen peroxide by two orders of magnitude. Note that this results in two different decays in light emissions. This is attributed to the complete consumption of Co(II) to Co(III) which then results in the slow oxidation of luminol with the remaining hydrogen peroxide. According to Burdo and Seitz (1975) at low H_2O_2, the intensity of the chemiluminescence emission should be proportional to H_2O_2, however at high peroxide concentration the peroxide-cobalt complex can reactive with peroxide leading

to H_2O and O_2, thus reducing the concentration of the complex and reducing the intensity of chemiluminescence. Since chemiluminescence is strongly sensitive to the concentrations of chemicals used, batch tests using the presented set-up provides a useful method to ensure the reaction is behaving ideally.

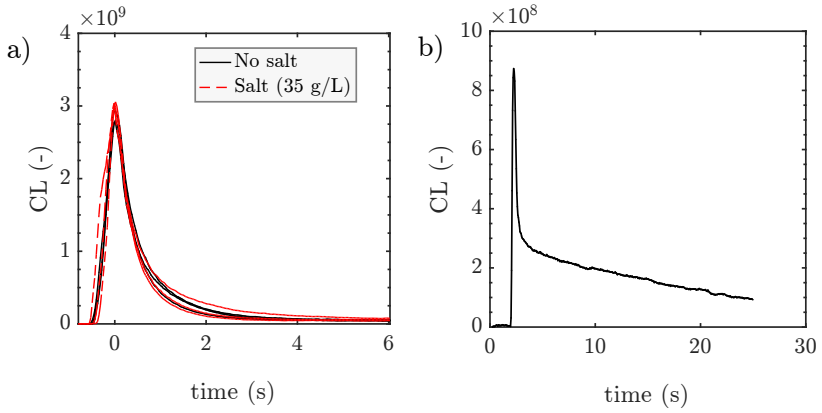

FIGURE 5.3.2: a) Batch tests performed for a solution with and without salt. 3 Repetitions are performed for each solution. b) Batch test performed with hydrogen peroxide concentration of 1e-2 M

.

In Chapter 6 and 7 we employ the chemiluminescent reaction in experiments using both pure water and in a salt solution to induce variable density flow, respectively. Although the addition of salt in luminol chemiluminescence has previously been shown to enhance chemiluminescence (Collaudin and Blum, 1997), our results suggest that the reaction is not significantly altered for the salt concentrations under consideration.

The results from the batch tests demonstrate that luminol chemiluminescence is a viable alternative when attempting to perform fast mixing-limited reaction experiments. While the instruments used for the batch tests may not be the most sensitive method of assessing reaction kinetics, access to a stopped flow device or a continuous stirred reactor may provide a means to constrain reaction kinetics more precisely. These instruments would also allow reactive mixing experiments to be tested over a wide range of Damköhler numbers by tuning the reaction kinetics (e.g. by decreasing the pH of solution A). Ideally, batch tests should be performed using a sample of the reactants before or in unison to the reactive experiment in order to account for variability in the reaction kinetics.

To demonstrate the general application of luminol chemiluminescence in porous medium we inject some saline solution A into a tank filled with hydrogels which is saturated with solution B. Since hydrogels are almost perfectly refractive indexed matched with water (Figure 5.3.3a), reactions can be observed across the entire domain, which allows one to quantify global reaction dynamics in 3D porous media. The importance of refractive index matching is further illustrated in Figure 5.3.3b. Here, we see that reactions occurring at at water-air interface results in significant light scattering where there is no water. This makes it very difficult to identify local reaction dynamics. In the zoomed in snap shot we can clearly see that reactions are enhanced as the mixing interface is deformed and stretched around the grain boundaries (e.g. de Anna et al., 2013b).

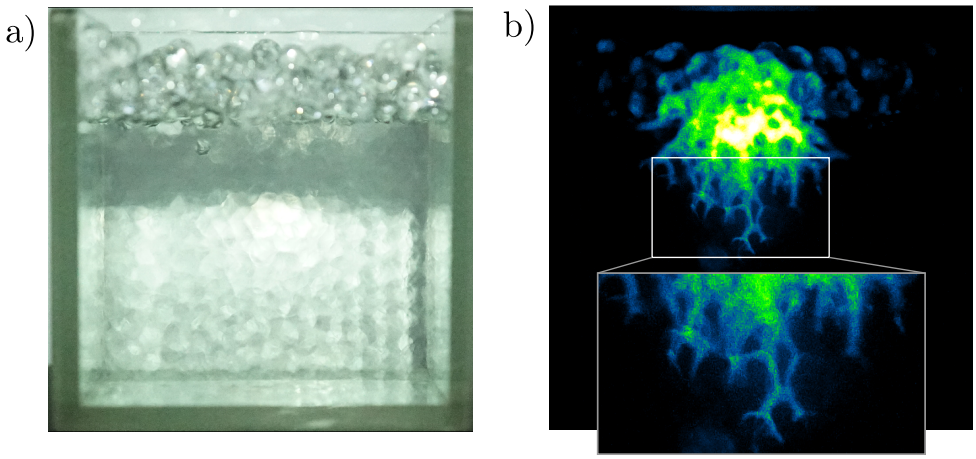

FIGURE 5.3.3: Example of chemiluminescent reaction occurring across mixing interface in hydrogel filled tank. a) The tank filled with hydrogels and b) the ensuing chemical reaction after injection solution A into the tank saturated with solution B.

5.4 Summary and Conclusion

In this chapter we propose the use of luminol chemiluminescence to characterize experimentally mixing-induced reactions across fluid interfaces. Through batch experiments we demonstrate that luminol chemiluminescence shows favourable reaction kinetics that could be used to study reactive mixing in a variety of porous media flow experiments. From a practical point of view, this reaction is much more flexible than using peroxyoxalate chemiluminescence presented in de Anna et al. (2013b), particularly for larger experimental set ups. The use of luminol chemiluminescence also limits the amount of hazardous chemicals required and would likely significantly reduce the costs involved when performing numerous experiments. On the other hand luminol chemiluminescence and chemiluminescent reactions in general, are known to be incredibly sensitive to factors such as pH, temperature, minor changes in reagents concentrations, the presence of oxygen bubbles and also any impurities present in the tank or water. A combination of these factors may result in some variability across multiple experiments, which should be considered.

CHAPTER 6

Reactive mixing across a stagnation point – An experimental investigation in pore scale flows [1]

6.1 Introduction

Understanding mixing processes in porous media is a fundamental precursor to predicting the fate, transport of many reactive solutes. In many natural groundwater systems, mixing-driven reactions can exhibit a wide range of complex behaviours over different spatial and temporal scales. This can manifest in enhanced local reactions, or reaction 'hot spots' in a wide range of environments where mixing between two fluids is of concern, such as between surface and groundwater (McClain et al., 2003) as well as seawater and groundwater. Strong variations in velocity, induced either by geological heterogeneity (Geng et al., 2020), variable density flows (Rezaei et al., 2005) and transient forcings such as tides or seasonal rainfall (Zheng et al., 2016; Dwivedi et al., 2000) have have been associated to enhanced reactions. Stagnation points in particular are known to occur in a number of scales in porous media, including at the pore scale (Lester et al., 2016), seawater intrusion (Held et al., 2005), unstable convective flow (Hidalgo and Dentz, 2018) and in groundwater flows beneath river bed dunes (Hester et al., 2013; Marzadri et al., 2016). They may also appear in response to groundwater management practises where fluids are injected back into the subsurface (Lu et al., 2009a; Wang et al., 2014). This type of critical point flow is thought to be important as it results in exponential elongation of solutes (Ranz, 1979).

The dynamics of reactive mixing have been extensively studied across reaction-diffusion mixing front in the absence of flow. The behaviour of reversible bimolecular reactions, $A + B \rightleftharpoons C$ coupled to diffusion, for example were theoretical derived for initially segregated reactions (Galfi and Racz, 1988; Larralde, Hernan et al., 1992). The scaling laws were also recovered in the experimental work of Park et al. (2001). In one of the few experimental studies looking at mixing-induced reactions under advective transport de Anna et al. (2013b), investigated reactive mixing in a milifluidic cell containing 2D porous media using a fast chemiluminescent reaction, of type $A + B \rightarrow C$. This experiment was also the first to use chemiluminescence to study reaction in porous media, which unlike colorimetric methods (Oates and Harvey, 2006; Gramling et al., 2002), allowed for direction visualisation of reaction rates across the reactive front. They showed that the presence of grains results in strong deformation of the invading front, resulting in the fingering of the invading solute, thereby

[1] This Chapter is the backbone of the paper "Izumoto, Huisman, De Vriendt et. al. - Enhancement of mixing-induced reactions at stagnation points in pore scale flow fields, *in preparation*".

enhancing reaction rate. Employing the lamella theory of mixing (Villermaux, 2012), the authors were also able to directly quantify the role of stretching due to shear on reactive mixing. Coupling the lamella theory to bimolecular irreversible reactions, Bandopadhyay et al. (2017) also derived analytical expressions for effective reaction rates in the presence of shear over a range of Damköler numbers.

In this study, we investigate experimentally mixing and reaction across a stagnation point in porous media. To this end, we assess the influence of different flow rates, represented by the Péclet number, on chemical reaction dynamics. We begin by deriving the theoretical scaling laws at a stagnation point as a function of Pe and Da using the same framework of Bandopadhyay et al. (2017). The experiment is perfomed in a Hele-Shaw cell with and without the presence of cylindrical grains in a flow configuration most commonly known as a Rankine Half-body (Rankine, 1864). This is established by imposing a background flow on one side of the cell and a point source further down stream, which results in a stagnation point between the two. The experiments are performed using both a conservative tracer as well as reactive solutes which induce chemiluminescence. Within the greater scope of this thesis looking at reactive mixing across the salt-freshwater interface, this experiment also helps to validate the use of luminol chemiluminescence developed in Chapter 5 as well as shed light on to the mixing mechanisms at the salt water toe, where a local stagnation point is also known to exist.

6.2 Mixing across a stagnation point: Theory

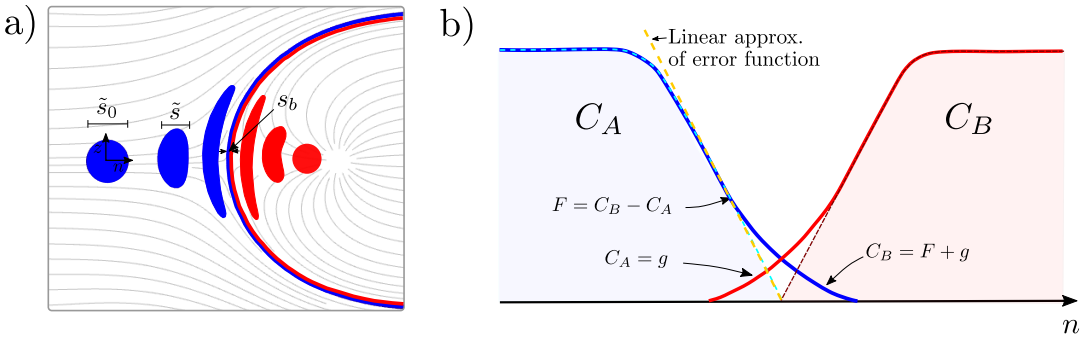

FIGURE 6.2.1: a) Illustration showing a) the deformation of a solute blob towards the stagnation point of the Rankine half-body b) concentration profile of species A (Blue) and B (Red) across the stagnation point. Dotted cyan line denotes the conservative component F and the yellow line represents the linear approximation of error the error function (F).

.

In the following section, we derive approximate analytical solutions for mixing coupled with reaction at stagnation points using a similar methodology to Bandopadhyay et al. (2017). To do so we employ the lamellar theory of mixing (Villermaux, 2012; Le Borgne et al., 2015). As depicted in Figure 6.2.1a, we consider the deformation of material fluid elements which can be stretched and compressed due to given characteristics of the flow field. The compression rate, given by γ is defined as,

$$\gamma = \frac{1}{\tilde{s}} \frac{d\tilde{s}}{dt}, \tag{6.1}$$

where $\tilde{s}$ is the width of the lamella in the principal direction of compression. At stagnation points we have a constant compression rate, resulting in the lamella width to decay exponentially towards it.

$$\tilde{s} = \tilde{s}_0 e^{-\gamma t}. \tag{6.2}$$

Where $\tilde{s}_0$ is the initial lamella size. At sufficiently long times when the mixing time is reached, $t_s \sim \frac{1}{2\gamma}(\gamma s_0^2/D)$, diffusive growth and compression rate reach an equilibrium (Villermaux and Duplat, 2006),

$$\frac{D}{\tilde{s}^2} \sim \gamma. \tag{6.3}$$

The size of the lamella after the mixing time, is known as the Batchelor scale (Batchelor, 1959),

$$s_b = \sqrt{\frac{D}{\gamma}}. \tag{6.4}$$

In laminar flow conditions, the compression rate can be approximated as $\gamma \sim \nabla v \sim \bar{v}/l_c$, where ∇v is the characteristic velocity gradient across the stagnation point, $\bar{v}$ is the average velocity and l_c is the characteristic length over which the velocity gradient occurs. The Batchelor scale can therefore be given as,

$$s_b \sim \sqrt{\frac{D}{\bar{v}/l_c}} \sim \mathrm{Pe}^{-1/2}, \tag{6.5}$$

where Pe defines the Pèclet number, here defined as $\mathrm{Pe} = \bar{v} l_c / D$. This defines the ratio of the diffusion time scale ($\tau_d = l_c/D$) to the advection time scale ($\tau_a = l_c/\bar{v}$). We define our transport problem in the local Lagrangian frame. This frame is attached to a material line orientated along the direction of elongation and compression, perpendicular to the mixing interface. This framework assumes that concentration gradients along the direction of elongation are negligible compared to the direction of compression where mass-transfer dominantly prevails. The compression diffusion reaction equation in the Lagrangian framework is described as,

$$\frac{\partial C_A}{\partial t} + \gamma n \frac{\partial C_A}{\partial n} = D \frac{\partial^2 C_A}{\partial n^2} - R, \tag{6.6}$$

here, C_A and C_B represent reactant concentrations that have been normalized by their initial concentration C_0. R is the reaction rate defined by kC_AC_B, where k is the rate constant, which for dimensionless concentrations, $k = \hat{k}C_0$, where $\hat{k_0}$. γ represents the stretching rate, defined as,

$$\gamma = \frac{1}{s}\frac{ds}{dt}. \tag{6.7}$$

Warped time, θ quantifies the enhancement of diffusion in response to fluid stretching,

$$\theta = \int_0^t d\tau \frac{D}{\tilde{s}(\tau)^2}, \quad \tilde{n} = \frac{n}{\tilde{s}}. \tag{6.8}$$

For exponential compression the warped time is defined as,

$$\theta = \frac{D}{\gamma \tilde{s}_0^2}\frac{1}{2}(e^{2\gamma t} - 1) \tag{6.9}$$

After non-dimensionalizing, equation (6.6) is reduced to a diffusion-reaction equation (Bandopadhyay et al., 2017),

$$\frac{\partial C_A}{\partial \theta} = \frac{\partial^2 C_A}{\partial \tilde{n}^2} - \mathrm{Da} C_A C_B \tilde{s}^2, \tag{6.10}$$

where Da defines the Damköler numbers given as the ratio of the diffusive time scale $\tau_d = s_0^2/D_m$ over the reactive time scale $\tau_r = (c_0 k)^{-1}$.

$$\mathrm{Da} = \frac{k C_0 s_0^2}{D}, \tag{6.11}$$

and $s = \tilde{s}/\tilde{s}_0^2$.

Derivation for $Da > 1$

In this scenario, the interpenetration of reactants is small. Following Larralde et al. (1992) and Bandopadhyay et al. (2017), the concentrations of reactants can be written in terms of the conservative component $F = C_B - C_A$ and a perturbation g, where $C_A = g$ and $C_B = F + g$.

$$\frac{\partial F}{\partial \theta} = \frac{\partial^2 F}{\partial \tilde{n}^2}. \tag{6.12}$$

Which has solution

$$F = erf\left(\frac{z}{\sqrt{4\theta}}\right). \tag{6.13}$$

After inserting $C_A = g$ and $C_B = F + g$ into (6.10), we obtain

$$\frac{\partial g}{\partial \theta} = \frac{\partial^2 g}{\partial \tilde{n}^2} - \mathrm{Da} g \left(\mathrm{erf}\left(\frac{\tilde{n}}{\sqrt{4\theta}}\right) + g\right) s^2. \tag{6.14}$$

We can further simplify by neglecting the nonlinear contribution of g^2, thus linearizing the error function term $\mathrm{erf}(n/\sqrt{4t})$ (Larralde, Hernan et al., 1992) (see Figure 6.2.1b). This yields the approximation,

$$\frac{\partial g}{\partial \theta} \approx \frac{\partial^2 g}{\partial \tilde{n}^2} - \mathrm{Da} g \frac{\tilde{n}}{\sqrt{\pi\theta}} s^2. \tag{6.15}$$

Under stationary conditions and using spatial coordinates, $n = \tilde{s}\tilde{n}$, this becomes

$$\frac{\partial^2 g}{\partial n^2} - \mathrm{Da} g \frac{n}{s_0^3 s \sqrt{\pi\theta}} s^2 = 0. \tag{6.16}$$

Which is an Airy differential equation. After resorting to an Airy function we arrive at the following solution(Larralde, Hernan et al., 1992):

$$g \sim \frac{\tilde{s}_0^{-2} s^{-2/3} \theta^{-1/3}}{\lambda} Ai\left(\frac{\lambda n}{\tilde{s}_0 s^{1/3} \theta^{1/6}}\right), \tag{6.17}$$

where Ai is the Airy function and

$$\lambda = \left(\frac{\mathrm{Da}}{\sqrt{\pi}}\right)^{1/3}. \tag{6.18}$$

The reaction rate, $R(n,\theta)$ can then be attained by inserting (6.17) into the second term of (6.16)

$$R(n,\theta) \approx \frac{\tilde{s}_0^{-4} s^{-2/3}\theta^{-4/3}\theta^{-2/3}\mathsf{Da}}{\lambda^2} Ai\left(\frac{\lambda n}{\tilde{s}_0} s^{1/3}\theta^{1/6}\right)\left(\frac{\lambda n}{\tilde{s}_0 s^{1/3}\theta^{1/6}}\right). \tag{6.19}$$

This can be written as,

$$R(n) = R_{Max} f\left(\frac{n}{s_R}\right), \tag{6.20}$$

where,

$$R_{Max} \sim \frac{\tilde{s}_0^{-4} s^{-4/3}\theta^{-2/3}\mathsf{Da}}{\lambda^2} \qquad s_R \sim \frac{\tilde{s}_0 s^{1/3}\theta^{1/6}}{\lambda}. \tag{6.21}$$

For large times we note that,

$$s = e^{\gamma t} \qquad \theta = \frac{D}{2\gamma\tilde{s}_0^2} e^{2\gamma t}. \tag{6.22}$$

From here, the following scaling laws can be obtained,

$$s_R \sim \mathsf{Da}^{-1/3}\mathsf{Pe}^{-1/6}, \tag{6.23}$$

and

$$R_{Max} \sim \mathsf{Da}^{1/3}\mathsf{Pe}^{2/3}. \tag{6.24}$$

The integral of the reaction rate over the reactive width, R_c can therefore be approximated by,

$$R_c \sim s_R R_{Max} \sim \mathsf{Pe}^{1/2}. \tag{6.25}$$

Derivation for $Da < 1$

In this scenario, diffusion dominates over reaction and the concentration profiles of reacting species, C_A and C_B behave similar to their conservative profiles (e.g. Bandopadhyay et al., 2017). The non-dimensional reaction rate is given by,

$$R = \mathsf{Da} C_A C_B. \tag{6.26}$$

Inserting the approximated diffusive profiles for C_A and C_B into 6.26, leads to the following approximation for the reaction rate,

$$R = \mathsf{Da}\left(1 - erf\left(\frac{\tilde{n}}{\sqrt{4\theta}}\right)^2\right). \tag{6.27}$$

After converting this to dimensional coordinates we have,

$$R = \mathsf{Da}\left(1 - erf\left(\frac{n/s_0 e^{\gamma t}}{\sqrt{4\frac{D}{\gamma\tilde{s}_0^2}\frac{1}{2}(e^{2\gamma t}-1)}}\right)^2\right). \tag{6.28}$$

At long times, we obtain the following approximation,

$$R = \mathrm{Da}\left(1 - erf\left(\frac{n}{\sqrt{2}s_b}\right)^2\right). \tag{6.29}$$

Under this regime, we would therefore expect that $s_R \sim s_b \sim Pe^{1/2}$ and the maximum reaction rate to scale as,

$$R_{Max} \sim \mathrm{Da}, \tag{6.30}$$

and

$$s_R \sim s_b \sim \mathrm{Pe}^{-1/2}. \tag{6.31}$$

6.3 Materials and Methods

6.3.1 Experimental set-up

The conservative and chemiluminescent reactions were carried out in a millifluidic setup where both a flat (Hele-Shaw) and porous surface were used (see Figure 6.3.1a-b)). The surface mold was fabricated using Polydimethylsiloxane (PDMS) (see Izumoto et al. (2021)) for details regarding the soft lithography method). The porous surface consisted of 1 mm high pillars between 0.34 and 0.82 mm in diameter. The resulting porosity of the 2D porous medium was found to be 0.59. The base mold on which the porous media sits has a length of 150 mm, width of 50 mm and height of 10.4 mm (see Figure 6.3.1b). Note that the pore throat (median of 0.36 mm) was carefully chosen such that it was smaller than the height of the cylinders. This aspect ratio ensures the flow is considered 2D and Taylor-Aris dispersion is dominant in the horizontal direction. For the Hele-Shaw experiment, the porous media mold is replaced with a flat PDMS mold with a length, width and height of 150 mm, 50 mm and 10.4 mm respectively. The gap between the top plate and heleshaw mold results in an aperture of 0.6 mm where the fluid can flow through. The cell holding the PDMS mold is composed of transparent poly(methyl methacrylate)(PMMA) with an outer length, width and height of 450 mm, 125 mm and 33 mm respectively. The cell is fixed together with three main plates: a bottom flat plate (height of 10 mm), a middle plate (height of 11 mm) which has the cavity to hold the 2D porous media and the top plate (height of 12 mm) to cover the top. The flow cell consists of two fluid inlet ports, the left-most used to impose the background flow and the second to impose a point-source using a needle with a diameter of 0.8 mm (see Figure 6.3.1a). A single fluid outlet port is situated on the far right to discharge the spent fluid. The resulting flow results in the formations of a Rankine half body.

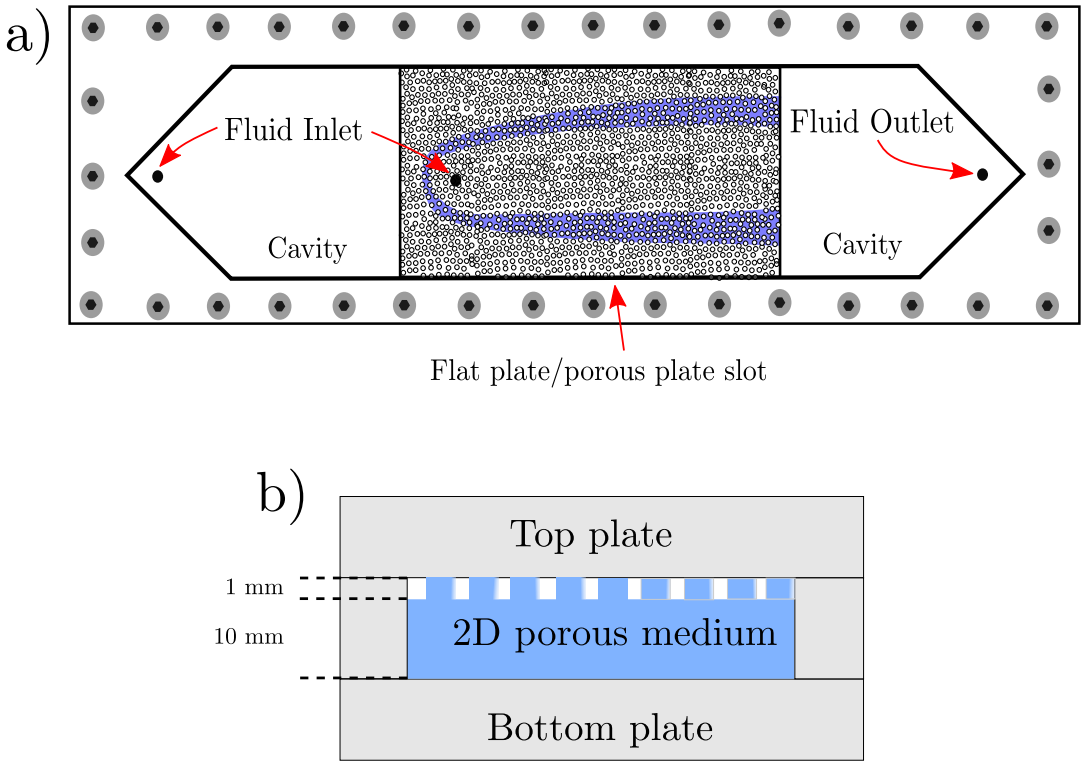

FIGURE 6.3.1: a) Schematic showing the milifluidic flow cell and b) Cross section of the milifluidic cell

6.3.2 Rankine half body

A Rankine half body develops when there is a superposition of flow from a source and a uniform flow (see Figure 6.3.2).

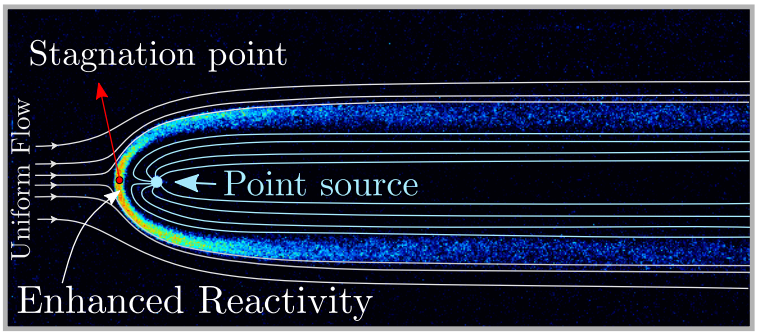

FIGURE 6.3.2: Example of a chemiluminescent reaction image in the Hele-Shaw cell taking place across the mixing interface for a Rankine half-body flow configuration. Lines represent streamlines for the given flow.

The incompressible velocity $\mathbf{q} = (q_x, q_y)$ describing this flow is given by,

$$q_x = \frac{m}{2\pi}\frac{x}{x^2+y^2} + U$$
$$q_y = \frac{m}{2\pi}\frac{y}{x^2+y^2},$$

where m is the strength of the source, $m = Q_i/2\pi r$, where Q_i defines the injection rate, r is the radius of the inlet and U defines the velocity of the uniform background flow. The stagnation point, defined where $q_x = q_y = 0$, is located upstream of the source at position x_s,

$$x_s = \frac{-m}{2\pi U}, \tag{6.32}$$

The compression rate,γ can be given by the symmetric part of the strain tensor (Ottino, 1989)

$$\mathbf{E} = \frac{1}{2}(\nabla \mathbf{q} + \mathbf{q}^T) = \begin{bmatrix} \gamma & 0 \\ 0 & -\gamma \end{bmatrix}. \tag{6.33}$$

Since compression is dominant perpendicular to the interface in the x-direction, we can define the compression rate as the derivative of q_x at $x = x_s$, which is given by,

$$\gamma = \frac{2\pi U^2}{m}. \tag{6.34}$$

6.3.3 Imaging

In both conservative and reactive tests, a digital camera (14-bit, SONY alpha7s) with a macro lens (MACRO GOSS F2.8/90, SONY) was used. The camera was set up above the milifluidic cell at a height of 12 cm for the conservative tests in the porous medium, 28 cm in the conservative Hele-Shaw tests and 13.5 cm in the reactive tests. This provided image resolutions of 0.008, 0.023 and 0.010 mm/pixel respectively.

6.3.4 Characterization of conservative mixing

To characterize the conservative mixing interface, a fluorescein sodium salt tracer was used. This tracer was excited using a blue coloured light source which was placed below the milifluidic cell. Images were captured using a narrow green band-pass filter attached to the camera lens. The images used in this study were captured after the flow and mixing zone stabilized, which was done by visual inspection. The concentration of the fluorescein used was 50 mg/L which was injected from the left as background flow and deionized was injected at the same flow rate through the injection needle in the middle. The flow rates used in the Hele-Shaw experiments were 0.14, 0.28, 0.56, 1.11 and 2.22 mm^3s^{-1} and for the rest of the tests, including the reactions, flow rates of 0.14, 0.20, 0.28, 0.40, 0.56, 0.79, 1.11, 1.57 and 2.22 mm^3s^{-1} were employed. Each flow rate is characterized by the Pèclet number, defined as $\mathrm{Pe} = vl_c/D$, where v is the average pore velocity, l_c is the characteristic length, here given by the median pore throat size of the porous medium and D is the diffusion coefficient (1 x 10^{-9} m^2/s). For our analysis, all conservative images were normalized by the maximum pixel intensity.

6.3.5 Characterization of reactive mixing

In the reactive transport experiments, we use the same chemiluminescent reaction described in Chapter 5 with some minor modifications. Solution A, was composed of the 1 mM Luminol, 7 mM NaOH and 0.01 mM $CoCl_2$. Solution A is injected as background flow through the side injection port and solution B is injected through

the needle as the point source. For each flow rate considered, 5-10 images were taken after the reaction stabilized in order to reduce background noise.

6.4 Results and Discussion

6.4.1 Conservative mixing

The mixing interface width at the stagnation point is determined by fitting an error function to the concentration profiles,

$$C_A = \frac{1}{2}\left(1 + erf\left(\frac{n}{\sqrt{2}s_b}\right)\right). \tag{6.35}$$

The fitted error functions for several Pe are shown in Figure 6.4.1a. The conservative mixing widths from the fitted curves are provided in Figure 6.4.1b). In both the Hele-Shaw and porous medium, we observe the expected scaling described by the Batchelor scale such that $\mathrm{Pe}^{-1/2}$. The mixing width for the porous medium is smaller than for the Hele-Shaw cell, which we attribute to larger compression rates due the the presence of the grains.

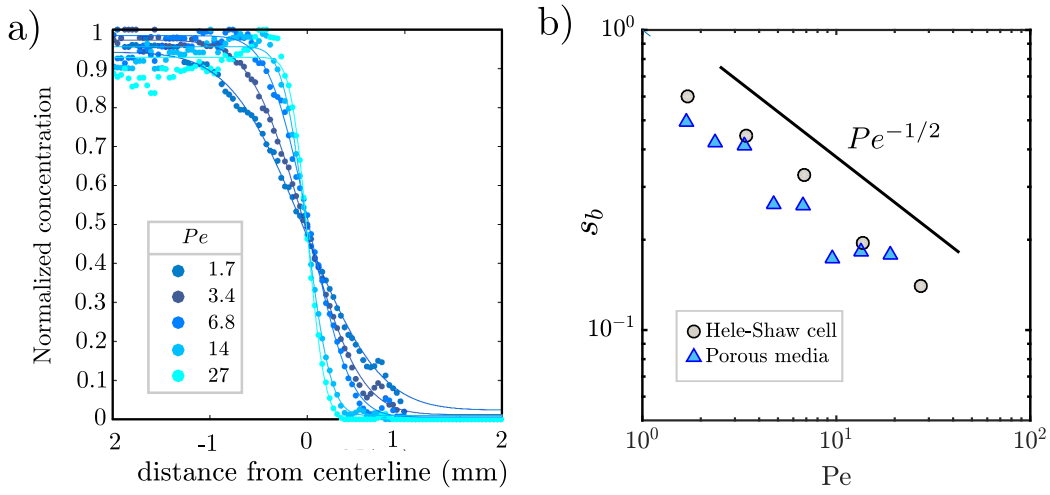

FIGURE 6.4.1: a) Measured concentration profile and the fitted error function curves in the Hele-Shaw configuration and b)Scaling of conservative mixing width as a function of Pe for both the Hele-Shaw and Porous medium experiments.

6.4.2 Reactive mixing

The reaction across the stagnation point in the chemiluminescent tests were evaluated by looking at two separate reaction profiles adjacent to a single grain. In order to reduce noise from these profiles, the Hele-Shaw light intensities were averaged by 30 pixels and for the porous media this was decreased to 1 pixel. The difference here was due to lower light emissions in the Hele-Shaw experiments which resulted in greater noise. To estimate the width and integrated light across the profile, a Gaussian function was fitted to the measured light intensities (See Figure 6.4.2).

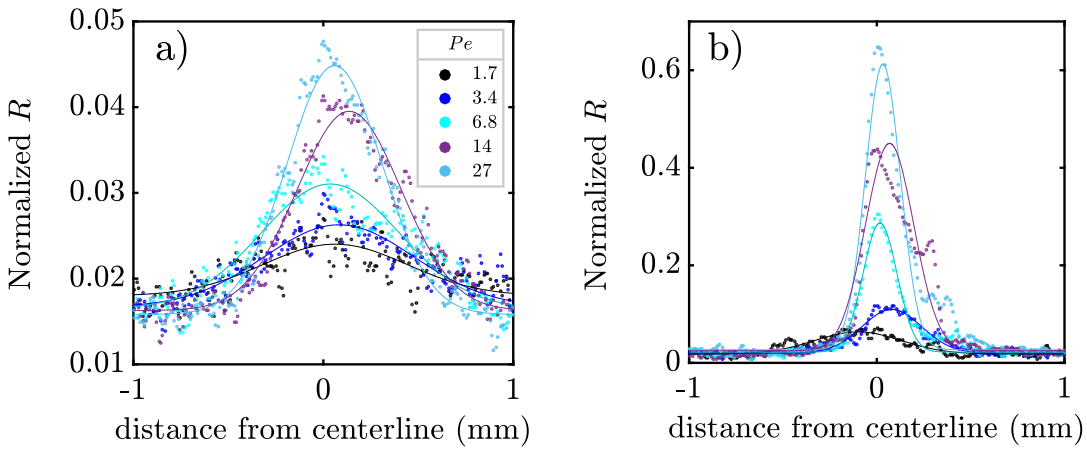

FIGURE 6.4.2: Profiles of the reaction rate across the stagnation points for a) the Hele-Shaw cell and b) the porous medium. Dots denote measured points and lines denote the fitted Guassian curves.

Figure 6.4.3 shows the reactive mixing width, s_R, reaction maximum, R_{Max} and integrated reaction rate, R_c with respect to Pe. Note that for the Hele-Shaw experiments, a very good agreement is obtained with all the theoretical scalings described in section 6.2. For the porous medium, although the agreement with theoretical predictions is also good, some clear deviations are observed, particularly for the S2 profile. This is attributed to strong velocity fluctuations induced by the grains.

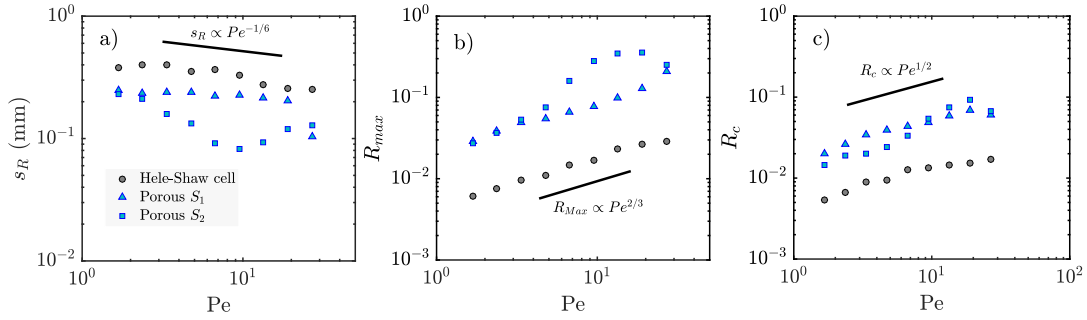

FIGURE 6.4.3: Scalings obtained from the chemiluminescent reaction across the stagnation point as a function of Pe. a) Reactive mixing width, s_R, b) Maximum reaction rate, R_{Max} and c) integrated reaction rate, R_c for both the Hele-Shaw and porous medium experiments.

Differences of the reactive interface in the Hele-Shaw and porous medium experiment can be seen in the example images provided in Figure 6.4.4. While the reactive interface across the stagnation point in the Hele-Shaw cell is smooth and well-defined, in the porous medium the interface is significantly more deformed and the enhanced reactivity appears far more segmented along the stagnation point. We see once again that the reactive width for the porous medium is significantly smaller than the Hele-Shaw cell (Figure 6.4.3a) resulting in much stronger velocity gradients and much larger reaction rates (Figure 6.4.3b).

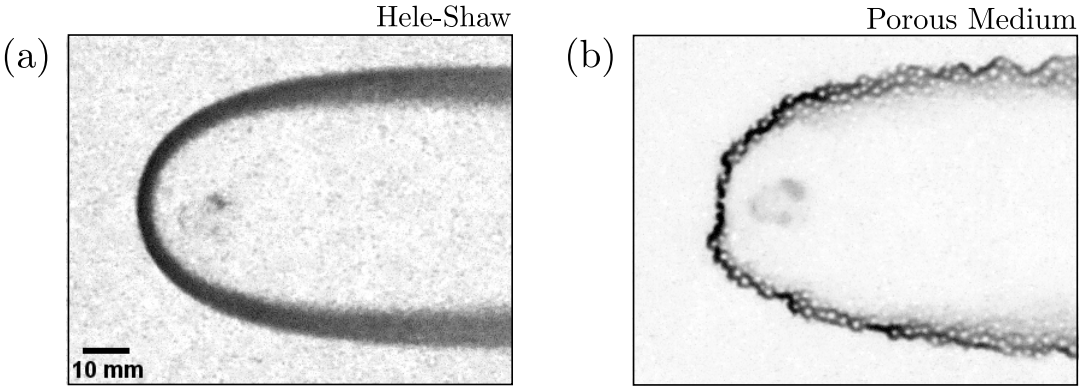

FIGURE 6.4.4: Example images of the reactive interface for the a) Hele-shaw cell and b) the porous medium. Figure c) is an illustration of the experimental flow cell.

Numerical pore-scale simulations carried out by Izumoto (2021) found that compression rates due to the presence of grains strongly enhance compression rates. This is attributed to flow channelling effects which lead to larger velocities at the stagnation point. Such behaviours have commonly been observed in porous media (e.g. de Anna et al., 2013a; Acharya et al., 2007).

6.5 Conclusion

In this chapter we have investigated mixing and reaction across a stagnation point. To this end, we have derived approximate analytical solutions for mixing coupled with reactions at stagnation points and compared this to the results obtained from experiments performed in a milifluidic cell. Analytical scaling laws for this mixing and reaction problem allowed us to predict the conservative mixing width, the reactive width, the maximum reaction rate and the integrated reaction rate as a function of Pe and Da. The results from the experiment showed good agreement with the theoretical predictions, particularly for the Hele-Shaw cell. Results for the porous medium also follow the expected trends, but strong velocity fluctuations due to the presence of grains lead to noise and deviations from the expected scalings. Enhanced compression, which is expected in the porous medium experiments result in smaller conservative and reactive widths and, consequently, much larger reactivity at the stagnation point. This study provides new insight into the reactive mixing dynamics at stagnation points, which appear in many subsurface flow problems. The agreement between experimental results and the theoretical derived reactive behaviour in this well-controlled set-up also validates the applicability of the chemiluminescent reaction as a means to investigate fast bimolecular irreversible reactions in porous media.

CHAPTER 7

Experimental study of reactive mixing across the salt-freshwater interface

7.1 Introduction

Seawater intrusion is a growing concern for both the management of groundwater and the health of coastal ecosystems. Not only does saltwater degrade the quality of fresh water reserves, but submarine groundwater discharge also acts as a major pathway of inland anthropogenic nutrient loadings which can detrimentally impact marine ecosystems (Slomp and Cappellen, 2004; Moore, 2010). Understanding the fundamental mechanisms controlling mixing and the transformation of reactive chemicals would therefore greatly benefit our ability to predict and manage coastal groundwater systems. As demonstrated by Rezaei et al. (2005) and Sanford and Konikow (1989), the mixing of waters with different chemical compositions has been shown to lead to dissolution hotspots at the toe and head of the interface. The influence of fast mixing-limited reactions is therefore crucial to understanding the evolution of coastal carbonate landscapes over large time scales. However, as of yet, there have been no experimental investigations into role of non-uniform flow on mixing and reactions across the salt-freshwater interface.

Over the past decade, many studies have turned to using experimental sand tanks to investigate salt-water intrusion (Zhang et al., 2002; Cartwright et al., 2003; Goswami and Clement, 2007; Tamio Takasu, Keisure Maekawa, 2008; Luyun Jr et al., 2009b; Chang and Clement, 2013; Badaruddin et al., 2015; Luyun Jr et al., 2009b; Oz et al., 2015). These experiments have studied a range of processes including; the influence of engineered structures (Luyun Jr et al., 2009b; Abdoulhalik, 2017; Houben et al., 2018), seasonal recharge (Chang and Clement, 2012b), artificial recharge (Luyun Jr et al., 2009a), heterogeneity (Castro-alcalá, 2019; Lu et al., 2013), tides (Kuan et al., 2012), as well as solute transport occuring within and toward the saltwater wedge (Chang and Clement, 2013; Liu et al., 2014; Oz et al., 2015; Singh et al., 2006). The majority of these studies have made use of coloured dyes to observe the movement of the salt-water body and the propagation of the interface, however only a few studies have attempted to quantitatively measure the extent SFI. Abarca and Clement (2009) developed a unique method of delineating the mixing zone using a colorimetric method through the use of pH indicators. Their method allowed for the determination of dispersivity coefficients which showed excellent visual agreement to numerical models. Work by Robinson et al. (2015) highlighted the use of pixel-wise regression using food colouring to delineate the mixing zone. This method was able to accurately quantify the extent of the mixing zone across the SFI for

both steady state and transient experiments. The same method was also used by Robinson et al. (2015) to shed light on the influence of different sized beads on mixing. More recently, machine learning techniques performed by Etsias et al. (2020) in both homogeneous and heterogeneous porous media was shown to outperform the pixel-wise regression technique by minimizing experimental errors introduced by small movements of the camera and air bubbles trapped in the porous medium. Outside the investigation of seawater intrusion, many other techniques have been proposed to optimize the concentration estimates (e.g. Schincariol et al., 1993; McNeil et al., 2006; Rahman et al., 2005; Konz et al., 2008). While many of these studies have shown great success in delineating the concentration field, none of them were designed to adequately estimate mixing which requires well resolved concentration gradients. This task is particularly difficult due to geometric properties of the porous media, trapping of air, non-uniform light sources and light fluctuations, all of which contribute to noisy concentration estimates. Despite these issues, advanced image processing techniques such the kernel regression methods used by Castro-Alcalá et al. (2012), have shown great promise in visualising local mixing in heterogeneous porous media. Knowledge of mixing processes is a fundamental precursor into understanding and predicting the behaviour of a wide range of biogeochemical processes. Unlike solute spreading, mixing captures the main processes that govern mass-transfer mechanisms, or in other words, the rate at which solutes come into contact and homogenize (Engdahl et al., 2013). De Simoni (2005), previously showed that local reactive quantities is controlled by both chemistry and the rate at which chemicals mix. Consequently, non-uniform flow patterns, be it due to heterogeneity or complex boundary conditions, are of particular interest, as they have been shown to directly impact mixing mechanisms (Castro-Alcalá et al., 2012; Engdahl et al., 2014; Le Borgne et al., 2014; Bandopadhyay et al., 2018; Hidalgo and Dentz, 2018). Despite growing interest in mixing and biogeochemical processes in coastal aquifers and a plethora of experimental studies involving seawater intrusion, reactive mixing has yet to be investigated experimentally.

Coastal aquifers are subject to a number of hydraulic stresses that can influence the movement of the salt freshwater interface. These stresses can be both natural and anthropogenic in origin. One of the most pressing issues is sea-level rise associated to global climate change. Estimates suggest a temperature increase of 2 degrees can result in sea level rise of up to 0.4 m (Jevrejeva et al., 2016). Studies have indicated that an increase in sea level can result in significant movement of the saltwater wedge inland (Werner and Simmons, 2009). Salt water intrusion can also be triggered by excessive groundwater abstraction in coastal aquifers (e.g. Rangel-Medina et al., 2004; Steinich et al., 1998), seasonal oscillations due to changes in recharge (Michael et al., 2005) and tidal oscillations. As demonstrated in Chapter 4, the movement of the saltwater wedge can influence mixing dynamics along the salt-freshwater interface. Understanding these dynamics can improve our understanding of fast mixing-dependent reactions ranging from calcite dissolution that occurs over large time scales in response to changing sea levels (Pool et al., 2019b) or the precipitation of iron oxides that help attenuate contaminants in beach environments (Charette and Sholkovitz, 2002). Until now, reactive transport studies have predominantly focused on the intertidal area, where an upper saline plume can develop due to tidal action (Geng et al., 2020; Heiss et al., 2017; Anwar et al., 2014; Robinson et al., 2009; Kim et al., 2017). Furthermore only a limited number experiments studying seawater intrusion have evaluated the influence of flow on mixing for steady state mixing interfaces. Experiments by Abdoulhalik and Ahmed (2018) for example, investigated the change in the size of the mixing zone during an advance and retreat.

They found that when the saltwater wedge intrudes inland, there is no significant increase in the mixing width, however the retreat of the wedge leads to a significant widening of the mixing zone before approaching the new steady state position. While such experiments do highlight some interesting behaviours, they do not provide any insight regarding the presence of high mixing rates or mixing-enhanced reactions.

The objective of this study is to quantitatively assess the influence of non-uniform flow on reactive mixing in response to salt-freshwater mixing using the reaction proposed in Chapter 5. This chapter begins with a discussion of the materials and methods used to carry out the experiment. Here, we introduce the sand tank and the porous media used for the study. Next, we present the method used to characterize and image conservative transport and outline how the chemiluminescent reaction is implemented into the sand tank. Finally, we describe the methods used for imaging and post-processing the steady state and transient images as well the colour channels used to quantify reaction dynamics. The results and discussion is split into two sections; one for the steady state results, where we analyse the behaviour of local reaction hotspots with respect to Pe, and the second is a discussion on some transient responses captured during the movement of the wedge between steady state images.

7.2 Materials and Methods

7.2.1 Sand-tank

Experiments were conducted in a rectangular tank in order to simulate seawater intrusion at laboratory scale. The tank consists of three main compartments, the central porous chamber and the reservoir chambers on either end. The entire tank was made from 10 mm thick glass panels in order to optimize optical clarity while the top and bottom were fabricated using acrylic glass (PMMA). The central porous chamber has dimensions of 0.38 m x 0.15 m x 0.025 m, bound by two screens with a 1 mm nylon mesh which define the boundary to the reservoir chambers. A detailed schematic of the experimental sand tank can be found in Appendix Figure 7.B.1. The inlet of both reservoirs are located at the bottom of the chamber. An outlet is also present along the outer right wall of the salt water chamber where spent fluid can freely discharge (Figure 7.2.1a).

7.2.2 Flow Regulation

Flow across the domain (left to right) is regulated by imposing a hydraulic head gradient across the domain. The hydraulic head on the seaside boundary is maintained by allowing water to freely flow out the upper right outlet. All hazardous waste is then collected in a waste vessel and safely disposed of accordingly. The freshwater head can be varied by regulating the flow entering the bottom of the left reservoir chamber using a variable area flow meter (VAF) (see Figure 7.2.1b). The same system is used to feed the saltwater chamber, however this is left at a constant inflow rate the entire duration of the experiment. The VAF is attached to pressurized vessels controlled by a pressure controller. The freshwater head levels are then controlled by adjusting the VAF located behind the tank to pre-determined flow rates corresponding to head gradients of interest. Due to the nature of the set up, the flow rates are regulated manually during the course of the experiment. The main limitation here

lies in the strong sensitivity of the saltwater wedge to small changes in hydraulic head, which in this set-up cannot be controlled with a high degree of precision. As a result, for the same measured freshwater head, there is often slight changes to the final steady state wedge position across several experiments.

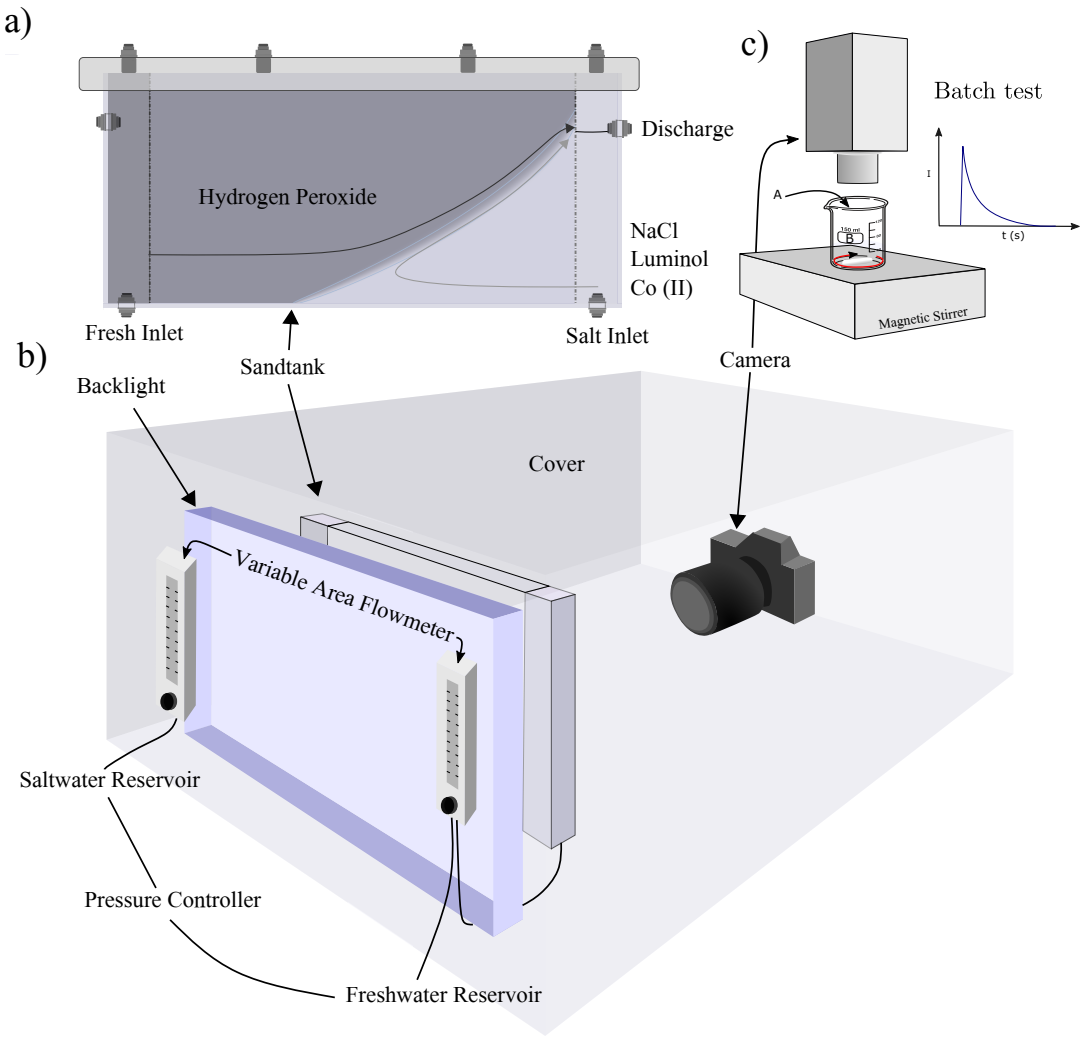

FIGURE 7.2.1: Schematic of experimental set-up and its components. a) Front view of sand tank, outlining the chemical constituents during a reactive experiment. b) Back angle of set-up showing the placement of Variable area flow meter, pressure controller and placement of camera. c) Batch test done using CCD camera upon mixing of reagents prior to the experiment.

7.2.3 Porous Media

In order to best resolve the reaction occurring across the SFI, the goal was to find a material that had the best combination of preferable attributes. Some of the main considerations taken into consideration include:

1. Will the porous media be compatible with the fluids used in the experiment (e.g., Salinity and pH), such that it will not impede the desired reaction or variable density flow?.

2. Is the porous media sufficiently transparent and can it be index-matched to the fluid?.

3. Is the material chosen sufficiently representative of porous media?.

4. Cost and availability/accessibility.

In the following we summarize some of the porous media that were initially considered for use in the experimental set up and their given limitations.

The considered porous media included borosilicate beads, Nafion, hydrogels, fluorinated ethylene propeylene (FEP), fused quartz and cryolite. Borosilicate beads had the benefit of being readily available from a number of suppliers and was optimal due to their uniform shape and sizes. The immediate drawback is that borosilicate beads are not readily refractive index matched with water or salt water. Instead it is typically index-matched with sodium Iodide at 60-64 wt% (Bai and Katz, 2014; Hassan and Dominguez-Ontiveros, 2008). In addition to difficulties regulating the density difference and viscosities, it was found that the sodium iodide solution was readily oxidised, resulting in a yellow hue. This is particularly problematic since a strong oxidant was a precurser to the chemiluminescent reaction. Borosilicate beads have also been used to image mixing patterns in porous media using a glycerol-water fluid mixture (Heyman et al., 2020). However again, the density and visocity differences would not permit studying seawater intrusion for the density differences required while also maintaining optical index matching. Porous media that could be readily index matched to water were therefore found to be the best option. While Nafion beads fitted this description, its limitation lied in its cost as well as its composition. In this case, due to its sulfonic acid backbone, under basic conditions the material would break down. The chemiluminescent reaction under consideration, however requires that the solution is strongly basic. An effort was made to acquire cryolite as it had proven success in the study by Gramling et al., 2002. Unfortunately this mineral is quite rare (Naftaly et al., 2015) and could not be acquired through standard commercial routes. Instead synthetic cryolite was purchased as an alternative, however this source proved to be completely opaque in water and could not be used in any practical manner. Crushed hydrogels were also tested. While this material has optically favourable qualities, its limitations were tied to its very low permeability and also its strong capacity to variably expand. Its final size is very sensitive to salinity (Horkay et al., 2000) of the resident fluid which would be problematic due to the high salinity solutions used to induce variable density flow. In addition, for steady state experiments, reactants would readily be diffused into these gels which would further complicate our analysis of local reactions. Based on the vast complications inherent to the aforementioned porous media and limitations on time and resources, fluorinated ethylene propylene grains (FEP) was found to be the most pragmatic option.

FEP grains showed no clear negative interaction with the fluid and reagents of interest. It was also an attractive option due to its refractive index of 1.338 (Wright et al., 2017) which under the salt concentration of interest was deemed optimal. In reality, achieving perfect refractive index matching in this set-up is not feasible due to density and viscosity differences between the the mixing fluids. Since the chemiluminescent reaction emits light, the main goal is to at least minimise light scattering as much as possible. Unfortunately, the quality of the manufactured material was such that the grains were disappointingly opaque. In Figure 7.2.2a, it is apparent that the grains are poorly translucent. After approximately 3 grains deep, objects behind are no longer resolvable.

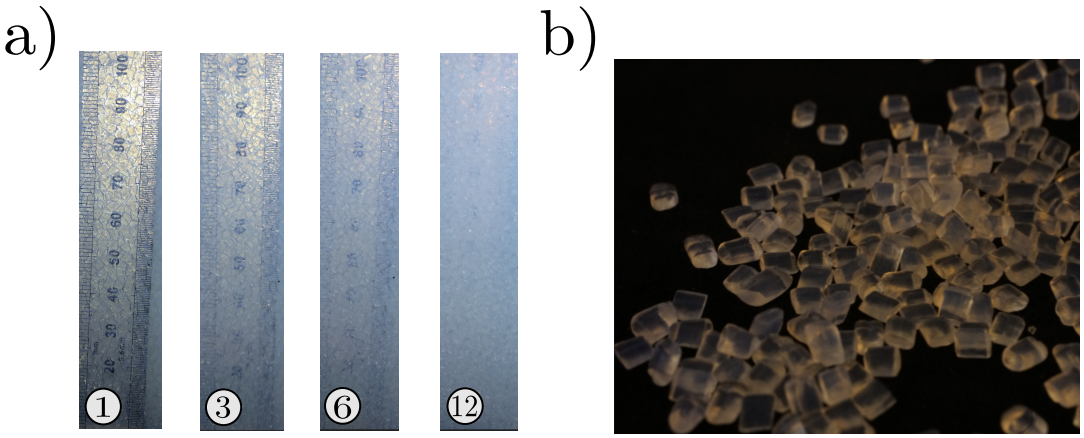

FIGURE 7.2.2: a) Transparency of FEP grains. Numbers denote approximate number of grains in front of submerged metallic ruler b) Close up of individual FEP grains

.

Another limitation to these grains lies in their size and geometry. The procured FEP grains were flat and rectangular, having an average diameters of 2-3 millimetres and a thickness of 1 mm (Figure 7.2.2b). This may result in unrealistic pore space geometries and high porosities not representative of typical porous media. Given the composition of FEP, the grains were also hydrophobic which required additional steps outlined in the following.

7.2.3.1 Packing and saturation

Due to the given shape of the FEP, the grains were added to the central chamber in such a way as to avoid any preferential orientation of the media. Packing and downward pressure was therefore limited during this process. Since the FEP grains are hydrophobic, the tank is flushed with CO_2 prior to and while filling the tank with Millipore water. After the tank is filled, the flow cell is flushed once more with several pore volumes of water purified and de-ionized using the Millipore purification system, henceforth referred to as Milli-Q water. This ensures the water is back at neutral pH.

7.2.3.2 Characterization of hydraulic and transport properties of porous media

The hydraulic and transport parameters were determined in-situ. The hydraulic conductivity, K was determined by measuring the flux change in response to a change in the hydraulic head gradient, ΔH (see appendix Figure 7.B.2). Using this method, we determined a hydraulic conductivity of approximately 2 x 10^{-2} m/s. Due to the hydrophobicity of the FEP, the porosity could not be estimated gravimetrically. Instead, we injected 5 ml of a conservative tracer (food-dye) using 5 syringes orientated along the width of the tank (see Appendix Figure 7.B.3c). The first spatial moment was then measured from images of the solute moving across the tank at different times which was used to deduce to average fluid velocity, v. The porosity could therefore be obtained as, $\phi = v/q_f$, where q_f is the Darcy velocity. We determined a porosity of approximately 0.47. Finally we approximated the longitudinal and transverse dispersivity, α_l and α_t using the same tracer injected determine the

porosity. This was done numerically by performing a parametric study over a range of dispersivity values. The numeric model simulates the same flow and transport problem performed experimentally where we use the previously calculated porosity and hydraulic conductivity values as known input parameters. The dispersivity values that best fit the longitdinal and transverse concentration profiles (see Appendix Figure 7.B.3a-b)) were α_l = 2.5 x 10^{-3} m and α_t = 4 x 10^{-4} m. Note that compared to typical saltwater intrusion experiments done in sand tanks using smaller glass beads ($\sim$ 1 mm) (e.g. Abarca and Clement, 2009; Robinson et al., 2015), these values determined for the FEP are up to one order of magnitude larger.

7.2.4 Characterization of Conservative Transport

We perform a single conservative seawater intrusion tracer test under steady state flow conditions to assess the concentration gradients that prevail. The saltwater wedge was imaged using a light transmission technique. In order to produce a uniform light distribution across the domain, a 100W LED backlight (Effiflux) was placed directly behind the sand tank. Following many previous studies, a non-sorbing food dye was used as the tracer. Image aquisition was carried out using a mirrorless digital camera (14-bit, SONY Alpha 7s). The camera was placed 54 cm away from the tank in order to capture the entire central porous chamber. Under this configuration the size of a pixel corresponds to 0.09 mm. To relate the light intensity to the concentration of the salt-dye solution, calibration images are required. To this end images are taken after flushing the tank with 8 different concentration of dyed salt water (c_1 = 100 %, c_2 = 50%, c_3 =25%, c_4 =12.5%, c_5 =5%, c_6 =2.5%, c_7 =1.25% and c_8 =0.5 %). For each dye concentration, approximately 4 pore volumes were injected starting from the lowest concentration. To relate the pixel light intensity to the concentration, we follow the lead of Robinson et al., 2015. We therefore use a pixel-wise regression method where we determine the power law regression coefficients for every pixel in the image. The concentration, C is therefore related to light intensity, I following,

$$C = aI^b - c, \tag{7.1}$$

where a, b and c are coefficients determined from the regression analysis. This method accounts for spatial variations in lighting due to bead heterogeneities and non-uniform light Robinson et al., 2015. Note that the calibration is specific to the domain being tested. Accordingly, the conservative seawater intrusion experiment was performed directly after the calibration was finished. Prior to doing so, approximately 8 pore volumes of Milli-Q water was flushed across the domain to ensure all the dye was removed from the tank.

7.2.5 Implementation of reaction into Sand tank

In order to implement the reaction into the sand tank, solution A and B are prepared on the same day as the experiment. Due to the poor solubility of luminol, solution A is prepared several hours in advance to sufficiently mix and left in a dark area to limit any possibility of photo-oxidation (Rose and Waite, 2001). Once the sand tank is filled up with Mili-Q water and flushed several times to bring the water back to neutral pH, approximately 3 pore volumes of solution B is injected through the tank from the fresh inlet and subsequently discharged from the saltwater reservoir outlet. Prior to beginning the experiment, four bottles of solution B (6 L) and 2 bottles of solution A (3 L) are connected to the pressure controller and the VAF which feeds into

the bottom of the tank (see Figure 7.2.1b). Since luminol chemiluminescence is notoriously sensitive to low concentrations of various organic and inorganic compounds (e.g. Zhao et al., 2007; Rose and Waite, 2001; Sakamoto-Arnold and Johnson, 1987; Klopf and Nieman, 1983; Kim et al., 2013), the tank and grains are carefully cleaned using Milli-Q water after each repetition.

For each imposed freshwater head, the system is allowed to evolve until steady state is achieved. This was done rather coarsely by inspecting images until at least three consecutive images showed no distinct changes in the distribution of light and the position of the toe. While this incurs some uncertainty, due to the amount of chemicals and fluids required to run several steady state positions, longer times were not feasible. As the freshwater head is lowered, the time required to reach steady state becomes progressively longer due to lower velocities. Sand tank experiments using glass beads typically requires upto one hour or more to reach one steady state interface (Goswami and Clement, 2007; Abarca and Clement, 2009; Robinson et al., 2016). Using the FEP grains, this is drastically shortened ranging between 15 to 25 minutes. An entire experiment for five different steady state configurations can therefore range between 1-1.5 hours in total. The benefit of this lies in minimizing the time the reagents are left in the supply bottles. Solution pH, which is a sensitive parameter to the light intensity was shown not to vary over the course of a single measurement and therefore pH buffers were not needed. In addition, we found that after several steady state measurements, increasing the freshwater head and allowing the wedge to recede did not result in any clear reduction in light intensity. With this in mind it appears that over the course of a single experiment, the solution chemistry may not drastically effect the measured light intensity.

In this study we use the same reaction outlined in Chapter 5 to investigate reactive mixing across the salt-freshwater interface. However, since we need to induce variable density flow, solution A (luminol, Cobalt chloride and NaOH), is mixed with 35 g/L of NaCl. In order to shift the wedge inward, we decrease the freshwater hydraulic head. In this study we present four different experiment repetitions labelled A-D. Experiment A is solely used to qualitatively demonstrate a transient phenomena, however experiments B, C and D are used to evaluate the steady state interface reactions. In experiment B we consider 5 steady state scenarios characterized by 5 different freshwater heads. In experiment C and D we consider 3 steady state scenarios corresponding to 3 different freshwater heads. The imposed hydraulic gradients are summarized in the table 7.1 below.

TABLE 7.1: Hydraulic head gradients imposed for each steady state experiment

	Exp B.	Exp C.	Exp D.
ΔH_1	11.5	8.5	10.5
ΔH_2	10.5	7	9
ΔH_3	9	5	7.5
ΔH_4	7.5	-	-
ΔH_5	6	-	-

Each steady state configuration is described by the Peclet number, here given by $\mathrm{Pe} = K\Delta H/\phi D$. where K (2 x 10^{-2} m/s) is the hydraulic conductivity, ΔH is

the head gradient, ϕ (0.47) is the porosity and D (1 x 10^{-9} m^2/s) is the molecular diffusion coefficient. For the parameters under consideration Pe $\gg$ 1. For each experiment we begin at the highest freshwater head and progressively lower it. Images are continuously taken during the experiment with an exposure time, τ_{exp} of 10 seconds. Steady state is determined by accessing images during the experiment and waiting until there are no longer clear changes in the light distribution and the toe is no longer moving. A minimum of three images of the steady state configuration is taken before lowering the head again. These images are averaged in order to minimize any noise present during the acquisition. We reduce noise further using a 5 pixel ($\sim$ 0.5 mm) mean filter. This is approximately the size between pore spaces where the reactions occur (see Figure 7.2.5). As described in Chapter 5, we use the green channel for our analysis. All image intensities are normalized by the camera bit depth (2^{14}-1).

Figure 7.2.3 shows the general characteristics of the reaction interface at steady state. Note that a blue light is clearly observed along the interface. A feature to point out is the bulbous source of blue light emerging next to the top of the salt water reservoir. This is originating from the strong reaction occurring at the top of the discharge zone where fresh and mixed hydrogen peroxide flows across the top of the salt water reservoir. The light from the reaction is then scattered back into the main tank.

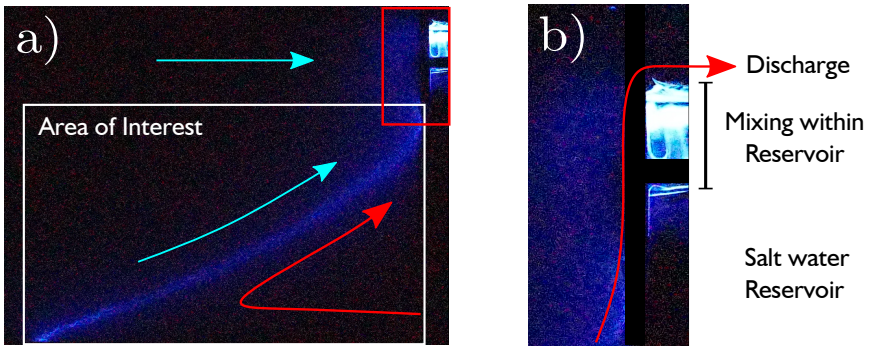

FIGURE 7.2.3: a) Raw image of chemiluminescent reaction across the mixing zone. Arrows depict general flow pattern within the flow cell at steady state. b) zoomed in image of salt water reservoir near discharge zone

.

While this is unavoidable, it does not significantly perturb the light distribution occurring across the main interface. Figure 7.2.4 shows images of the reaction along the interface as it intrudes inward at the beginning of the experiment. Note that it is only once the interface moves far enough inward and up along salt water reservoir that this secondary light from the top becomes visible. Notice also that there is no evident reactions occurring along the screen between the top of the SFI and the outlet. It is likely that mixing across this boundary is limited due to high fluid velocities upwards, which limits the time available for the reaction to occur. Naturally, this works in the favour of the experiment as it limits additional light being scattered across the experimental domain.

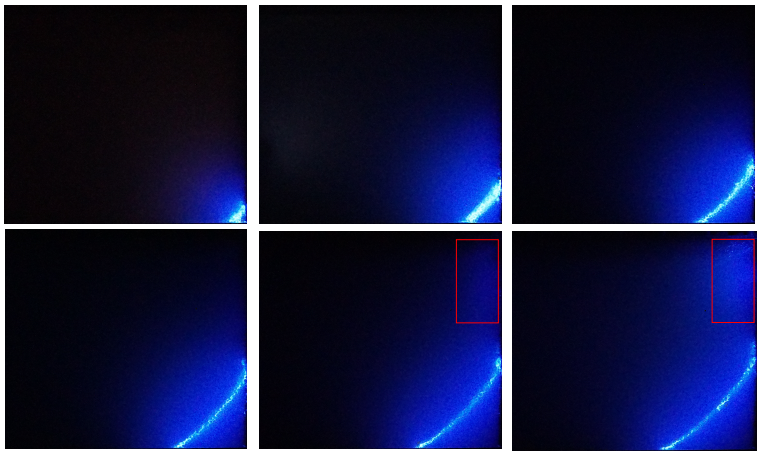

FIGURE 7.2.4: Raw images of Interface reaction during initial injection of solution A prior to arriving at steady state.

7.2.6 Imaging

Image acquisition was carried out using the same camera as for the conservative experiments. Based on the reaction kinetics and camera sensitivity, we choose an exposure time τ_{exp} of 10 seconds. Since images are acquired during steady state we do not need to consider an exposure time based on a characteristic time scale (de Anna et al., 2013b). An ISO of 32000 was found to be an optimal compromise between light sensitivity and the appearance of 'hot pixels' that are magnified by using a high ISO and long exposure times. The aperture is determined prior to filling the tank by focusing on a ruler placed at half the depth of the tank.

7.2.6.1 Steady state images

For each steady state interface, three or more images (over the duration of 3 exposure times) are captured to be averaged as a means to reduce any noise. The local pixel intensities evaluated after filtering can therefore be expressed as,

$$R_{i,j} = \frac{1}{N} \sum_{k=1}^{N} \frac{P_{i,j}^{k}}{\tau_{exp}} \tag{7.2}$$

where N is the number of steady state images for the given ΔH under consideration.

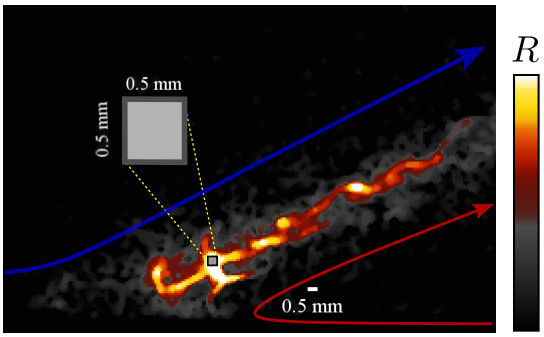

FIGURE 7.2.5: Zoomed in image at the toe of a steady state wedge from experiment D. Square block depicts the size over which the mean filtering was applied

.

7.2.6.2 Transient images

During the movement of the SFI between steady state position images are continuously taken. For experiment B in particular, we evaluate the behaviour of the reactive interface during the interface advance and retreat. Note that an advance refers to the forward movement of the SFI due to a drop in the freshwater head and a retreat refers to the movement of the SFI towards the salt water boundary after increasing the freshwater head. Unlike the steady state images which are in a fixed position, transient images are taken during the movement of the wedge, using the same exposure time (10 seconds). The results from these experiments should therefore be interpreted with caution since images represent the integrated light intensities recorded over the exposure time.

Figure 7.2.6 illustrates the measured toe length over the course of experiment B. It is found that after a drop in the freshwater head, the toe length initially changes quite rapidly then slows down considerably as it approaches the next steady-state position. During a retreat, the toe recedes considerably faster after an increase in head which is in line with previous studies (Robinson et al., 2016). It is likely that during the initial stages of the advance and during a retreat, the reactive interface may appear slightly "smeared". In other words, the reactive width may be larger then what would be expected by using a significantly smaller exposure time. With this in mind, the mixing width, unlike the reaction maximum may not be a reliable metric when evaluating the transient data.

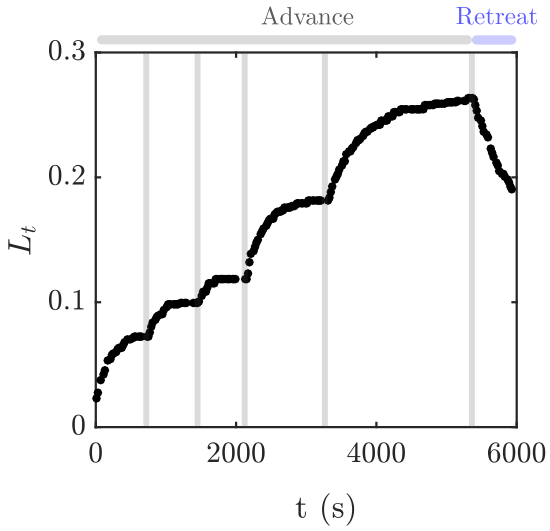

FIGURE 7.2.6: Toe length measured during experiment B. Vertical grey blocks delineate the times used for the evaluation of steady state reactive interfaces.

7.2.6.3 Colour Channels

Images from the chemiluminescent reactions revealed that there was substantial differences in signals for each of the colour channels. Figure 7.2.8 depicts the differences in images when splitting the image into blue, green and red channels. It is clear from the blue channel image that the emitted light signal is much more blurry than for the green and red channels. This could be explained by the fact that transparency varies with wavelength of emitted light, with shorter wavelength (i.e blue) being absorbed

more than green and red (Dever et al., 2001). This is also an important consideration when attempting to measure the width of the reactive zone as neighbouring grains absorb more of the emitted light, further rendering the width artificially large as depicted in Figure 7.2.8.

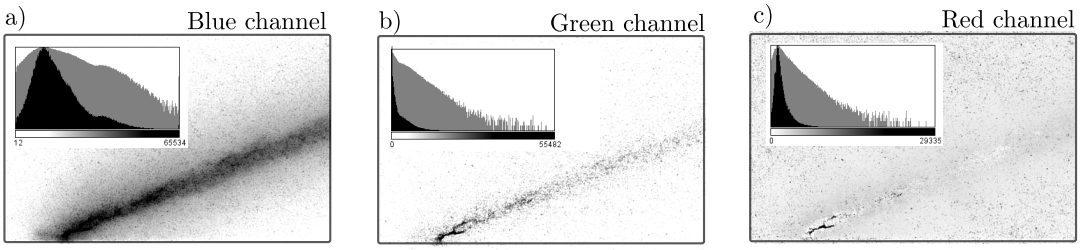

FIGURE 7.2.7: Example of colour channel images of chemiluminescence reaction at the toe of a steady state wedge. a) blue channel, b) green channel and c) red channels. Inset figures show the respective histograms for each channel. Light grey area depicts data in log-scale

Note that for the colour histograms from each image, the blue channel has the strongest light intensity followed by green then red. Due to the difficulty associated with adjusting the exposure time mid experiment, depending on the experiment, this results in the blue channel being over saturated. This is evidently be problematic when attempting to see the differences in maximum light intensity for varying fluxes. In general, despite lower light emittance, the green channel offers the most optimal characteristics. Revisiting Figure 7.2.8, it is evident that for the the mixing width of the green channel is much more narrow than the blue channel owing to less absorbance from surrounding grains and also less noisy than the red channel which is in part due to its weaker signal. Due to the aforementioned issues, images of reactions presented in the following, depict light intensities from the green channel.

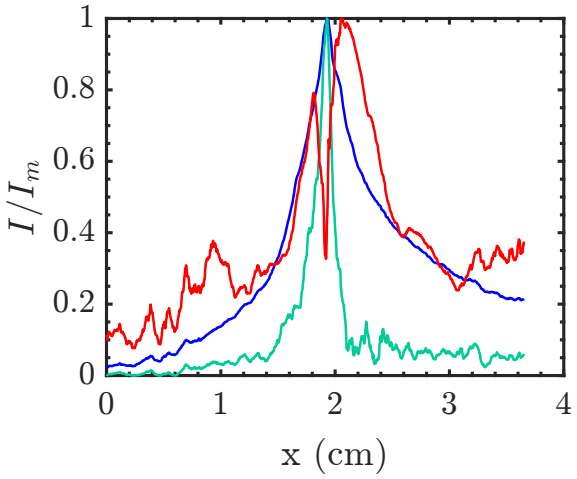

FIGURE 7.2.8: Normalised light intensity for each RGB Channel. Values are measured just above the toe perpendicular to the reaction interface

7.2.7 Diagnostics

As part of our analysis, several different quantities for each steady state configuration were evaluated. Visual representations of these quantities are presented in the illustration provided in Figure 7.2.9.

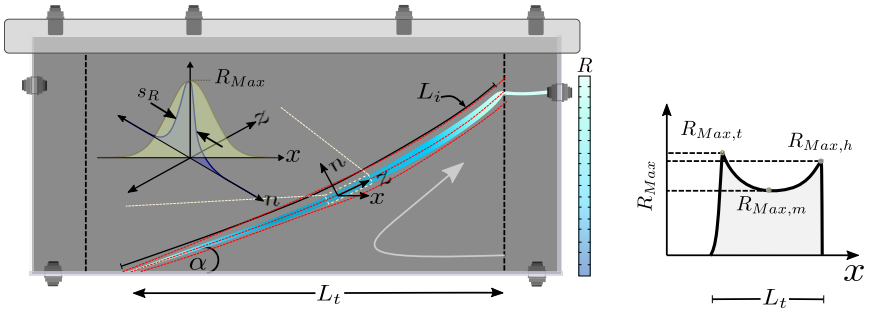

FIGURE 7.2.9: a) Schematic of reactive interface and the diagnostic quantities of interest. b) Generalized behaviour of reaction maximum along the interface.

Interface length

The interface length (L_i), is measured by following the reaction maximum along the mixing zone. For the transient case, individual images at each time are assessed.

Interface angle

The interface angle (α), is approximated by measuring angle between the bottom boundary and the interface angle in the vicinity of the toe. While this metric may under value the interface angle near the top of the interface, it captures the main trend.

Reaction maximum

The reaction maximum (R_{Max}), quantifies the maximum light intensity along the interface. This is evaluated locally at the toe, $R_{Max,t}$, the interface head, $R_{Max,h}$ and the local minimum,$R_{Max,m}$ located along the center of the interface. Due to the noise associated with maximum reaction rates, for the steady state images, $R_{Max,t}$ and $R_{Max,h}$ are determined by sampling light intensities over a manually specified block outlining the area of interest (see Figure 7.2.10a). From this window, the 90-th percentile R_{Max} is evaluated for each Pe.

Global reaction rate

The global reaction rate (R_g), is quantified by the total light intensity recorded across the entire domain. The average global reaction rate is determined by dividing the global reaction rate by the interface length.

Reaction maximum

The reactive width, s_R is determined by setting an appropriate tolerance over which to evaluate the reactive interface. This was done to overcome issues surrounding light scattering. The tolerance was adjusted manually in order to adequately capture the true reactive mixing width.

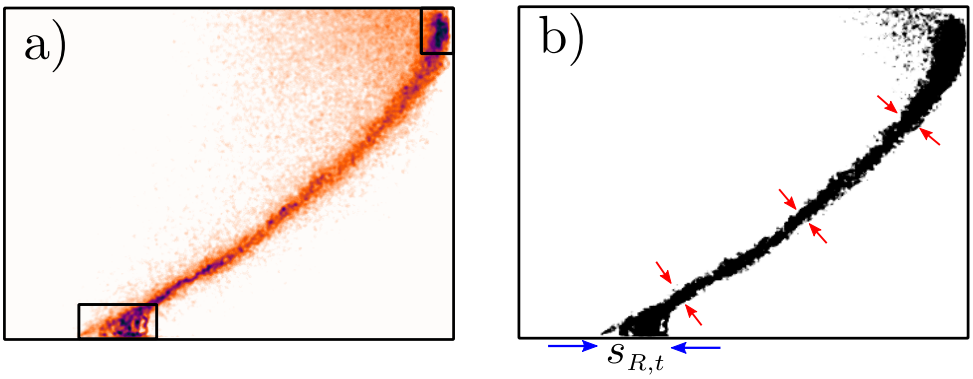

FIGURE 7.2.10: a) Experiment B.2, red box delinates sample over which $R_{Max,t}$ and $R_{Max,h}$ are calculated. b) Delinated interface for calculation of s_R.

An example of a delimited reactive mixing zone can be visualized in Figure 7.2.10b. At the toe the extent of s_R is measured along the bottom boundary while the rest is measured perpendicular to the interface.

Reaction enhancement

Finally, to assess the importance of the local reactive behaviour at the toe and head, we evaluate the reactive enhancement factor defined as,

$$RE = \frac{R_{Max,t/h}}{R_{Max,m}} \tag{7.3}$$

7.3 Results and Discussion

7.3.1 Steady state

7.3.1.1 Global reaction rate

Figure 7.3.1 shows the experimental global reactive behaviour against Pe for experiments B, C and D. The global reaction rate was found to grow approximately as $R_g \sim \mathrm{Pe}$. Given that the interface length decays as $L_i \sim \mathrm{Pe}^{-3/2}$ (Figure 7.3.1c), the average global reaction rate scales as $R_g/L_i \sim \mathrm{Pe}^{5/2}$. Therefore, the reaction rate per unit length increases with Pe, as expected due to higher flow rates which enhance mixing (Paster and Dagan, 2007). If R_g was controlled by co-flow mixing alone, as described in section 7.2, $R_g \sim L_i^{1/2}$. Substituting the measured decay of L_i, the global reaction rate should therefore follow $R_g \sim Pe^{-3/4}$. It is clear that dispersive growth via transverse dispersion alone is a poor predictor of the global reaction rate. In order to better understand the global behaviour, it is necessary to capture local reactive behaviours at the toe and head of the interface. It should be emphasized that the range over which Pe can be evaluated is restricted by the dimensions of the tank. Consequently, we can only evaluate quantities of interest across half a magnitude of Pe.

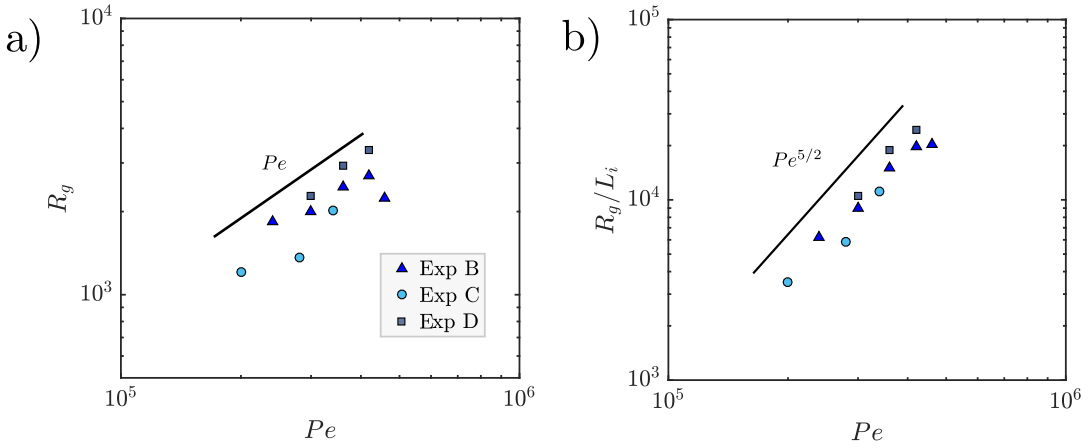

FIGURE 7.3.1: a) Global reaction rate b) Average global reaction rate

7.3.1.2 Mixing and Reaction patterns

Figure 7.3.3 illustrates the images of the steady state light distribution for each experiment performed at each ΔH. Qualitatively, enhanced reactivity is consistently observed at the toe and head of the interface with a local minimum located along the center of the mixing zone. This is better seen in Figure 7.3.5 which illustrates the maximum reaction rate along the interface. These reactive hotspots correspond to the position of enhanced mixing and strain rates observed in Chapter 4. They also correspond to locations of enhanced calcite dissolution in homogeneous media presented in Chapter 3 and in the work of Sanford and Konikow (1989) and Rezaei et al. (2005).

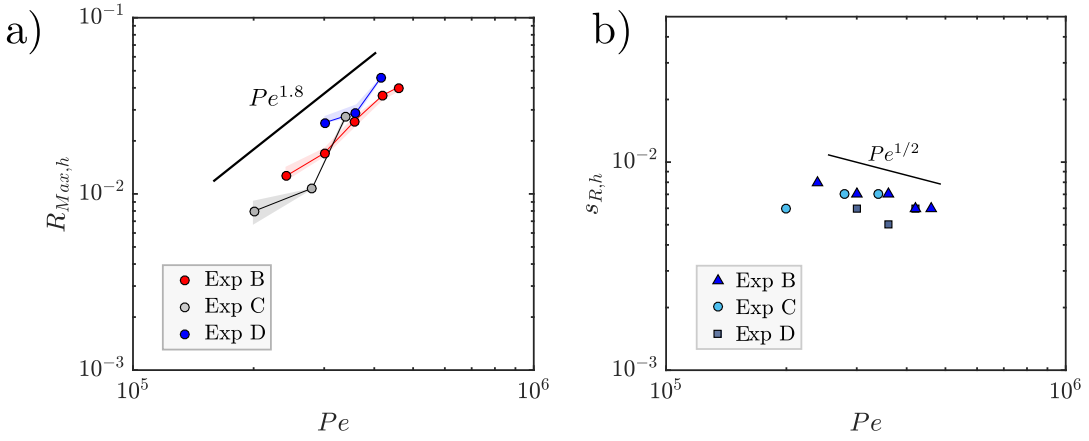

FIGURE 7.3.2: a) Experimental reaction maximum at the interface and b) reaction width at the interface head. c) Numerical reaction maximum and d) reaction width at the head.

Post-processed images of the conservative and reactive experiment for ΔH = 9 mm are shown in Figure 7.3.4. The square of the gradient of the concentration field is also provided in Figure 7.3.4b. High concentration gradients appear to be scattered across the entire mixing interface. Furthermore, sinuous nature of the concentration gradient distribution delineates the transport of mixed fluids in the pore spaces where flow can be focused locally (Acharya et al., 2007). The reaction rate along the

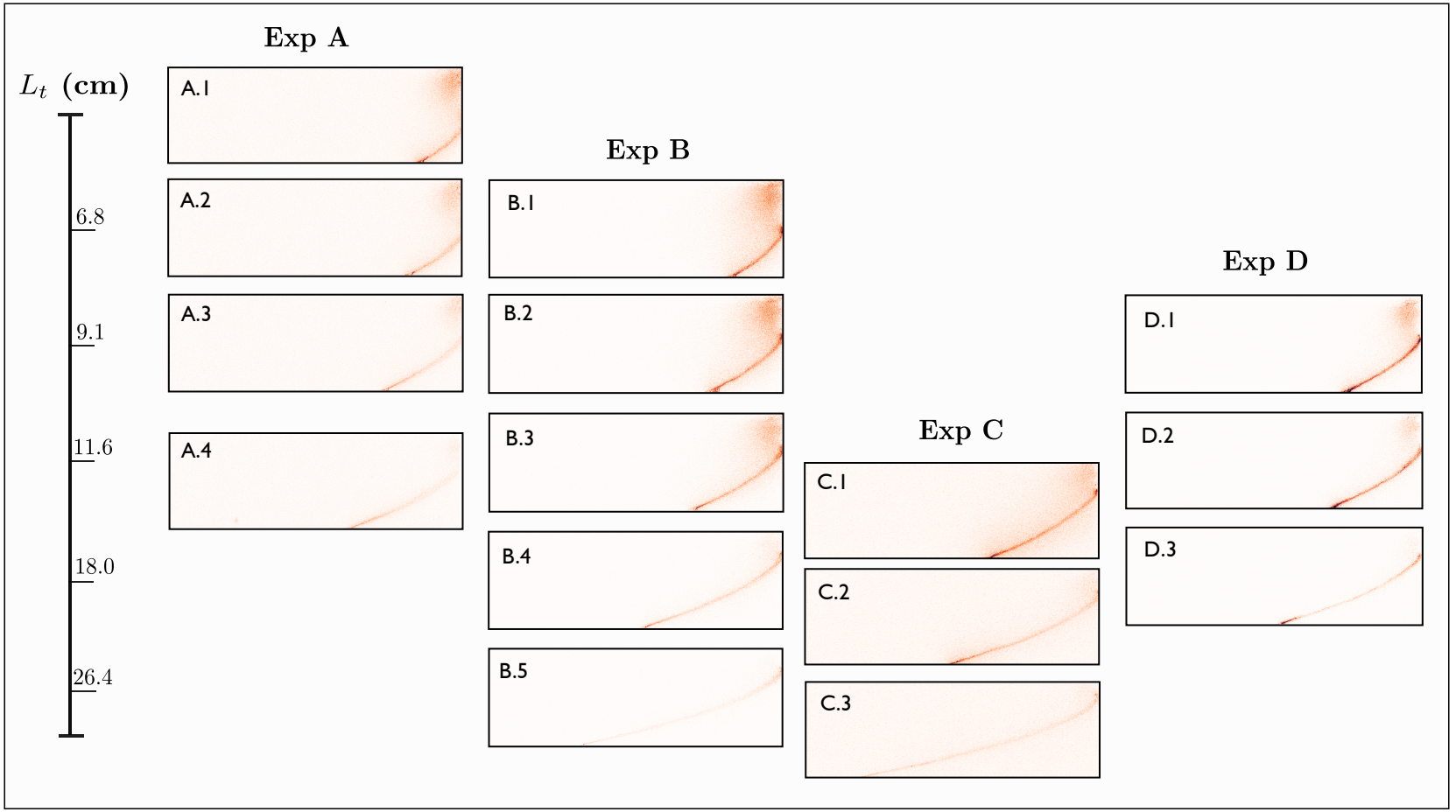

FIGURE 7.3.3: Light intensity distribution for experiments A-D. Images are positioned vertically such that their center corresponds to their toe length. Image colour intensities have been adjusted in order to better signify the relative change in reactivity from the first and last steady state positions

interface, however, does not appear to be sensitive to localized areas of high concentration gradients. In transport problems defined by a constant diffusion coefficient, high concentration gradients would directly imply high mixing rate. However, in the case of seawater intrusion, velocity-dependent dispersion must be considered to adequately describe mixing (e.g. Abarca and Clement, 2009). As noted by Pool and Dentz (2018), if the interface is locally compressed or stretched, this can steepen the concentration gradient, but it is only when local dispersion is sufficiently strong that this can lead to enhanced mixing. Therefore, in mixing problems characterised by velocity-dependent dispersion and non-uniform flow, chemiluminescent reactions may provide useful information that cannot be captured by conservative mixing metrics alone.

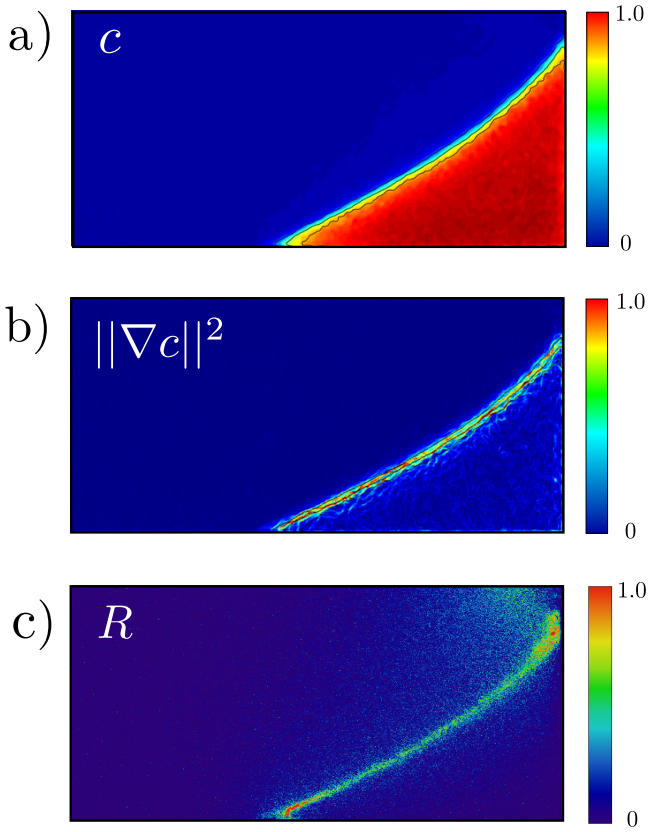

FIGURE 7.3.4: Image map of the a) concentration, b) the concentration gradient and c) the reaction rate in experiment B. All images have been normalized by the maximum pixel intensity.

In the following we will quantitatively assess the local reactive behaviours along the interface. We start by evaluating the toe, followed by the interface center and finally the head of the interface.

7.3.1.3 Reaction at the interface toe

We start by highlighting some features of the imaged reaction at the toe. This is demonstrated in Figure 7.3.6, where we show four zoomed in snap shots of the toe as the wedge intrudes. Note that each snap shot is captured with an exposure time of 10 seconds. The most evident feature in these images is that we are clearly sampling reaction rates occurring within the pore space. Note that the average filtering used during processing is over the size of the pore space, not several grains. This differs

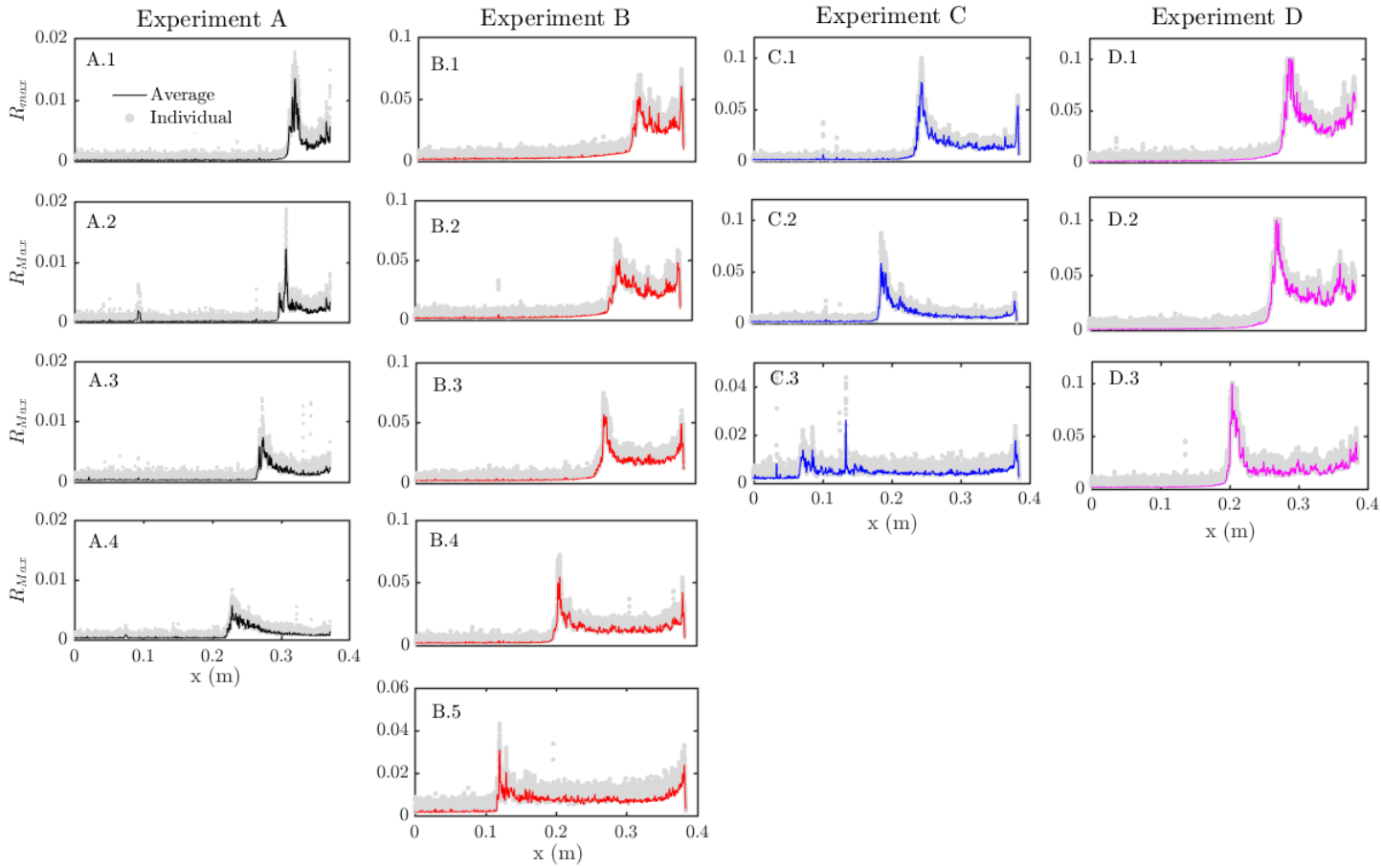

FIGURE 7.3.5: Reaction maximum along the interface along the x-axis. Grey points represent green color channel images after 5 x 5 mean filtering. Coloured lines represents maximum intensity after averaging over several steady state images.

from previous reactive-mixing experiments where much finer grains were employed (e.g. Gramling et al., 2002). It is likely that obtained results are strongly influenced by pore-scale effects owing to the non-homogeneous velocity structure induced by the anisotropic grains. Darcy scale descriptions of reactive transport may therefore be inadequate when attempting to predict the reactive rates in this set-up, especially for high Pe flows (Tartakovsky et al., 2009). Another distinct feature is that despite some transparency in the grains as depicted in Figure 7.2.2a, the observed reaction is mostly limited to the pore space along 1-2 grains deep. It is clear that the reaction intensity of the chemiluminescent reaction combined with poor opacity of the grain, prevents light from being transmitted through the grain.

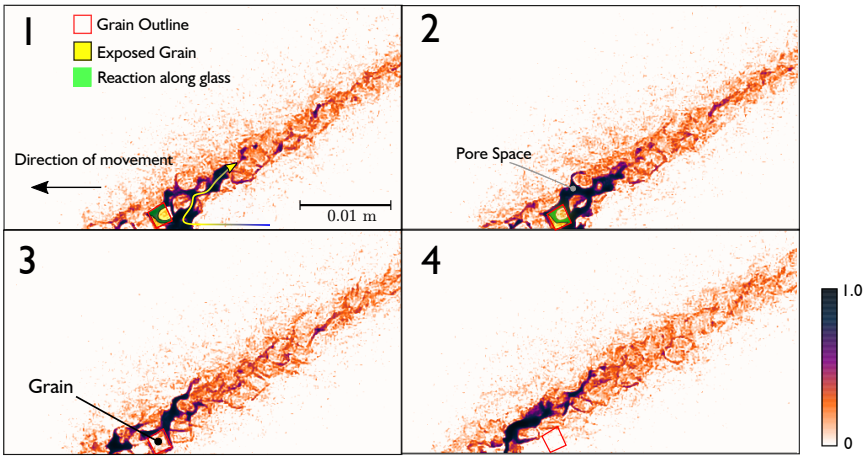

FIGURE 7.3.6: Zoomed in snap shots of toe during an advance of the wedge in experiment C. Each image represents the integrated light after the 10s exposure time.

We are therefore only capturing a thin slice of the bulk reaction across the interface, i.e, the images only represent quasi 2-D reaction interface. One must therefore assume the reactive behaviour observed over a couple of grains is representative across the entire thickness of the flow cell. Finally, by following the grain outline in Figure 7.3.6, it is clear that some of the reaction is occurring directly along the grain/glass boundary. It could be argued that this is some artefact created by mixing along the grains and the glass surface. However, the fact that enhanced mixing and reactions have similarly been observed at the toe in Darcy scale simulations suggest that the two reaction hotspots are truly the result of flow induced by variable density flow.

Figure 7.3.7a shows the results for the reaction maximum at the toe, $R_{Max,t}$ with respect to Pe. Under steady state conditions, there is opposing flow from the salt and freshwater in the vicinity of the toe, resulting in a stagnation point (Chang and Clement, 2012a). As we saw in Chapter 6, for purely diffusive mixing across a saddle point, it is expected that $R_{Max,t} \sim Pe^{2/3}$. Our results indicate the $R_{Max,t}$ generally increases with Pe. It appears that at low Pe, $R_{Max,t}$ strongly decays as evidenced by Exp C. However, for larger Pe, the reaction maximum begins to level off. Unlike the Hele-Shaw experiment in Chapter 6, no robust scaling behaviour is identified. This is further confounded by the limited number of data points and the limited range over which Pe can be evaluated. As demonstrated by the porous media milifluidic experiments, the presence of grains can strongly alter local velocities which may strongly increase compression rates in the pore-space, resulting in higher than

expected and noisier reaction rates. Previous reactive transport simulations looking at calcite dissolution across the salt-freshwater mixing zone have suggested that the reactive hotspot at the toe is due to an initial mixing effect. Since there are no additional dissolved calcite in solution, this area would be most undersaturated with respect to calcite, thereby enhancing calcite dissolution (Rezaei et al., 2005; Sanford and Konikow, 1989). However, results from this experiment suggest that the kinetics of calcite dissolution alone cannot explain the presence of this reactive hotspot, which is strongly dictated by non-uniform flow.

Note that reaction rates for each experiment vary slightly. For example, $R_{Max,t}$ for experiment D is the highest, followed by experiment B and C. As discussed in Chapter 5, reactions involving chemiluminescence are generally quite sensitive to a number of factors ranging from small changes in solution pH, the presence of impurities the flow chamber and room temperature. It is therefore possible that small changes in the experimental conditions resulted in different reactivity between experiments. Despite this, the general reactive characteristics do not appear to differ substantially.

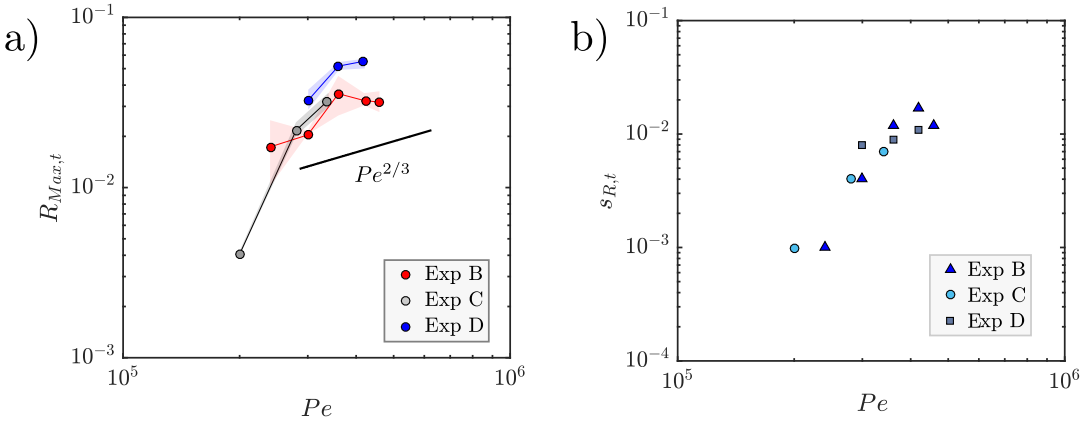

FIGURE 7.3.7: a) Reaction maximum at the toe. Shaded area denotes the variability in $R_{Max,t}$ from non-averaged steady state images. b) Reaction width at the toe.

Figure 7.3.7b illustrates the reactive width at the toe, $s_{R,t}$. As for the previous analysis, the expected behaviour for diffusive mixing (under constant density) at a stagnation point is considered. As demonstrated in Chapter 5, the reactive width $s_{R,t}$ should decay as $\mathrm{Pe}^{-1/6}$. Our results show the exact opposite behaviour, with s_R growing very strongly with an increase in Pe. Similar to the behaviour of R_{Max}, at low Pe, $s_{R,t}$ initially grows very strongly before levelling out at higher Pe. Zoomed in snap shots of the toe for each experiment provided in Figure 7.3.8 illustrate the change in $s_{R,t}$ for the range of Pe investigated.

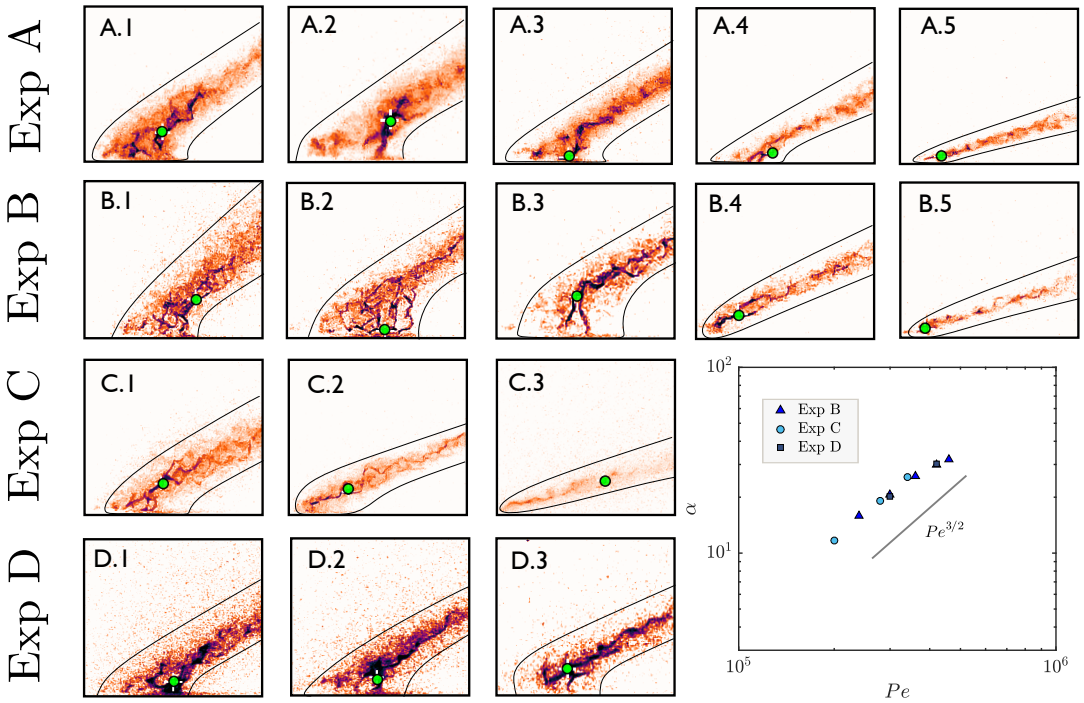

FIGURE 7.3.8: Zoomed-in images of light intensities observed at the toe for each experiment. Images from left to right represent the lowering of the freshwater head and subsequent increase of toe length. Black lines denote coarse outline of the mixing zone and the green dot represent the location of maximum recorded light intensity within the frame. The scatter plot in the bottom right shows the angle at the toe as a function of Pe

On the other hand, non-uniform packing, particularly at the base of the tank, together with the anisotropic grain shape, might result in strong longitudinal mixing at the toe. This would be more prevalent at high Pe, when the interface angle is larger and flow approaching the toe is, respectively speaking, more orthogonal with respect to the mixing interface (see Figure 7.3.8). Under velocity-dependent dispersion, for which we are concerned, this would presumably lead to larger mixing widths at higher flow rates. This is in contrast to the center of the interface where flow is dominantly aligned tangential to the interface and therefore transverse mixing prevails. Studies that have evaluated conservative mixing in sand-filled tanks with comparably sized glass beads have generally observed very narrow mixing widths at the toe (Abarca and Clement, 2009; Robinson et al., 2016). These studies indicate an almost finite mixing zone dictated by very small transverse dispersivities. On the other hand, results from (Yoshihiro Oda, Tamio Takasu, Hirashi Sato, Atsushi Sawada, 2010) who also used sand-sized glass beads showed locally wide mixing zone at the toe, particularly at towards the high salt water concentration isolines. It is therefore unclear as to whether the large reactive width observed at the toe is solely due to the nature of packing and type of grains used or whether it is strongly influenced by the flow structure.

While our study has focused on evaluating the impact of changing the flow rate on reactive mixing, it is also crucial to mention the role of buoyancy effects which are also dependent on the the flow rate. This is typically evaluated using the gravity number which is defined as $Ng = kg\Delta\rho/\mu q_f$, where k is the hydraulic permeability, g is the gravitational acceleration and μ is the viscosity. This non-dimensional parameter indicates the competition between gravity-induced flow (resulting from a

difference in density) and forced convection . As the freshwater velocity is increased by increasing the hydraulic head gradient, Ng also decreases, therefore buoyancy effects become smaller. As a result this may lead to larger mixing-widths, which may help to explain the reactive widths at the toe (Dell'Oca et al., 2018).

While our analysis has so far relied on analytical scalings dervied for stagnation point mixing, it should be reiterated that this description lacks a lot of complexity that is likely present for the seawater intrusion problem. As mentioned above, a change in interface geometry means the angle of flow relative to the mixing interface decreases with a decrease in flow velocity. The stagnation point at the toe therefore represents oblique saddle point whose compression rate depends on the interface angle. We therefore have both a longitudinal and transverse component that plays a role in mixing. Determining an appropriate transverse dispersion coefficient in experimental studies generally proves to be a difficult task in and of its self, often displaying non-linear dependencies with Pe, attributed to pore-scale effects resulting from incomplete mixing Perkins and Johnston, 1963; Klenk and Grathwohl, 2002. Previous studies have also noted the need for compound-specific descriptions of transverse dispersion Chiogna et al., 2010; Rolle et al., 2012. As indicated previously, the impact of buoyancy effects is also critical to adequately describing mixing and reaction for variable density flow problems. The study by Grane and Gardner (1961), for example have shown that as the gravity number increases, the amount of mixing can significantly decrease. This is particularly important for high permeability media. Neri (2009) has also shown that transverse dispersivity is a function of both fluid velocity and density differences. While these factors may not directly explain the results found at the toe, it highlights how local pore scale effects could play a role in the reactive behaviour at the toe and should be considered in future studies.

7.3.1.4 Reaction along the interface

Figure 7.3.9 illustrates results for R_{Max} and s_R along the interface from the toe. For a co-flow mixing configuration, it is expected that $R_{Max} \sim x^{-2/3}$ and $s_R \sim x^{1/6}$ (see Appendix Section 7.A). Results for R_{Max} generally show good agreement with the expected analytical decay, particularly for experiment C and D. The measured reactive width was very noisy, and for the exception of experiment C, did not show any clear scaling. In general, due to the issues regarding light scattering, the reactive width proves to be a less reliable metric when evaluating reactive mixing away from the toe. The initial decay of R_{Max} and growth of s_R continues up to some critical distance, x_m (4-5 cm from the toe). This distance appears to be the same for all experiments and independent of Pe. At high Pe when the interface length is small, R_{Max} either increases directly after x_m (e.g. Figure 7.3.5 B.1 and D.1), or it levels off to some uniform value before increasing again near the head of the interface (e.g. Figure 7.3.5 images B.5, C.3 and D.3). This shift in behaviour is also captured in the reactive width, where it proceeds to grow more strongly after x_m. For experiment B, the growth following x_m follows, $s_R \sim z^{1/2}$ whereas for experiment C and D this is closer to $s_R \sim z^{1/3}$.

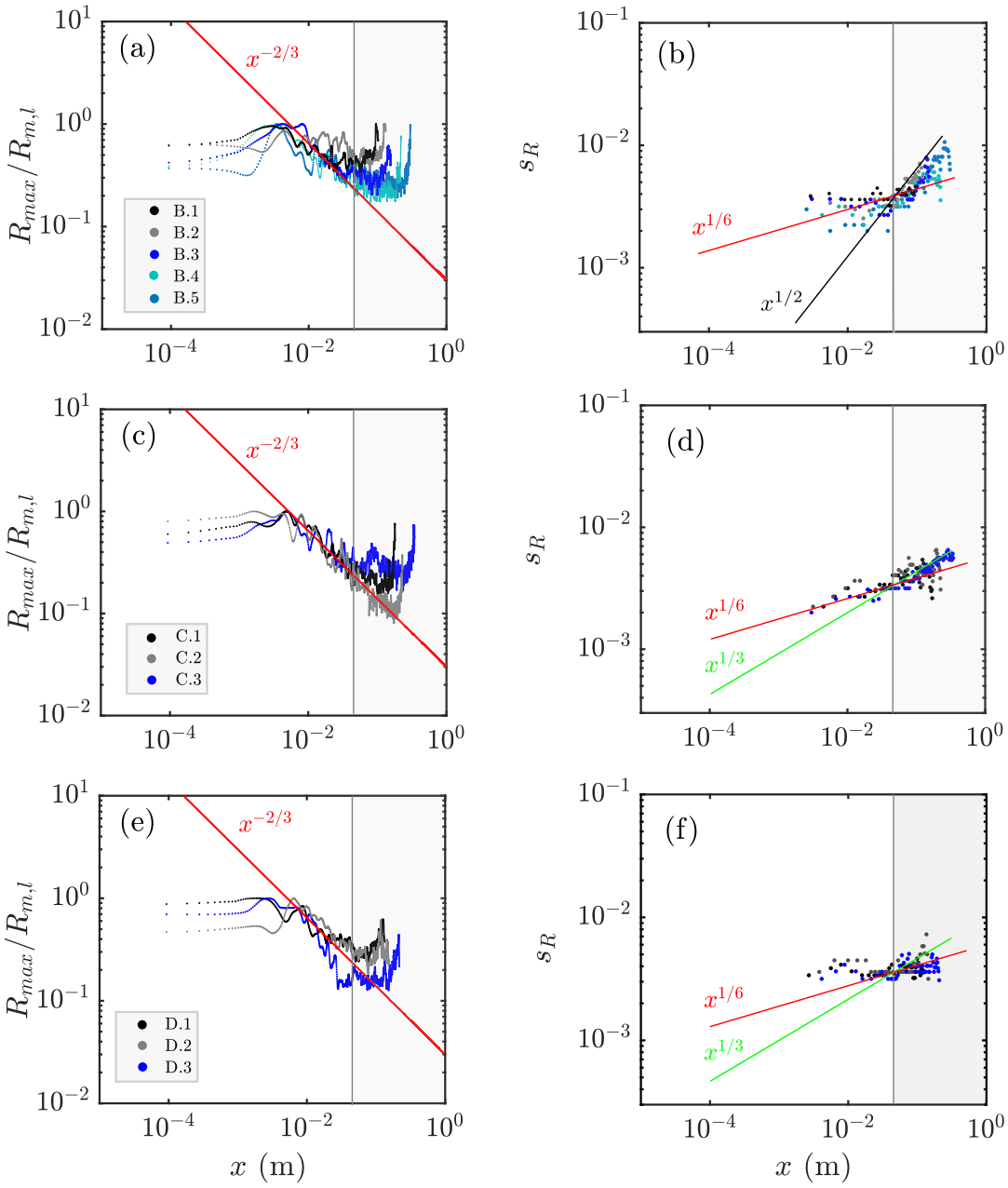

FIGURE 7.3.9: R_{Max} normalized by the maximum local reaction rate, $R_{m,l}$ along the interface from the toe to the interface head. Shaded area depicts the behaviour after the critical distance x_m.

This transition may demarcate a characteristic cross over distance, akin to the mixing time that dictates the cross over time between two mixing regimes (Villermaux, 2012; Le Borgne et al., 2015). For this specific problem, it may represent the cross over distance between dispersive relaxation and a mechanism that suppresses further decrease in R_{Max}. This could be attributed to increasing tangential velocity along the interface. Based on the findings of Chapter 4, this may be attributed to strong flow acceleration as it approaches the interface head, resulting in considerable stretching of the interface, thereby enhancing reactions near the outlet.

7.3.1.5 Reaction at the interface head

The local reaction rate maximum and reaction width at the interface head are evaluated in Figure 7.3.2. As seen with $R_{Max,t}$, there is a strong increase in $R_{Max,h}$ with Pe for all experiments. Experiment B grows as $R_{Max,h} \sim \mathrm{Pe}^{1.8}$, with experiment C and D showing similar trends. Unlike the toe, $R_{Max,h}$ does not appear to saturate high Pe. Measurements of the experimental reactive width shows little to no discernible changes for experiment C and D, however in experiment B, the width decreases as $s_{R,h} \sim Pe^{-1/2}$. This may be attributed to enhanced stretching near the outlet which compresses the mixing interface.

7.3.1.6 Reaction enhancement

The enhancement factor, RE_t and RE_h are evaluated with respect to the toe and head respectively. For the exception of Experiment C, RE_t and RE_h decreases with an increase in Pe (Figure 7.3.10a-b). In other words, the difference between the maximum toe and head to the local maximum becomes larger as the interface lengthens. For the exception of experiment C, it found that RE_t can range between 2∼6.5 and RE_h ranges between 1∼12. Note that these values are subject to some uncertainty since the reaction rate minimum obtained along the center of the interface is subject to a high degree of noise due to having small light intensities.

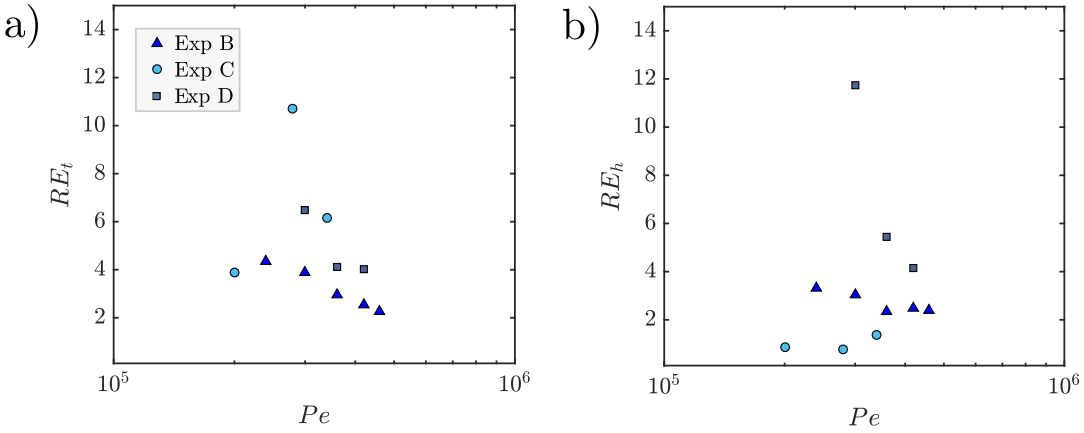

FIGURE 7.3.10: Reaction enhancement, RE, given by the ratio of the R_{Max} at the toe, RE_t and head, RE_h to the local minimum. (a-b) RE for the experimental test cases and (c-d) RE for the numerical simulations

7.3.2 Transient

7.3.2.1 Advance and Retreat

Figure 7.3.11 shows the results for the transient experiment. The interface at the beginning of image aquisition and at 4080 seconds into the experiment is illustrated in Figure 7.3.11b. Note that at early times, when the velocity is also highest, the reaction rates along the interface are also largest. This is reflected by high values of R_{Max} at the toe, the reaction minimum along the interface and head of the interface. This is also demonstrated in Figure 7.3.11d which shows the average global reaction rate over time. As the freshwater head is dropped and the interface intrudes further in, R_{Max} at the toe and head remain high. It is only after the third and fourth steady state positions that a strong decrease of R_{Max} at the toe and head is observed. In contrast, the reaction rate along the center of the interface decays significantly as

represented by R_{Max} min. This separation between reaction rates at the head and toe with respect to the center is what distinguishes the local reactive hotspots at each end of the interface. This can be explained given that at early times, the entire interface experiences similar freshwater flow velocities. As the interface grows, the velocities experienced along its length becomes much more non-uniform. The response of the average global reaction rate is very similar to the behaviour of the minimum R_{Max}, as evidenced by their step-wise response to a decrease in freshwater hydraulic head (see Figure 7.3.11a and d). This suggests the mid-section of the interface is an important metric when describing the global reaction dynamics. Unlike the average global reaction rate, at early times, the global reaction rate is initially small. Once again, this is due to the small size of the interface. In our evaluation of the steady state global reaction rate in the previous section, it was noted that R_g grew with an increase in Pe, however it is clear from this transient experiment that when the interface is small enough, R_g will eventually decrease. There is therefore a non-monotonic relationship between the size of the interface and the global reaction rate.

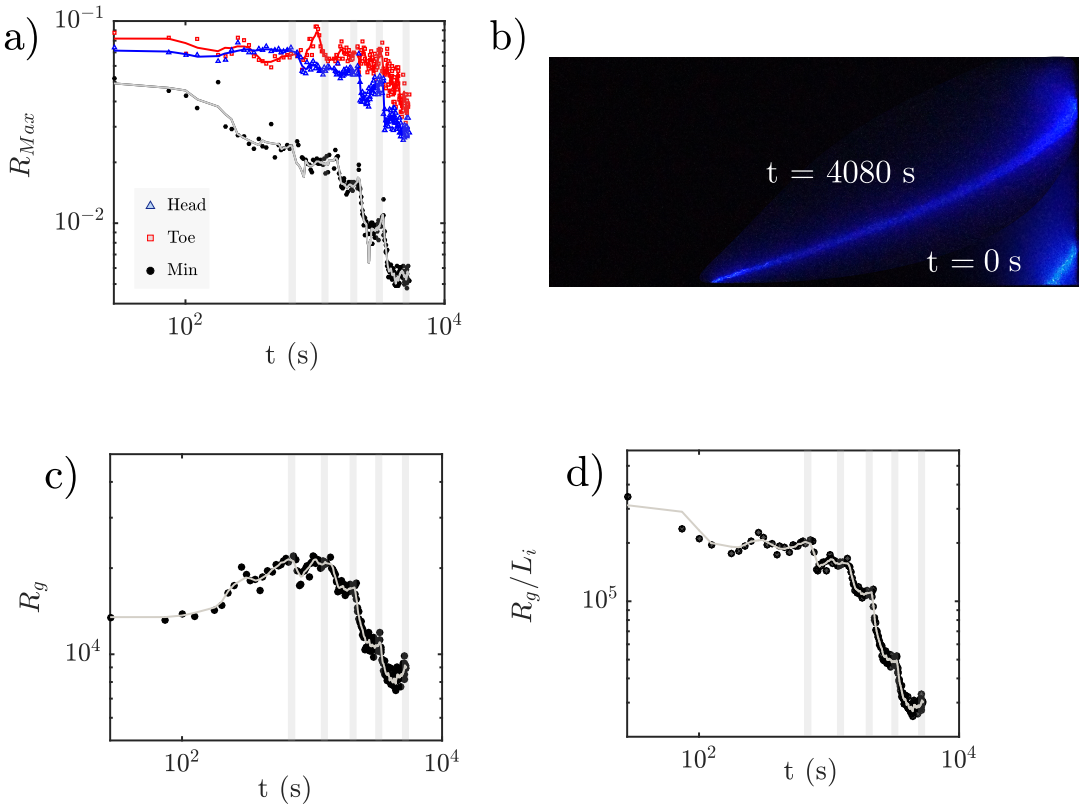

FIGURE 7.3.11: Transient R_{max} behaviour for experiment B. a) R_{max} the head toe and minimum, b)superimposed reactive interface at time = 0 and time = 4080 s, c) the global reaction rate and c) the average global reaction rate. Solid line represents a one minute moving average. The grey rectangular blocks represent the time where the interface is at steady state

It is important to note that as the interface transitions between advancing to its new steady state configuration, all quantities show a slight increase in reactivity. This is particularly apparent in R_g and R_{Max} at the head and min and indicates a change in mixing dynamics between an intruding wedge and a wedge at steady

state. Chang and Clement (2012a) investigated the changes in the velocity field during steady state, an intrusion and retreat of the SFI. During steady state and an intruding wedge, salt and fresh water flow orthogonal from their respective boundaries toward the mixing interface and recirculate up along the mixing zone, thereby forming the typical convection cell. Chang and Clement (2012a), however noted that during an intrusion, the convection cell becomes slightly distorted and flow vectors pointing landward extend further into the mixing zone before recirculating upwards. Once steady state is achieved, however, these vectors shift back behind the mixing interface. The fact the global reaction rate decreases slightly during an intrusion could be tied to the fact that we have stronger longitudinal mixing which smooths concentration gradients along the interface, thereby decreasing the reactivity. During a retreat of the wedge, Chang and Clement (2012a) also noted that flow inside the saltwater wedge is redirected towards the salt water boundary. Although flow across the bulk of the mixing zone is still orientated along the mixing interface, flow in the vicinity of the toe becomes unidirectional towards the saltwater boundary.

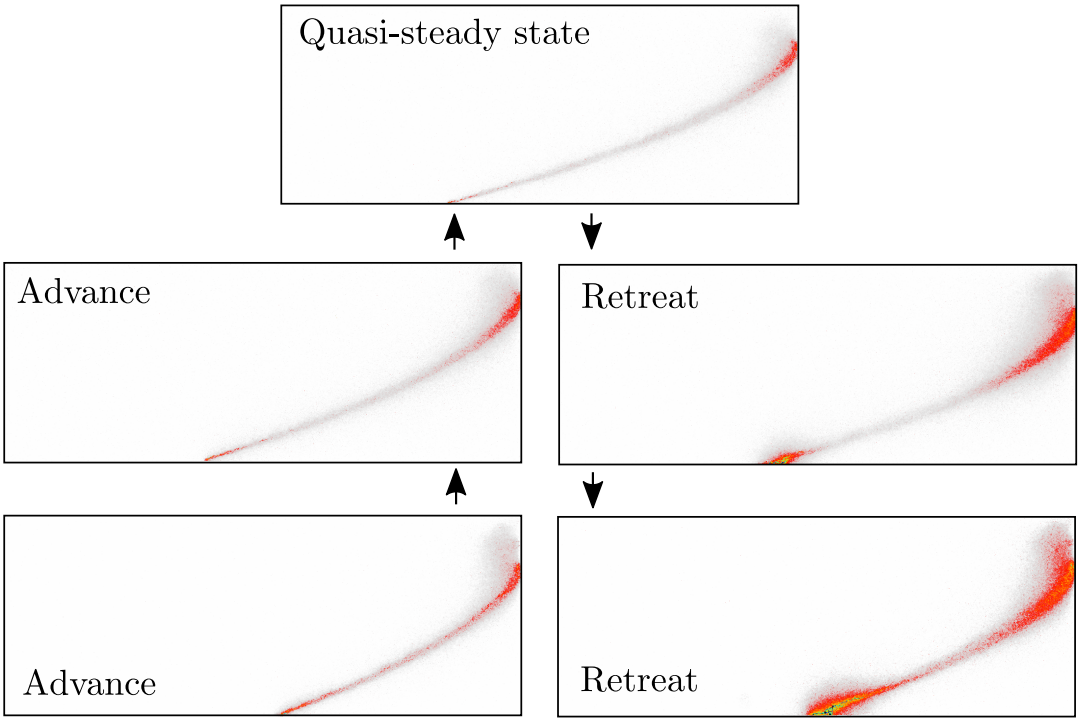

FIGURE 7.3.12: Image of reactive interface at similar toe lengths during an active advance and an active retreat

Differences in reactive mixing behaviour are shown in Figure 7.3.12. Qualitatively, there is not a significant difference between an advancing wedge and quasi-steady state wedge since the convective cell remains intact. In contrast, during a retreat, the reactive interface becomes visibly wider, namely near the toe and discharge zone. A similar response has also been observed in conservative seawater intrusion and retreat experiments. In an experimental sand tank study, Abdoulhalik and Ahmed (2018) found that during an intrusion there was little change in the average conservative mixing width, however during a retreat, there is a strong momentary increase in the mixing width before it narrows again at the new steady state position. It is apparent that the redirection of flow seaward has a strong influence on

both the conservative and reactive interface width. This change in flow would certainly result in stronger longitudinal mixing as opposed to transverse mixing which dominates during an seawater intrusion and at steady state. Another interesting observation is that the local reaction hotspot at the toe persists even during a retreat. If the maximum reaction rate at the toe at steady state is indeed controlled by stagnation point flow, then this would naturally be lost when flow becomes unidirectional. Its persistence may be explained by the velocity difference of freshwater flow towards the wedge and within the salt water wedge which is much slower (Chang and Clement, 2012a). It is important to note that the the movement of the saltwater wedge inland and during a retreat occurs over different time scales (Robinson et al., 2016; Lu and Werner, 2013). For example the movement of the wedge during a retreat towards its new steady state position is faster than during an advance (Robinson et al., 2016). Faster flow velocities during a retreat would therefore further enhance dispersion, therefore play a strong role in mixing and reaction dynamics. Coastal aquifers that experience strong hydraulic perturbations (e.g. tides and seasonal recharge oscillations) that act on different time scales, may therefore exhibit interesting global reactive responses.

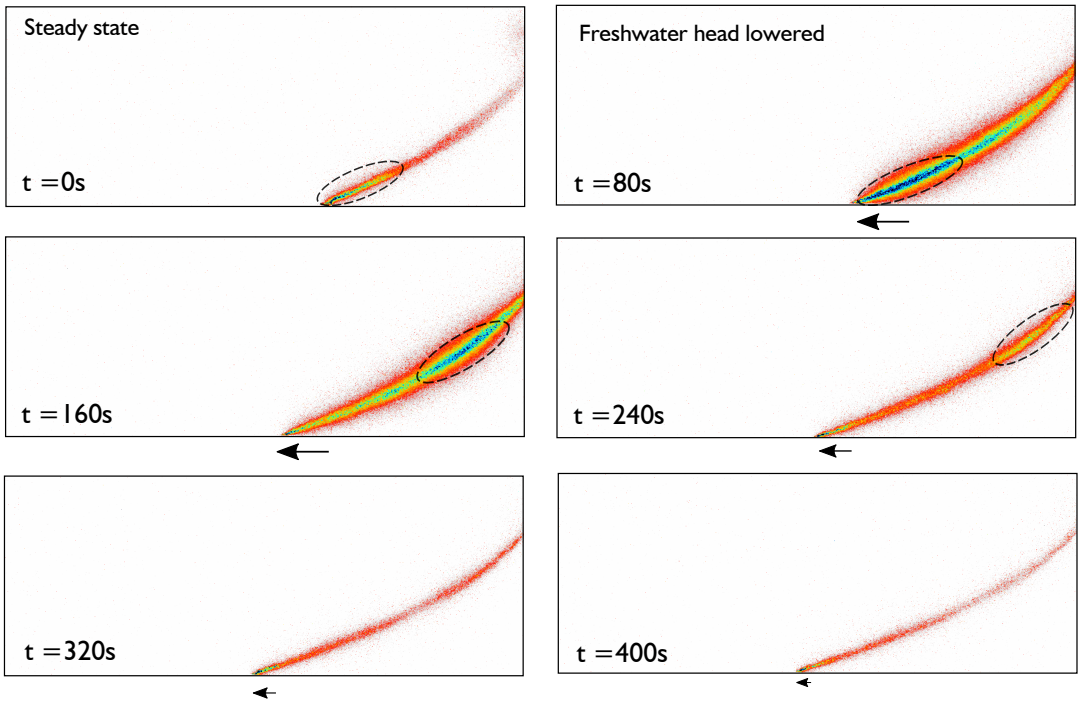

FIGURE 7.3.13: Transient movement of interface in Experiment A. Images show movement of wedge after lowering the freshwater head.

7.3.2.2 Reactive pulse

An interesting transient response was observed following a drop in the freshwater head (see Figure 7.3.13). This behaviour was best captured in experiment A. The result is a reactive 'pulse' that travels from the toe up along the interface where it eventually dissipates at the head. Eventually, once the wedge approaches a quasi-steady state position, only the reactive hotspot at the toe remains. While the same phenomenon was observed in the other experiments, the magnitude of this effect appears to diminish as the experimental reactivity increases. Consequently, this phenomenon is less evident in experiment B, C and D. Although the pressure drop after

dropping the freshwater head is almost instantaneous, the pulse appears to take over four minutes before dissipating. A coarse approximation would suggest the center of this pulse moves at $v_{pulse} \sim 5 \text{ x } 10^{-4}$ m/s, which may roughly indicate the local velocity along the interface. A possible explanation for this process could be linked to local stretching of the interface as it moves inward and upwards along the salt water boundary. The propagation of this pulse upwards may therefore be the result of an asynchronous shift of the toe and interface head. Since the movement of the toe inward is much more pronounced after a drop in freshwater head, this may explain the origin of the pulse at the toe. With little understanding of this mechanism it has yet to be seen whether this phenomena would be significant let alone occur at field scale. Nevertheless from a mixing dynamics point of view, it presents an interesting occurrence that, to the authors knowledge has not been observed in other experimental porous media transport problems.

7.4 Summary and Conclusion

In this chapter we have assessed reactive mixing across the SFI for several steady state interface configurations by altering the freshwater head. We have shown that even with a decrease in flow velocity, there exists a persistent local reaction hotspot at the toe for all steady state configurations. Although the toe is characterized by a stagnation point, we do not recover the analytically derived scaling laws for the reaction maximum and reaction width presented in Chapter 6. Rather than narrowing due to enhanced compression, the reactive width at the toe grows wider with an increase of Pe, which we attribute to enhanced longitudinal dispersion. As we move away from the toe, the maximum reaction rate decays until some critical distance is reached. This decay appears to follow the expected scaling for co-flow mixing. Moving further up along the interface, the reaction begins to increase again towards the head, where another local reaction hotspot is observed. This hotspot is associated to enhanced flow velocities along the interface which lead to accelerating flow and therefore enhanced stretching. Consequently, the reaction maximum at the toe increases with increasing Pe while the reactive mixing width compresses. Note that the reactive patterns observed in this study were very similar to those demonstrated by Sanford and Konikow (1989), in their investigation on mixing-induced calcite dissolution. We have shown that the reaction hotspot at the toe is strongly influenced by non-uniform flow and not solely attributed to calcite under saturation. This study shows the utility of luminol chemiluminescence to investigate the role of mixing for in heterogeneous flow, even for more complex geochemical reactions which are fast compared to rates of transport.

Images of the reaction during its advance and retreat has also shed light to interesting mixing behaviours which are attributed to the direction of flow in the fresh and salt water domains. We have shown during steady state, global reactivity is enhanced as compared to during intrusion. This is attributed to enhanced longitudinal dispersion that results from opposing flow vectors within the salt water wedge to extend further into the mixing zone. During a retreat however, flow becomes unidirectional towards the saltwater reservoir. This results in a wider reactive mixing zone which is also attributed to longitudinal mixing. We note that the reaction hotspot at the toe also remains intact during the retreat, despite flow becoming unidirectional. This is thought to be due to lower velocities in the salt water wedge compared to the freshwater flow, which continues to compress the interface at the toe. In response to a drop in freshwater head, we have also observed a reactive pulse that originates

at the toe and moves upwards along the interface. We hypothesize that this may be due to localized stretching as the interface elongates.

In order to better understand mechanisms at play, there are a number of things that could be investigated in more detail. For example, chemiluminescent experiments could be performed using more simple mixing set-ups, such as co-flow or stagnation point mixing. This would serve to also validate analytical scalings for porous media flow. Although stagnation point flow was tested in the Hele-Shaw cell, ultimately, flow and consequently reactions in 3D porous media (quasi-2D) is much more complex. In addition, effort should be placed on determining up scaled transport parameters experimentally which may be influenced by pore-scale processes. This could also be complemented by numerical simulations to see whether processes at the tank scale can be replicated by Darcy scale simulations.

Appendix

7.A Reactive Mixing along the interface

In the following we outline the expected reactive behaviour of the interface as we move away from the toe along the interface. In chapter 4, we found that the growth of the mixing width could be approximated by $s \sim \sqrt{\alpha_t z}$, where α_t is the transverse dispersivity and z denotes the coordinate axis along the interface. Conceptually this is similar to a co-flow mixing configuration, where two initially segregated reactive solutes are injected to the top and bottom half of the domain under uniform flow conditions. Using the same method presented in chapter 6, we outline the expected behaviour of $R_{Max}(z)$ and $s_R(z)$. We employ the same expression for the reaction rate which can be extended to different types of compression,

$$R(n,\theta) \approx \frac{\tilde{s}_0^{-4} s^{-2/3}\theta^{-4/3}\theta^{-2/3}\mathsf{Da}}{\lambda^2} Ai\left(\frac{\lambda n}{\tilde{s}_0} s^{1/3}\theta^{1/6}\right)\left(\frac{\lambda n}{\tilde{s}_0 s^{1/3}\theta^{1/6}}\right). \tag{7.4}$$

We recall that n is the coordinate axis perpendicular to the mixing interface, s is the mixing width and θ is the warped time. For the problem under consideration, the interface does not experience any compression and only grows via dispersion. Accordingly, the definition for warped time is simply given by $\theta = (D/s_0^2)t$, where t is the time available for mixing which can be expressed as $t = z/v$. Here, we consider the case where mechanical dispersion prevails such that $D = \alpha_t z$, where v is the average linear velocity. We therefore arrive at the following scaling behaviours for the reactive interface. The reactive width, s_R is expected to grow as,

$$s_r(z) \sim \mathsf{Da}^{-1/3} z^{1/6}, \tag{7.5}$$

and the reaction maximum to decay as

$$R_{Max}(z) \sim \mathsf{Da}^{1/3} z^{-2/3}. \tag{7.6}$$

The integrated reaction across the reactive interface can therefore be approximated as,

$$R_c(z) \sim z^{-1/2}. \tag{7.7}$$

Integrating this over the length of the interface gives the expected scaling for the global reaction rate.

$$R_g \sim L_i^{1/2} \tag{7.8}$$

where L_i is the interface length. Note that while these descriptions are not dependent on the the Pèclet number, it is ingrained in the description of L_i which changes as the freshwater head is altered.

7.B Experimental sand tank and porous media

In Figure 7.B.1 we show a detailed plan of the experimental sand tank from all perspectives.

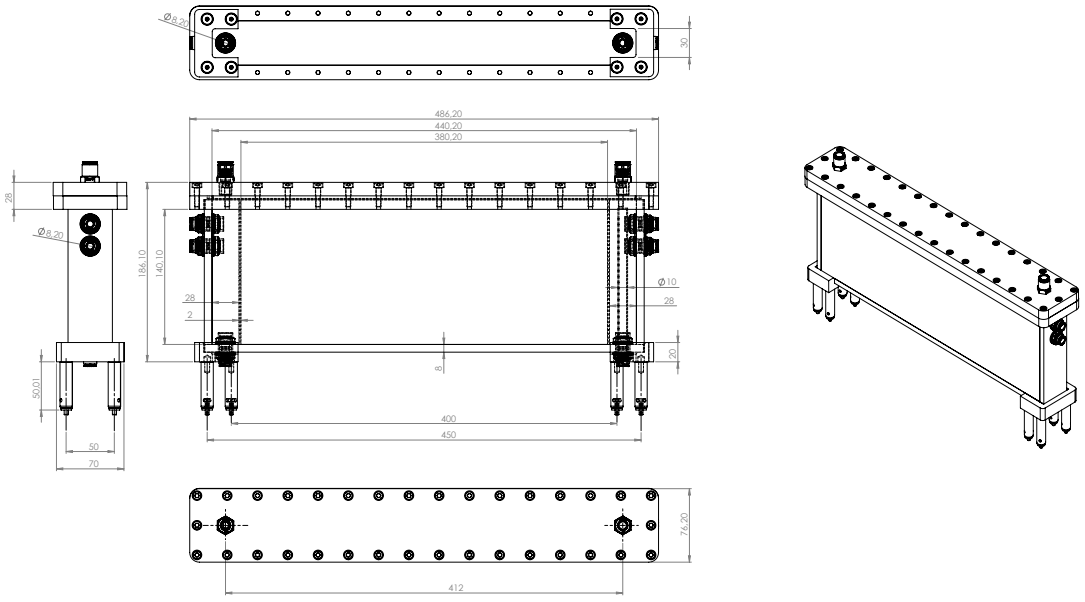

FIGURE 7.B.1: Plan of experimental sand tank

.

In Figure 7.B.2, we present the results used for the determination of the hydraulic conductivity. We plot the response in the hydraulic head gradient, ΔH to a change in the freshwater velocity q_s. The hydraulic head is determined by fitting a linear regression to the data points and determining the slope, m.

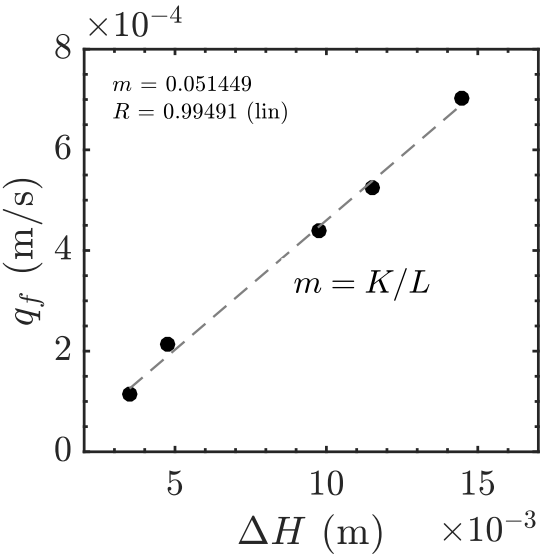

FIGURE 7.B.2: Determination of hydraulic conductivity over several hydraulic heads using Darcy's Law

.

Figure 7.B.3a and b shows the fitted longitudinal and transverse profiles to the 2D numeric simulations performed using COMSOL Multiphysics®. The simulations

were performed using the pre-determined hydraulic conductivity (K = 2 x 10^{-2}) and porosity (ϕ = 0.47) in a rectangular domain using the dimensions of the sand tank. We follow the evolution of a point source tracer that has an initial radius of 15 mm , as determined from the experimental images at t = 0. The transverse and longitudinal dispersivites are determined by carrying out a parametric study over a range of dispersivity values until a best fitting solution was found.

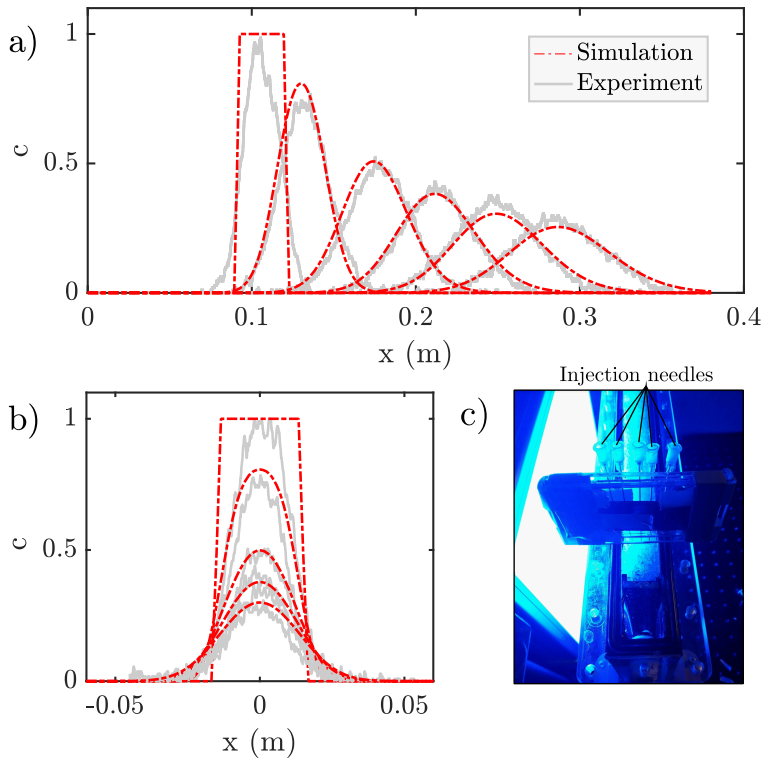

FIGURE 7.B.3: a) Longitudinal concentration profile and b) transverse concentration profile of injected solute slug in the experiment (grey lines) and simulations (dashed red line). c) Top view of injection set up into the tank.

CHAPTER 8

Conclusions

This chapter concludes the thesis by summarizing the main results. A general summary is provided where we recall the key message and findings in each chapter of the thesis. Finally, we provide an outlook on future research challenges that we believe are of significant interest.

8.1 Summary and general conclusions

This thesis focuses on understanding processes that influence the mixing of salt and freshwater and how it can lead to localized chemical reaction hotspots. We have focused on the role of non-uniform flow resulting from variable density flow and its capacity to enhance mixing and mixing-dependent reactions. In the following, we summarize the studies undertaken and main conclusions obtained.

The formation of karsts in many coastal carbonate aquifers have long been attributed to the mixing between salt and freshwater. Numerical studies have previously highlighted the non-trivial interplay between chemical reactions and transport which for homogeneous media, leads to dissolution hotspots at the toe and head of the mixing interface. In reality, the topology of karst networks are complex and cannot adequately be represented using homogeneous media alone. While simulations were only performed under steady state, the results shed light into the propagation of karst conduits, which are well-known to initiate along rock sequences and local heterogeneity. Knowledge of geological heterogeneity is therefore a crucial component towards understanding the temporal evolution of calcite dissolution. Using different types of heterogeneities, ranging from multi-Guassian fields with different levels of connectivity to stratified hydraulic fields, we show that the distribution and characteristics of localized reactive hotspots can be strongly altered. Heterogeneity not only broadens the spectrum of high local reactions rates, but the resulting reactive patterns are strongly dependent on the heterogeneity structure. This was most notable for stratified hydraulic fields, which resulted in elongated strips of enhanced reactivity. This highlighted the role of the convection cell which forces flow upward, thus compressing the interface between stratified layers thereby increasing reaction rates along them.

To better comprehend the influence of mixing due to variable density flow, we evaluate the salt-freshwater mixing interface in the absence of heterogeneity. We find that strong compression near the outlet leads to stronger mixing rates which may also explain strong geochemical activity associated with this zone. Traditionally, the evaluation of mixing in the context of seawater intrusion has involved averaging the mixing width over a segment of the interface. While this is an important metric for risk management for saline contamination, it does not help in distinguishing

local mixing dynamics. To address this gap in knowledge, we look at mixing metrics, including the mixing width, concentration gradient and scalar dissipation rate locally along the entire interface. We study these metrics for several interface positions, dictated by varying the freshwater flux. Beginning at the toe, the interface is found to initially grow due to transverse dispersion and is then arrested by strongly accelerating flow towards the outlet, thereby re-compressing the interface. We derive approximate analytical solutions that describe the compression of the interface using a modified sharp interface analytical solution. These analytical solutions were found to be in good agreement with the results from the numerical solutions

We complement the aforementioned numerical studies with laboratory scale experiments of variable density flow and reactive mixing. Reactive transport experiments aimed at measuring the impact of mixing-limited reactions in porous media is a challenging task. To date, there have been no experiments that dedicated to study reactive mixing under variable density flow. We propose the use of luminol chemiluminescence as a means to capture reaction rates that develop across the salt-freshwater interface. This reaction mechanism proved to have favourable reaction kinetics, which are appropriate for the study of fast mixing-limited reactions. Compared to the Peroxyoxalate reaction used by de Anna et al. (2013b), luminol chemiluminescence not only requires less harmful and toxic compounds, but also uses water as the solvent. This reduces experimental costs and allows experiments to be performed at much larger scales.

The luminol chemiluminescent reaction is used in two separate experimental set-ups. In the first, we investigate mixing and reaction enhancement at a stagnation point within a millifluidic cell using both a flat plate (Hele-Shaw) and porous media. The stagnation point is generated by imposing a Rankine half body flow configuration. Results were found to show good agreement with theoretically derived scaling laws describing the reaction maximum and reactive width as a function of the Pèclet number. Experiments performed in the porous media showed higher reaction rates and smaller reaction widths compared to the Hele-Shaw set-up, which is attributed to greater compression rates resulting from flow focusing between grains. This study not only highlights reaction enhancement due mixing across stagnation points, but also validates the applicability of luminol chemiluminescence to study mixing-limited reactions.

In the second experimental set-up we employ the same reaction to study the influence of mixing on reactions across the salt-freshwater interface for several steady state configurations dictated by the freshwater head. We outline the methodology used in order to employ said reaction in the sand tank filled with fluorinated ethylene propylene grains. While the grains used in the experiment were found to have non-optimal characteristics (not perfectly translucent or optically indexed matched to the fluids), we were able to consistently capture local reactive hotspots at both the toe and head of the interface. The position of these hotspots were in line with those found for mixing-driven calcite dissolution and zones of enhanced strain rates found in steady state homogeneous numerical simulations.

Although enhanced reactivity at the toe is attributed to stagnation point flow, we find that the reactive behaviour did not follow the expected theoretical scaling laws for diffusive mixing as found in the millifluidic cell. We attribute these differences to changes in the interface angle and pore-scale effects which may result in strong deviations away from ideal mixing behaviours. As we move away from the toe, the reaction rate initially decays due to transverse mixing and then proceeds to increase again towards the top of the interface. This is linked to accelerating flow towards the discharge zone, which enhances local stretching rates.

Results from the transient images suggest that reactive mixing is strongly sensitive to the internal structure of flow in the fresh and salt water bodies. During an advance, the reactive interface was found to behave similar to when at steady state. During both these scenarios, we have opposing flow between salt and freshwater bodies, leading to a stagnation point at the toe and the presence of a convection cell. During a retreat, however, the flow field becomes unidirectional, with vectors pointing toward the saltwater boundary. This presumably results in enhanced longitudinal mixing, thereby widening the reactive mixing width. Despite unidirectional flow during the retreat we still have a reactive hotspot at the toe. This is ascribed to differential velocities between the fresh and salt water bodies that continues to result in enhanced compression at the toe. Finally, we also witnessed the appearance of a reactive pulse that travelled up along the interface after a drop in the freshwater head. This may be linked to differential stretching of the interface as it intrudes forward. We show that the use of chemiluminescence in due to mixing in variable-density flows can offer rich and novel behaviours that would otherwise be difficult to observe using conservative tracers alone.

8.2 Outlook

To further our understanding of reactive mixing in coastal environments, future work could benefit from exploring the following topics:

1. to consider the influence of mixing on more complex geochemical reactions occurring across the salt-freshwater interface. Understanding the role of mixing enhanced reactions on regulating the loading of harmful nutrients and pollutants into the ocean would also help evaluate the risks to shallow ocean ecosystems.

2. Implementing the proposed experimental set up to investigate the role of realistic heterogeneities such as stratified aquifers. This would highlight the role of large scale heterogeneities in the creation of local reaction hotspots which may provide insight into the development of areas preferential dissolution.

3. To study the impact of flow deformation on mixing across the upper saline plume in the intertidal zone. While this area has extensively been studied in the field and numerically it lacks any in-depth study related to mixing dynamics.

4. To develop an experimental methodology to investigate precipitation and dissolution reactions across the salt-freshwater interface. This could range from inducing calcite dissolution to assess the formation of karsts and caves along the mixing zone or the precipitation of iron oxides that have been shown to preferentially precipitate out near the outlet of beach environments.

Bibliography

Abarca, Elena (2006). "Seawater intrusion through heterogeneous aquifers". PhD thesis. Universitat Politècnica de Catalunya.

Abarca, Elena and T Prabhakar Clement (2009). "A novel approach for characterizing the mixing zone of a saltwater wedge". In: *Geophysical Research Letters* 36.January, pp. 1–5. DOI: 10.1029/2008GL036995.

Abarca, Elena et al. (2007). "Anisotropic dispersive Henry problem". In: *Advances in Water Resources* 30.4, pp. 913–926. ISSN: 03091708. DOI: 10.1016/j.advwatres.2006.08.005.

Abarca, Elena et al. (2013). "Transient groundwater dynamics in a coastal aquifer : The effects of tides , the lunar cycle , and the beach profile". In: *Water Resources Research* 49.May, pp. 2473–2488. DOI: 10.1002/wrcr.20075.

Abarca Cameo, Elena (2006). "Seawater intrusion in complex geological environments". PhD thesis. Technical University of Catalonia, UPC.

Abdoulhalik, Antoifi (2017). "Experimental and numerical study The use of subsurface physical barriers to control seawater intrusion in heterogeneous coastal aquifers : Experimental and Numerical study A thesis submitted to Queen ' s University Belfast By Antoifi Abdoulhalik in partia". PhD thesis. Queen's University Belfast.

Abdoulhalik, Antoifi and Ashraf A Ahmed (2018). "Transience of seawater intrusion and retreat in response to incremental water - level variations". In: *Hydrological Processes* 32.April 2017, pp. 2721–2733. DOI: 10.1002/hyp.13214.

Acharya, Ram C. et al. (2007). "Pore-scale simulation of dispersion and reaction along a transverse mixing zone in two-dimensional porous media". In: *Water Resources Research* 43.10, pp. 1–11. ISSN: 00431397. DOI: 10.1029/2007WR005969.

Alencar, Natália M.P. de et al. (2020). "Circles of coastal sustainability: A framework for coastal management". In: *Sustainability (Switzerland)* 12.12, pp. 1–27. ISSN: 20711050. DOI: 10.3390/SU12124886.

Amato, Daniel W. et al. (2016). "Impact of submarine groundwater discharge on marine water quality and reef biota of Maui". In: *PLoS ONE* 11.11, pp. 1–28. ISSN: 19326203. DOI: 10.1371/journal.pone.0165825.

Anwar, N., C. Robinson, and D. A. Barry (2014). "Influence of tides and waves on the fate of nutrients in a nearshore aquifer: Numerical simulations". In: *Advances in Water Resources* 73, pp. 203–213. ISSN: 03091708. DOI: 10.1016/j.advwatres.2014.08.015. URL: http://dx.doi.org/10.1016/j.advwatres.2014.08.015.

Ataie-Ashtiani, B., R. E. Volker, and D. A. Lockington (1999). "Tidal effects on sea water intrusion in unconfined aquifers". In: *Journal of Hydrology* 216.1-2, pp. 17–31. ISSN: 00221694. DOI: 10.1016/S0022-1694(98)00275-3.

Audra, Ph. and Arthur Palmer (2015). "Research frontiers in speleogenesis . Dominant processes , hydrogeological conditions and resulting cave patterns". In: *Acta Carsologica* 44.3, pp. 315–348. DOI: 10.3986/ac.v44i3.1960.

Back, William et al. (1979). "Geochemical significance of groundwater discharge and carbonate solution to the formation of Caleta Xel Ha, Quintana Roo, Mexico".

In: *Water Resources Research* 15.6, pp. 1521–1535. ISSN: 19447973. DOI: 10.1029/WR015i006p01521.

Back, William et al. (1986a). "Differential dissolution of a Pleistocene reef in the ground-water mixing zone of coastal Yucatan , Mexico". In: February, pp. 137–140.

— (1986b). "Differential dissolution of a Pleistocene reef in the ground-water mixing zone of coastal Yucatan , Mexico". In: *Geology* 14.February, pp. 137–140.

Badaruddin, Sugiarto, Adrian D. Werner, and Leanne K. Morgan (2015). "Water table salinization due to seawater intrusion". In: *Water Resources Research* 51.10, pp. 8397–8408. ISSN: 19447973. DOI: 10.1002/2015WR017098. arXiv: 2014WR016527 [10.1002].

Bai, Kunlun and Joseph Katz (2014). "On the refractive index of sodium iodide solutions for index matching in PIV". In: *Experiments in Fluids* 55.4. ISSN: 07234864. DOI: 10.1007/s00348-014-1704-x.

Bandopadhyay, Aditya et al. (2017). "Enhanced reaction kinetics and reactive mixing scale dynamics in mixing fronts under shear flow for arbitrary Damköhler numbers". In: *Advances in Water Resources* 100, pp. 1339–1351. ISSN: 03091708. DOI: 10.1016/j.advwatres.2016.12.008. arXiv: 1604.08092.

Bandopadhyay, Aditya, Philippe Davy, and Tanguy Le Borgne (2018). "Shear Flows Accelerate Mixing Dynamics in Hyporheic Zones and Hillslopes". In: *Geophysical Research Letters*, pp. 659–668. DOI: 10.1029/2018GL079914.

Barlow, Paul M (2003). *Ground Water in Freshwater-Saltwater Environments of the Atlantic Coast*. Tech. rep. Geological Survey (USGS), p. 113.

Batchelor, G. K. (1959). "Small-scale variation of convected quantities like temperature in turbulent fluid: Part 1. General discussion and the case of small conductivity". In: *Journal of Fluid Mechanics* 5.1, pp. 113–133. ISSN: 14697645. DOI: 10.1017/S002211205900009X.

Bear, Jacob (1988). *Dynamics of fluids in porous media*. Dover publications, inc New York.

Blum, Loïc j. (1997). *Bio- and Chemi-Luminescent Sensors*. World Scientific.

Bolster, Diogo et al. (2011). "Mixing in confined stratified aquifers". In: *Journal of Contaminant Hydrology* 120-121.C, pp. 198–212. ISSN: 01697722. DOI: 10.1016/j.jconhyd.2010.02.003.

Bone, Sharon E., M.E. Gonneea, and Matthew A. Charette (2006). "Geochemical cycling of arsenic in a coastal aquifer". In: *Environmental Science and Technology*, pp. 3273–3278.

Burdo, Timothy G and W Rudolf Seitz (1975). "Mechanism of Cobalt Catalysis of Luminol Chemiluminescence UVnh". In: *Analytical Chemistry* 47.9, pp. 1639–1643. DOI: 10.1021/ac60359a019.

Bustos, Carlos, Guillermo Salgado, and Cecilia López (2001). "The Oxidation of Luminol an Experiment to Maximize the Efficiency of Chemiluminescence from Luminol". In: *The Chemical Educator* 2.01, pp. 97–99.

Cartwright, Nick, Peter Nielsen, and Scott Dunn (2003). "Water table waves in an unconfined aquifer : Experiments and modeling". In: *Water Resources Research* 39.12, pp. 1–12. DOI: 10.1029/2003WR002185.

Castro-alcalá, Eduardo (2019). "Laboratory experiments to evaluate the joint effect between heterogeneity and head fluctuation on mixing, effective porosity and tailing". PhD thesis. Universitat Politechnica De Catalunya.

Castro-Alcalá, Eduardo et al. (2012). "Visualization of mixing processes in a heterogeneous sand box aquifer". In: *Environmental Science and Technology* 46.6, pp. 3228–3235. ISSN: 0013936X. DOI: 10.1021/es201779p.

Chang, Sun Woo and T. Prabhakar Clement (2012a). "Experimental and numerical investigation of saltwater intrusion dynamics in flux-controlled groundwater systems". In: *Water Resources Research* 48.9, pp. 1–10. ISSN: 00431397. DOI: 10.1029/2012WR012134.

Chang, Sun Woo and T Prabhakar Clement (2012b). "Experimental and numerical investigation of saltwater intrusion dynamics in flux-controlled groundwater systems". In: 48.September, pp. 1–10. DOI: 10.1029/2012WR012134.

Chang, Sun Woo and T. Prabhakar Clement (2013). "Laboratory and numerical investigation of transport processes occurring above and within a saltwater wedge". In: *Journal of Contaminant Hydrology* 147, pp. 14–24. ISSN: 01697722. DOI: 10.1016/j.jconhyd.2013.02.005. URL: http://dx.doi.org/10.1016/j.jconhyd.2013.02.005.

Charbonnier, Céline et al. (2013). "Aerobic respiration in a high-energy sandy beach". In: *Marine Chemistry* 155, pp. 10–21. ISSN: 03044203. DOI: 10.1016/j.marchem.2013.05.003. URL: http://dx.doi.org/10.1016/j.marchem.2013.05.003.

Charette, Matthew A. and Edward R. Sholkovitz (2002). "Oxidative precipitation of groundwater-derived ferrous iron in the subterranean estuary of a coastal bay". In: *Geophysical Research Letters* 29.10, pp. 85–1–85–4. ISSN: 0094-8276. DOI: 10.1029/2001gl014512.

Chiogna, Gabriele et al. (2010). "Evidence of compound-dependent hydrodynamic and mechanical transverse dispersion by multitracer laboratory experiments". In: *Environmental Science and Technology* 44.2, pp. 688–693. ISSN: 0013936X. DOI: 10.1021/es9023964.

Collaudin, Agnès Berger and Loïc J. Blum (1997). "Investigations of the enhancer effect of a high-salt concentration medium on the luminol chemiluminescent reaction". In: *Photochemistry and Photobiology* 65.2, pp. 303–308. ISSN: 00318655. DOI: 10.1111/j.1751-1097.1997.tb08562.x.

Cooper, H H (1959). "A Hypothesis Concerning the Dynamic Balance of Fresh Water and Salt Water in a Coastal Aquifer". In: *Journal of Geophysical Research* 64.4, pp. 461–467.

Dagan, G (1987). "Theory of solute transport by groundwater". In: *Annu. Rev. Fluid Mech.* 19.1, pp. 183–213. ISSN: 00664189. DOI: 10.1146/annurev.fluid.19.1.183.

de Anna, Pietro (2013). "Mixing and reactions in porous media". PhD thesis. Rennes University 1. ISBN: 1234524678479.

de Anna, Pietro et al. (2013a). "Flow intermittency, dispersion, and correlated continuous time random walks in porous media". In: *Physical Review Letters* 110.18, pp. 1–5. ISSN: 00319007. DOI: 10.1103/PhysRevLett.110.184502.

de Anna, Pietro et al. (2013b). "Mixing and Reaction Kinetics in Porous Media : An Experimental Pore Scale Quantification". In: *Environmental Science and Technology*.

de Anna, Pietro et al. (2014). "The filamentary structure of mixing fronts and its control on reaction kinetics in porous media flows". In: *Geophysical Research Letters* May, pp. 4586–4593. DOI: 10.1002/2014GL060068.Abstract.

De Barros, Felipe P J et al. (2012). "Flow topology and scalar mixing in spatially heterogeneous flow fields". In: *Geophysical Research Letters* 39.8, pp. 1–5. ISSN: 00948276. DOI: 10.1029/2012GL051302.

De Simoni, M. (2005). "A procedure for the solution of multicomponent reactive transport problems". In: 41, pp. 1–16. DOI: 10.1029/2005WR004056.

De Simoni, M., J Carrera, and M W Saaltink (2007). "A mixing ratios-based formulation for multicomponent reactive transport". In: *Water Resources Research* 43, pp. 1–10. DOI: 10.1029/2006WR005256.

De Vriendt, K., M. Pool, and M. Dentz (2020). "Heterogeneity-Induced Mixing and Reaction Hot Spots Facilitate Karst Propagation in Coastal Aquifers". In: *Geophysical Research Letters* 47.10, pp. 1–12. ISSN: 19448007. DOI: 10.1029/2020GL087529.

Dell'Oca, Aronne et al. (2018). "Solute dispersion for stable density-driven flow in randomly heterogeneous porous media". In: *Advances in Water Resources* 111.April 2017, pp. 329–345. ISSN: 03091708. DOI: 10.1016/j.advwatres.2017.10.040. URL: https://doi.org/10.1016/j.advwatres.2017.10.040.

Dentz, M. et al. (2006). "Variable-density flow in porous media". In: *Journal of Fluid Mechanics* 561, pp. 209–235. ISSN: 00221120. DOI: 10.1017/S0022112006000668.

Dentz, Marco et al. (2011). "Mixing , spreading and reaction in heterogeneous media : A brief review". In: *Journal of Contaminant Hydrology* 120-121, pp. 1–17. ISSN: 0169-7722. DOI: 10.1016/j.jconhyd.2010.05.002. URL: http://dx.doi.org/10.1016/j.jconhyd.2010.05.002.

Dever, Joyce A. et al. (2001). "Simulated space vacuum ultraviolet (VUV) exposure testing for polymer films". In: *39th Aerospace Sciences Meeting and Exhibit* February. DOI: 10.2514/6.2001-1054.

Dodeigne, C, L Thunus, and R Lejeune (2000). "Chemiluminescence as diagnostic tool . A review". In: *Talanta* 51, pp. 415–439.

Dwivedi, Dipankar et al. (2000). "Water Resources Research: Preface". In: *Water Resources Research* 36.1, pp. 11–12. ISSN: 00431397. DOI: 10.1029/1999WR900293.

Eeman, S. et al. (2011). "Analysis of the thickness of a fresh water lens and of the transition zone between this lens and upwelling saline water". In: *Advances in Water Resources* 34.2, pp. 291–302. ISSN: 03091708. DOI: 10.1016/j.advwatres.2010.12.001. URL: http://dx.doi.org/10.1016/j.advwatres.2010.12.001.

Engdahl, Nicholas B, Timothy R Ginn, and Graham E Fogg (2013). "Scalar dissipation rates in non-conservative transport systems". In: *Journal of Contaminant Hydrology* 149, pp. 46–60. ISSN: 0169-7722. DOI: 10.1016/j.jconhyd.2013.03.003. URL: http://dx.doi.org/10.1016/j.jconhyd.2013.03.003.

Engdahl, Nicholas B, David A Benson, and Diogo Bolster (2014). "Predicting the enhancement of mixing-driven reactions in nonuniform flows using measures of flow topology". In: *Physical Review E* 051001, pp. 1–5. DOI: 10.1103/PhysRevE.90.051001.

Etsias, Georgios et al. (2020). "Optimizing Laboratory Investigations of Saline Intrusion by Incorporating Machine Learning Techniques". In: *water*.

Ferguson, Grant and Tom Gleeson (2012). "Vulnerability of coastal aquifers to groundwater use and climate change". In: *Nature Climate Change* 2.5, pp. 342–345. ISSN: 1758678X. DOI: 10.1038/nclimate1413. URL: http://dx.doi.org/10.1038/nclimate1413.

Filipponi, Marco, Pierre-yves Jeannin, and Laurent Tacher (2009). "Geomorphology Evidence of inception horizons in karst conduit networks". In: *Geomorphology* 106.1-2, pp. 86–99. ISSN: 0169-555X. DOI: 10.1016/j.geomorph.2008.09.010. URL: http://dx.doi.org/10.1016/j.geomorph.2008.09.010.

Fiori, Aldo and Gedeon Dagan (1999). "Concentration fluctuations in transport by groundwater : Comparison between theory and field experiments". In: *Water Resources Research* 35.January, pp. 105–112. DOI: 10.1029/98WR01862.

Gabrov, Franci, Philipp Häuselmann, and Philippe Audra (2014). "'Looping caves' versus 'water table caves': The role of base-level changes and recharge variations in cave development". In: *Geomorphology* 204, pp. 683–691. DOI: 10.1016/j.geomorph.2013.09.016.

Galfi, L and Z Racz (1988). "Properties of the reaction front in an A+8 = C type reactionit'usion process". In: *Physical Review A* 38.6, pp. 8–11.

Gelhar, L. W. (2003). *Applied Stochastic Hydrogeology*. Oxford University Press. ISBN: 019513804X.

Gelhar, L. W. (1993). (1993). *Stochastic subsurface hydrology*. Prentice-Hall.

Geng, Xiaolong et al. (2020). "Heterogeneity Affects Intertidal Flow Topology in Coastal Beach Aquifers". In: *Geophysical Research Letters* 47.17, pp. 1–12. ISSN: 19448007. DOI: 10.1029/2020GL089612.

Glover, R. E. (1959). "The pattern of fresh-water flow in a coastal aquifer". In: *Journal of Geophysical Research* 64.4, pp. 457–459. DOI: 10.1029/jz064i004p00457.

Goswami, Rohit R. and T. Prabhakar Clement (2007). "Laboratory-scale investigation of saltwater intrusion dynamics". In: *Water Resources Research* 43.4, pp. 1–11. ISSN: 00431397. DOI: 10.1029/2006WR005151.

Gramling, Carolyn M., Charles F. Harvey, and Lucy C. Meigs (2002). "Reactive transport in porous media: A comparison of model prediction with laboratory visualization". In: *Environmental Science and Technology* 36.11, pp. 2508–2514. ISSN: 0013936X. DOI: 10.1021/es0157144.

Grane, F. E. and G. H.F. Gardner (1961). "Measurements of Transverse Dispersion in Granular Media". In: *Journal of Chemical and Engineering Data* 6.2, pp. 283–287. ISSN: 15205134. DOI: 10.1021/je60010a031.

Groves, Christopher G. and Alan.D Howard (1994). "Early development of karst systems . I . Preferential flow path enlargement under laminar flow". In: *Water Resour. Res* 30.October, pp. 2837–2846. DOI: 10.1029/94WR01303.

Hassan, Yassin A and E.E Dominguez-Ontiveros (2008). "Flow visualization in a pebble bed reactor experiment using PIV and refractive index matching techniques". In: *Nuclear Engineering and Design* 238, pp. 3080–3085. DOI: 10.1016/j.nucengdes.2008.01.027.

Heiss, James W. and Holly A. Michael (2014). "This Copy of a Work Protected By Canadian Copyright Law Is To". In: *Water Resources Research*, pp. 6747–6766. DOI: 10.1002/2014WR015574.Received.

Heiss, James W. et al. (2017). "Physical Controls on Biogeochemical Processes in Intertidal Zones of Beach Aquifers". In: *Water Resources Research* 53.11, pp. 9225–9244. ISSN: 19447973. DOI: 10.1002/2017WR021110.

Held, R, S Attinger, and W Kinzelbach (2005). "Homogenization and effective parameters for the Henry problem in heterogeneous formations". In: *Water Resources Research* 41, pp. 1–14. DOI: 10.1029/2004WR003674.

Hester, E. T., K. I. Young, and M. A. Widdowson (2013). "Mixing of surface and groundwater induced by riverbed dunes: Implications for hyporheic zone definitions and pollutant reactions". In: *Water Resources Research* 49.9, pp. 5221–5237. ISSN: 00431397. DOI: 10.1002/wrcr.20399.

Heyman, Joris et al. (2020). "Stretching and folding sustain microscale chemical gradients in porous media". In: *Proceedings of the National Academy of Sciences of the United States of America* 117.24, pp. 13359–13365. DOI: 10.1073/pnas.2002858117.

Hidalgo, Juan J and Marco Dentz (2018). "Mixing across fluid interfaces compressed by convective flow in porous media". In: *Journal of Fluid Mechanics*, pp. 105–128. DOI: 10.1017/jfm.2017.888.

Hidalgo, Juan J et al. (2015). "Dissolution patterns and mixing dynamics in unstable reactive flow". In: *Geophysical Research Letters* 42.15, pp. 6357–6364. DOI: 10.1002/2015GL065036.1..

Holzbecher, Ekkehard (1998). *Modeling density-driven flow in porous media: principles, numerics, software*. Springer Science Business Media. ISBN: 9783642637193.

Horkay, Ferenc, Ichiji Tasaki, and Peter J Basser (2000). "Osmotic Swelling of Polyacrylate Hydrogels in Physiological Salt Solutions". In: *Biomacromolecules*, pp. 84–90.

Houben, Georg J. et al. (2018). "The influence of heterogeneity on coastal groundwater flow - physical and numerical modeling of fringing reefs, dykes and structured conductivity fields". In: *Advances in Water Resources* 113, pp. 155–166. ISSN: 03091708. DOI: 10.1016/j.advwatres.2017.11.024. URL: https://doi.org/10.1016/j.advwatres.2017.11.024.

Hun, Bok Jung, Matthew A. Charette, and Yan Zheng (2009). "Field, laboratory, and modeling study of reactive transport of groundwater arsenic in a coastal aquifer". In: *Environmental Science and Technology* 43.14, pp. 5333–5338. ISSN: 0013936X. DOI: 10.1021/es900080q.

Inouchi, Kunimitsu, Kishi Yosuke, and Kakinuma Tadao (1990). "The motion of coastal groundwater in response to the tide". In: *Journal of Hydrology* 115, pp. 165–191.

Izumoto, Satoshi (2021). "Spectral induced polarization of calcite precipitation in porous media". PhD thesis. University of Stuttgart.

Izumoto, Satoshi et al. (2021). "Enhancement of mixing-induced reactions at stagnation points in pore scale flow fields". In: *Unpublished*.

Jevrejeva, Svetlana et al. (2016). "Coastal sea level rise with warming above 2 C". In: *Proceedings of the National Academy of Sciences of the United States of America* 113.47, pp. 13342–13347. ISSN: 10916490. DOI: 10.1073/pnas.1605312113.

Jiao, Jimmy and Vincent Post (2019). "Analytical Solutions for a Steady Freshwater–Saltwater Interface". In: *Coastal Hydrogeology*, pp. 47–72. DOI: 10.1017/9781139344142.003.

Jiménez-Martínez, Joaquín et al. (2017). "Impact of saturation on dispersion and mixing in porous media: Photobleaching pulse injection experiments and shear-enhanced mixing model". In: *Water Resources Research*, pp. 1457–1472. DOI: 10.1002/2016WR019849.Received.

Jones, B. F. et al. (1999). *Geochemical investigations. In Seawater intrusion in coastal aquifers—concepts, methods and practices*. Dordrecht: Springer, pp. 51–71.

Jonsson, Tobias and Knut Irgum (1999). "Very fast peroxyoxalate chemiluminescence". In: *Analytica Chmica Acta* 400.August, pp. 257–264.

Jose, Surabhin C. and Olaf A. Cirpka (2004). "Measurement of Mixing-Controlled Reactive Transport in Homogeneous Porous Media and Its Prediction from Conservative Tracer Test Data". In: *Environmental Science and Technology* 38.7, pp. 2089–2096. ISSN: 0013936X. DOI: 10.1021/es034586b.

Jouves, Johan et al. (2017). "Speleogenesis , geometry , and topology of caves : A quantitative study of 3D karst conduits Geomorphology Speleogenesis , geometry , and topology of caves : A quantitative study of 3D karst conduits". In: *Geomorp* 298.January, pp. 86–106. DOI: 10.1016/j.geomorph.2017.09.019.

Kang, Peter K. et al. (2014). "Pore-Scale intermittent velocity structure underpinning anomalous transport through 3-D porousmedia". In: *Geophysical Research Letters* 41.17, pp. 6184–6190. ISSN: 19448007. DOI: 10.1002/2014GL061475.

Kapoor, Vivek and Peter K Kitanidis (1998). "Concentration fluctuations and dilution in aquifers". In: *Water Resources Research* 34.5, pp. 1181–1193.

Kerrou, Jaouher and Philippe Renard (2010). "A numerical analysis of dimensionality and heterogeneity effects on advective dispersive seawater intrusion processes". In: *Hydrogeology Journal* 18.1, pp. 55–72. ISSN: 14312174. DOI: 10.1007/s10040-009-0533-0.

Kim, Kue-young, Chul-min Chon, and Ki-hwa Park (2007). "A Simple Method for Locating the Fresh Water – Salt Water Interface Using Pressure Data". In: *Ground Water* 45.6, pp. 723–728. DOI: 10.1111/j.1745-6584.2007.00349.x.

Kim, Kyra H. et al. (2017). "Spatial Patterns of Groundwater Biogeochemical Reactivity in an Intertidal Beach Aquifer". In: *Journal of Geophysical Research: Biogeosciences* 122.10, pp. 2548–2562. ISSN: 21698961. DOI: 10.1002/2017JG003943.

Kim, Kyung Min et al. (2013). "A chelate complex-enhanced luminol system for selective determination of Co(II), Fe(II) and Cr(III)". In: *Luminescence* 28.3, pp. 372–377. ISSN: 15227235. DOI: 10.1002/bio.2392.

Kitanidis, Peter K. (2005). "The concept of the dilution index Peter". In: *Water Resources Research* 30.June, pp. 1–10.

Klenk, I. D. and P. Grathwohl (2002). "Transverse vertical dispersion in groundwater and the capillary fringe". In: *Journal of Contaminant Hydrology* 58.1-2, pp. 111–128. ISSN: 01697722. DOI: 10.1016/S0169-7722(02)00011-6.

Klopf, Lori L and Timothy A Nieman (1983). "Iron(II), Cobalt(II), Copper(II)," in: *Analytical Chemistry* 55.7, pp. 1080–1083. DOI: 10.1021/ac00258a023.

Konz, M. et al. (2008). "On the measurement of solute concentrations in 2-D flow tank experiments". In: *Hydrology and Earth System Sciences* 12.3, pp. 727–738. ISSN: 16077938. DOI: 10.5194/hess-12-727-2008.

Kreyns, Pieter, Xiaolong Geng, and Holly A. Michael (2020). "The Influence of Connected Heterogeneity on Groundwater Flow and Salinity Distributions in Coastal Volcanic Aquifers". In: *Journal of Hydrology* 586.September 2019, p. 124863. ISSN: 00221694. DOI: 10.1016/j.jhydrol.2020.124863.

Kroeger, K. D. and M. A. Charette (2008). "Nitrogen biogeochemistry of submarine groundwater discharge". In: *Limnology and Oceanography* 53.3, pp. 1025–1039. ISSN: 00243590. DOI: 10.4319/lo.2008.53.3.1025.

Kuan, Woei Keong et al. (2012). "Tidal influence on seawater intrusion in unconfined coastal aquifers". In: *Water Resources Research* 48.2, pp. 1–11. ISSN: 00431397. DOI: 10.1029/2011WR010678.

Langevin, Christian D (2003). "Simulation of Submarine Ground Water Discharge to a Marine Estuary : Biscayne Bay , Florida". In: *Ground Water* 41.6, pp. 758–771.

LaRoche, J. et al. (1997). "Brown Tide blooms in Long Island ' s coastal waters linked to interannual variability in groundwater flow". In: *Global Change Biology* 3.5, pp. 397–410.

Larralde, Hernan et al. (1992). "Reaction front for A+ H: C diffusion-reaction systems with initially separated reactants". In: *Physical Review A* 46.2, pp. 855–859.

Larralde, Hernan et al. (1992). "Reaction front for A+ H: C diffusion-reaction systems with initially separated reactants". In: *Physical Review A* 46.2, pp. 855–859.

Le Borgne, Tanguy et al. (2010). "Non-Fickian mixing : temporal evolution of the scalar dissipation rate in porous media". In: *Advances in Water Resources*. ISSN: 0309-1708. DOI: 10.1016/j.advwatres.2010.08.006. URL: http://dx.doi.org/10.1016/j.advwatres.2010.08.006.

Le Borgne, Tanguy, Marco Dentz, and Emmanuel Villermaux (2013). "Stretching, coalescence, and mixing in porous media". In: *Physical Review Letters* 110.20, pp. 1–5. ISSN: 00319007. DOI: 10.1103/PhysRevLett.110.204501.

Le Borgne, Tanguy, Timothy R. Ginn, and Marco Dentz (2014). "Impact of fluid deformation on mixing-induced chemical reactions in heterogeneous flows". In: *Geophysical Research Letters* 41.22, pp. 7898–7906. ISSN: 19448007. DOI: 10.1002/2014GL062038.

Le Borgne, Tanguy, M Dentz, and E Villermaux (2015). "The lamellar description of mixing in porous media". In: *Journal of Fluid Mechanics* 770, pp. 458–498. DOI: 10.1017/jfm.2015.117.

Lee, Yong Woo and Guebuem Kim (2007). "Linking groundwater-borne nutrients and dinoflagellate red-tide outbreaks in the southern sea of Korea using a Ra tracer". In: *Estuarine, Coastal and Shelf Science* 71.1-2, pp. 309–317. ISSN: 02727714. DOI: 10.1016/j.ecss.2006.08.004.

Lester, D. R., M. G. Trefry, and G. Metcalfe (2016). "Chaotic advection at the pore scale: Mechanisms, upscaling and implications for macroscopic transport". In: *Advances in Water Resources* 97, pp. 175–192. ISSN: 03091708. DOI: 10.1016/j.advwatres.2016.09.007. arXiv: 1602.05275. URL: http://dx.doi.org/10.1016/j.advwatres.2016.09.007.

Liu, Yi et al. (2014). "Influence of a coarse interlayer on seawater intrusion and contaminant migration in coastal aquifers". In: *Hydrological Processes* 28.20, pp. 5162–5175. ISSN: 10991085. DOI: 10.1002/hyp.10002.

Liu, Yi et al. (2017). "Tidal Pumping-Induced Nutrients Dynamics and Biogeochemical Implications in an Intertidal Aquifer". In: *Journal of Geophysical Research: Biogeosciences* 122.12, pp. 3322–3342. ISSN: 21698961. DOI: 10.1002/2017JG004017.

Lowe, David John (1992). "The origin of limestone caverns : an inception horizon hypothesis". PhD thesis. Manchester Polytechnic.

Lu, Chunhiu et al. (2013). "Steady-state freshwater–seawater mixing zone in stratified coastal aquifers". In: *Journal of Hydrology* 9. ISSN: 00221694. DOI: 10.1016/j.jhydrol.2013.09.017. URL: http://www.tandfonline.com/doi/abs/10.1080/18146627.2012.755281.

Lu, Chunhui and Jian Luo (2010). "Dynamics of freshwater-seawater mixing zone development in dual-domain formations". In: *Water Resources Research* 46.11, pp. 1–6. ISSN: 00431397. DOI: 10.1029/2010WR009344.

Lu, Chunhui and Adrian D Werner (2013). "Advances in Water Resources Timescales of seawater intrusion and retreat". In: *Advances in Water Resources* 59, pp. 39–51. ISSN: 0309-1708. DOI: 10.1016/j.advwatres.2013.05.005. URL: http://dx.doi.org/10.1016/j.advwatres.2013.05.005.

Lu, Chunhui, Rulan Gong, and Jian Luo (2009a). "Analysis of stagnation points for a pumping well in recharge areas". In: *Journal of Hydrology* 373.3-4, pp. 442–452. ISSN: 00221694. DOI: 10.1016/j.jhydrol.2009.05.002.

Lu, Chunhui, Peter K Kitanidis, and Jian Luo (2009b). "Effects of kinetic mass transfer and transient flow conditions on widening mixing zones in coastal aquifers". In: *Water Resources Research* 45.December 2008, pp. 1–17. DOI: 10.1029/2008WR007643.

Luyun Jr, Roger et al. (2009a). "Effects of Artificial Recharge and Physical Barrier on Seawater Intrusion". In: *Journal of Hydraulic Engineering, JSCE* 53, pp. 85–90. URL: http://library.jsce.or.jp/jsce/open/00028/2009/53-0015.pdf.

Luyun Jr, Roger, Kazuro Momii, and Kei Nakagawa (2009b). "Laboratory-scale saltwater behavior due to subsurface cutoff wall". In: *Journal of Hydrology* 377.3-4, pp. 227–236. ISSN: 0022-1694. DOI: 10.1016/j.jhydrol.2009.08.019. URL: http://dx.doi.org/10.1016/j.jhydrol.2009.08.019.

Marzadri, Alessandra et al. (2016). "Mixing interfaces, fluxes, residence times and redox conditions of the hyporheic zones induced by dune-like bedforms and ambient groundwater flow". In: *Advances in Water Resources* 88, pp. 139–151. ISSN: 03091708. DOI: 10.1016/j.advwatres.2015.12.014. URL: http://dx.doi.org/10.1016/j.advwatres.2015.12.014.

Masahiro, Takahashi, Kazuro Momii, and Roger Luyun Jr (2018). "Laboratory Scale Investigation of Dispersion Effects on Saltwater Movement due to Curoff Wall Installation". In: *25th Salt Water Intrusion Meeting*. Gdansk, pp. 323–328.

McClain, Michael E. et al. (2003). "Biogeochemical Hot Spots and Hot Moments at the Interface of Terrestrial and Aquatic Ecosystems". In: *Ecosystems* 6.4, pp. 301–312. ISSN: 14329840. DOI: 10.1007/s10021-003-0161-9.

McNeil, J. D., G. A. Oldenborger, and R. A. Schincariol (2006). "Quantitative imaging of contaminant distributions in heterogeneous porous media laboratory experiments". In: *Journal of Contaminant Hydrology* 84.1-2, pp. 36–54. ISSN: 01697722. DOI: 10.1016/j.jconhyd.2005.12.005.

Mendenhall, G.D. (1993). "Analytical applications of chemiluminescence". In: *Advances in Clinical Chemistry* 30.C, pp. 89–183. ISSN: 00652423. DOI: 10.1016/S0065-2423(08)60195-X.

Merenyi, Gabor, Johan Lind, and Trygve E Eriksen (1990). "Lu m i no1 C h e m il u m inescence : Chemistry , Excitation , Emitter". In: 5, pp. 53–56.

Michael, Holly A, Ann E Mulligan, and Charles F Harvey (2005). "Seasonal oscillations in water exchange between aquifers and the coastal ocean". In: *Nature* 436.August, pp. 1145–1148. DOI: 10.1038/nature03935.

Michael, Holly A et al. (2016). "Geologic influence on groundwater salinity drives large seawater circulation through the continental shelf". In: *Geophysical Research Letters*, pp. 782–791. DOI: 10.1002/2016GL070863.Received.

Moore, Willard S. (1999). "The subterranean estuary: A reaction zone of ground water and sea water". In: *Marine Chemistry* 65.1-2, pp. 111–125. ISSN: 03044203. DOI: 10.1016/S0304-4203(99)00014-6.

Moore, Willard S (2010). "A reevaluation of submarine groundwater discharge along the southeastern coast of North America". In: 24.December 2009, pp. 1–9. DOI: 10.1029/2009GB003747.

Mylroie, J. E. and J. L. Carew (1990). "Mylroie, J. E., Carew, J. L. (1990). The flank margin model for dissolution cave development in carbonate platforms. Earth Surface Processes and Landforms, 15(5), 413–424. doi:10.1002/esp.3290150505". In: *Earth Surface Processes and Landforms* 15, pp. 413–424.

Naftaly, Aviv et al. (2015). "Visualization and analysis of nanoparticle transport and ageing in reactive porous media". In: *Journal of Hazardous Materials* 299, pp. 513–519. ISSN: 18733336. DOI: 10.1016/j.jhazmat.2015.07.043. URL: http://dx.doi.org/10.1016/j.jhazmat.2015.07.043.

Neri, Mariene Gutierrez (2009). "Aspects of Transverse Dispersion in Porous Media". In: 309. DOI: 10.1016/j.aquatox.2014.06.022.

Neuman, P (1990). "Universal scaling of hydraulic conductivities and dispersivities in geologic media". In: *Water Resources Research* 26.8, pp. 1749–1758.

Ng, Kwok Choi and Brian Jones (1995). "Hydrogeochemistry of Grand Cayman, British West Indies: implications for carbonate diagenetic studies". In: *Journal of Hydrology* 164.1-4, pp. 193–216. ISSN: 00221694. DOI: 10.1016/0022-1694(94)02556-Q.

Nick, H M et al. (2013). "Reactive dispersive contaminant transport in coastal aquifers : Numerical simulation of a reactive Henry problem". In: *Journal of Contaminant Hydrology* 145, pp. 90–104. ISSN: 0169-7722. DOI: 10.1016/j.jconhyd.2012.12.005. URL: http://dx.doi.org/10.1016/j.jconhyd.2012.12.005.

Oates, Peter M. and Charles F. Harvey (2006). "A colorimetric reaction to quantify fluid mixing". In: *Experiments in Fluids* 41.5, pp. 673–683. ISSN: 07234864. DOI: 10.1007/s00348-006-0184-z.

Okubo, Akira (1970). "Horizontal dispersion of floatable particles in the vicinity of velocity singularities such as convergences". In: *Deep-Sea Research and Oceanographic Abstracts* 17.3, pp. 445–454. ISSN: 00117471. DOI: 10.1016/0011-7471(70)90059-8.

Olsson, Åsa and Peter Grathwohl (2007). "Transverse dispersion of non-reactive tracers in porous media: A new nonlinear relationship to predict dispersion coefficients". In: *Journal of Contaminant Hydrology* 92.3-4, pp. 149–161. ISSN: 01697722. DOI: 10.1016/j.jconhyd.2006.09.008.

Ottino, J M (1989). *The kinematics of mixing : stretching , chaos , and transport*. Cambridge university press.

Oz, Imri et al. (2015). "Saltwater circulation patterns within the freshwater-saltwater interface in coastal aquifers: Laboratory experiments and numerical modeling". In: *Journal of Hydrology* 530, pp. 734–741. ISSN: 00221694. DOI: 10.1016/j.jhydrol.2015.10.033. URL: http://dx.doi.org/10.1016/j.jhydrol.2015.10.033.

Palmer, Arthur (1992). "Origin and morphology of limestone caves". In: *Geological Society of America Bulletin* 103.January 1991, pp. 1–21.

Palmer, R and D Williams (1982). "Cave development under Andros Island, Bahamas." In: *Cave Science* 11.1, pp. 50–52.

Park, Sung Hyun et al. (2001). "Gel-free experiments of reaction-diffusion front kinetics". In: *Physical Review E* 64, pp. 2–5. DOI: 10.1103/PhysRevE.64.055102.

Paster, A (2010). "Mixing between fresh and salt waters at aquifer regional scale and identification of transverse dispersivity". In: *Journal of Hydrology* 380.1-2, pp. 36–44. ISSN: 0022-1694. DOI: 10.1016/j.jhydrol.2009.10.018. URL: http://dx.doi.org/10.1016/j.jhydrol.2009.10.018.

Paster, Amir and Gedeon Dagan (2007). "Mixing at the interface between two fluids in porous media: a boundary-layer solution". In: *Journal of Fluid Mechanics* 584, pp. 455–472. DOI: 10.1017/S0022112007006532.

Paster, Amir, Gedeon Dagan, and Joseph Guttman (2006). "The salt-water body in the Northern part of Yarkon-Taninim aquifer : Field data analysis , conceptual model and prediction". In: *Journal of Hydrology* 323, pp. 154–167. DOI: 10.1016/j.jhydrol.2005.08.018.

Perkins, T.K. and O.C. Johnston (1963). "A Review of Diffusion and Dispersion in Porous Media". In: *Society of Petroleum Engineers Journal* 3.01, pp. 70–84. ISSN: 0197-7520. DOI: 10.2118/480-pa.

Pool, M. et al. (2019a). "Effects of sea level changes and fluid density variability on calcite dissolution in coastal aquifers". In: *Geophysical Research Abstracts* 21.

Pool, Maria (2011). "Simplified approaches to deal with the complexities of Seawater Intrusion". PhD thesis.

Pool, Maria and Marco Dentz (2018). "Effects of heterogeneity , connectivity and density variations on mixing and chemical reactions under temporally fluctuating flow conditions and the formation of reaction patterns". In: *Water Resources Research*, pp. 1–40.

Pool, Maria, Vincent E.A. Post, and Craig T Simmons (2014). "aquifers : Homogeneous case". In: *Water Resources Research*, pp. 6910–6926. DOI: 10.1002/2014WR015534.Received.

Pool, Maria, Vincent E. A. Post, and Craig T. Simmons (2015). "Effects of tidal fluctuations and spatial heterogeneity on mixing and spreading in spatially heterogeneous coastal aquifers". In: pp. 1570–1585. DOI: 10.1002/2014WR016068.Received.

Pool, Maria et al. (2019b). "Effects of sea level changes and fluid density variability on calcite dissolution in coastal aquifers [Conference presentation abstract]". In: *EGU General Assembly*.

Pope, S.B. (2000). *Turbulent flows*. Cambridge, UK: Cambridge university press.

Price, René M. et al. (2003). "Use of tritium and helium to define groundwater flow conditions in Everglades National Park". In: *Water Resources Research* 39.9, pp. 1–12. DOI: 10.1029/2002WR001929.

Prommer, H., D. A. Barry, and G. B. Davis (2002). "Modelling of physical and reactive processes during biodegradation of a hydrocarbon plume under transient groundwater flow conditions". In: *Journal of Contaminant Hydrology* 59.1-2, pp. 113–131. ISSN: 01697722. DOI: 10.1016/S0169-7722(02)00078-5.

Rahman, Md Arifur et al. (2005). "Experiments on vertical transverse mixing in a large-scale heterogeneous model aquifer". In: *Journal of Contaminant Hydrology* 80.3-4, pp. 130–148. ISSN: 01697722. DOI: 10.1016/j.jconhyd.2005.06.010.

Rangel-Medina, M. et al. (2004). "The saline intrusion in the Costa de Hermosillo aquifer in Sonora, México; a challenge to restore". In: *Proceedings of the 18th Salt Water Intrusion Meeting, Cartagena, Spain, 2004*, pp. 653–662.

Rankine, W. (1864). "XXXIII. Summary of the properties of certain stream-lines". In: *The London, Edinburgh, and Dublin Philosophical Magazine and Journal of Science* 28.189, pp. 282–288.

Ranz, William E. (1979). "Applications of a Stretch Model to Mixing , Diffusion , and Reaction in Laminar and Turbulent Flows". In: *The American Institute of Chemical Engineers* 25.1, pp. 41–47.

Renard, Philippe and Ghislain de Marsily (1997). "Calculating equivalent permability: a review". In: *Advances in Water Resources* 20.5-6, pp. 253–278.

Rezaei, Mohsen et al. (2005). "Reactive transport modeling of calcite dissolution in the fresh-salt water mixing zone". In: *Journal of Hydrology* 311, pp. 282–298. DOI: 10.1016/j.jhydrol.2004.12.017.

R.K. Stoessell, W.C. Ward, B.H. Ford, J.D Schuffert (1989). "Water Chemistry and CaCO3 dissolution in the saline part of an open flow mixing zone, coastal Yucatan Peninsula, Mexico". In: *Geological Society of America Bulletin* 101, pp. 159–169.

Robinson, C et al. (2007). "Salt-freshwater dynamics in a subterranean estuary over a spring-neap tidal cycle". In: *Journal of Geophysical Research* 112.June, pp. 1–15. DOI: 10.1029/2006JC003888.

Robinson, C. et al. (2009). "Tidal influence on BTEX biodegradation in sandy coastal aquifers". In: *Advances in Water Resources* 32.1, pp. 16–28. ISSN: 03091708. DOI: 10.1016/j.advwatres.2008.09.008. URL: http://dx.doi.org/10.1016/j.advwatres.2008.09.008.

Robinson, G., G. A. Hamill, and Ashraf A. Ahmed (2015). "Automated image analysis for experimental investigations of salt water intrusion in coastal aquifers". In: *Journal of Hydrology* 530, pp. 350–360. ISSN: 00221694. DOI: 10.1016/j.jhydrol.2015.09.046. URL: http://dx.doi.org/10.1016/j.jhydrol.2015.09.046.

Robinson, G., Ashraf A. Ahmed, and G. A. Hamill (2016). "Experimental saltwater intrusion in coastal aquifers using automated image analysis: Applications to homogeneous aquifers". In: *Journal of Hydrology* 538, pp. 304–313. ISSN: 00221694. DOI: 10.1016/j.jhydrol.2016.04.017. URL: http://dx.doi.org/10.1016/j.jhydrol.2016.04.017.

Rolle, Massimo and Tanguy Le Borgne (2019). "Mixing and Reactive Fronts in the Subsurface". In: *Reviews in Mineralogy and Geochemistry* 85.1, pp. 111–142. ISSN: 1529-6466. DOI: 10.2138/rmg.2018.85.5.

Rolle, Massimo et al. (2009). "Enhancement of dilution and transverse reactive mixing in porous media: Experiments and model-based interpretation". In: *Journal of Contaminant Hydrology* 110.3-4, pp. 130–142. ISSN: 01697722. DOI: 10.1016/j.jconhyd.2009.10.003. URL: http://dx.doi.org/10.1016/j.jconhyd.2009.10.003.

Rolle, Massimo et al. (2012). "Experimental Investigation and Pore-Scale Modeling Interpretation of Compound-Specific Transverse Dispersion in Porous Media". In: *Transport in Porous Media* 93.3, pp. 347–362. ISSN: 01693913. DOI: 10.1007/s11242-012-9953-8.

Rose, A. L. and T. D. Waite (2001). "Chemiluminescence of luminol in the presence of iron(II) and oxygen: Oxidation mechanism and implications for its analytical use". In: *Analytical Chemistry* 73.24, pp. 5909–5920. ISSN: 00032700. DOI: 10.1021/ac015547q.

Sakamoto-Arnold, Carole M and Kenneth S Johnson (1987). "Determination of Picomolar Levels of Cobalt in Seawater by Flow Injection Analysis with Chemiluminescence Detection". In: *Analytical Chemistry* 59, pp. 1789–1794.

Sanchez-Vila, Xavier, Alberto Guadagnini, and Jesus Carrera (2006). "Representative hydraulic conductivities in saturated grqundwater flow". In: *Reviews of Geophysics* 44.3, pp. 1–46. ISSN: 87551209. DOI: 10.1029/2005RG000169.

Sanford, Ward E. and Leonard F. Konikow (1989). "Simulation of Calcite Dissolution and Porosity Changes in Saltwater Mixing Zones in Coastal Aquifers". In: *Water Resources Research* 25.4, pp. 655–667.

Schincariol, Robert A., Edward E. Herderick, and Franklin W. Schwartz (1993). "On the application of image analysis to determine concentration distributions in laboratory experiments". In: *Journal of Contaminant Hydrology* 12.3, pp. 197–215. ISSN: 01697722. DOI: 10.1016/0169-7722(93)90007-F.

Sebben, Megan L., Adrian D. Werner, and Thomas Graf (2015). "Seawater intrusion in fractured coastal aquifers: A preliminary numerical investigation using a fractured Henry problem". In: *Advances in Water Resources* 85, pp. 93–108. ISSN: 03091708. DOI: 10.1016/j.advwatres.2015.09.013. URL: http://dx.doi.org/10.1016/j.advwatres.2015.09.013.

Simmons, C. T., M. L. Pierini, and J. L. Hutson (2002). "Laboratory investigation of variable-density flow and solute transport in unsaturated - Saturated porous media". In: *Transport in Porous Media* 47.2, pp. 215–244. ISSN: 01693913. DOI: 10.1023/A:1015568724369.

Simmons, Craig T, Thomas R Fenstemaker, and John M Sharp (2001). "Variable-density groundwater flow and solute transport in heterogeneous porous media : approaches , resolutions and future challenges". In: *Journal of Contaminant Hydrology*, pp. 245–275.

Singh, Kripa Shankar et al. (2006). "Tracer Studies in Laboratory Beach Simulating Tidal Influences". In: *Journal of Environmental Engineering* 9372.2006, p. 9372. ISSN: 07339372. DOI: 10.1061/(ASCE)0733-9372(2006)132.

Slomp, Caroline P and Philippe Van Cappellen (2004). "Nutrient inputs to the coastal ocean through submarine groundwater discharge : controls and potential impact". In: *Journal of Hydrology* 295, pp. 64–86. DOI: 10.1016/j.jhydrol.2004.02.018.

Smart, P. L., J. M. Dawans, and F. Whitaker (1988). "Carbonate dissolution in a modern mixing zone". In: *Nature* 335.6193, pp. 811–813. ISSN: 00280836. DOI: 10.1038/335811a0.

Souzy, Mathieu (2017). "Mixing lamellae in a shear flow". In: *Journal of Fluid Mechanics* December. DOI: 10.1017/jfm.2017.916.

Spiteri, C. et al. (2006). "pH-Dependent iron oxide precipitation in a subterranean estuary". In: *Journal of Geochemical Exploration* 88.1-3 SPEC. ISS. Pp. 399–403. ISSN: 03756742. DOI: 10.1016/j.gexplo.2005.08.084.

Spiteri, Claudette et al. (2008a). "Flow and nutrient dynamics in a subterranean estuary (Waquoit Bay , MA , USA): Field data and reactive transport modeling". In: *Geochimica et Cosmochimica Acta* 72.3, pp. 3398–3412. DOI: 10.1016/j.gca.2008.04.027.

Spiteri, Claudette et al. (2008b). "Modeling biogeochemical processes in subterranean estuaries : Effect of flow dynamics and redox conditions on submarine groundwater discharge of nutrients". In: *Water Resources Research* 44, pp. 1–18. DOI: 10.1029/2007WR006071.

Steinich, Birgit, Oscar Escolero, and Luis E. Marín (1998). "Salt-water intrusion and nitrate contamination in the Valley of Hermosillo and El Sahuaral coastal aquifers, Sonora, Mexico". In: *Hydrogeology Journal* 6.4, pp. 518–526. ISSN: 14312174. DOI: 10.1007/s100400050172.

Strack, O. D. L. (1976). "A Single-Potential Solution for Regional Interface Problems in Coastal Aquifers". In: *Water Resources Research* 12.6.

Swarzenski, P W, M Charette, and C Langevin (2004). "An autonomous, electromagnetic seepage meter to study coastal groundwater/surface-water exchange". In: *Open File Report* 1369.September, pp. 1–4.

Tamio Takasu, Keisure Maekawa, Atsushi sawada (2008). "Saltwater-freshwater interface behavior for homogeneous and double layer porous media filled with different size of glass beads". In: *JAEA-Research*.

Tartakovsky, A. M., G. D. Tartakovsky, and T. D. Scheibe (2009). "Effects of incomplete mixing on multicomponent reactive transport". In: *Advances in Water Resources* 32.11, pp. 1674–1679. ISSN: 03091708. DOI: 10.1016/j.advwatres.2009.08.012. URL: http://dx.doi.org/10.1016/j.advwatres.2009.08.012.

Tóth, József (2009). *Gravitational Systems of Groundwater Flow: Theory, Evaluation, Utilization*. Cambridge University Press. ISBN: 9780511576546. DOI: https://doi.org/10.1017/CBO9780511576546.

Ullman, William J. et al. (2003). "Groundwater mixing, nutrient diagenesis, and discharges across a sandy beachface, Cape Henlopen, Delaware (USA)". In: *Estuarine, Coastal and Shelf Science* 57.3, pp. 539–552. ISSN: 02727714. DOI: 10.1016/S0272-7714(02)00398-0.

Valiela, Ivan et al. (1990). "Transport of groundwater-borne nutrients from watersheds and their effects on coastal waters". In: *Biogeochemistry* 10.7418, pp. 177–197.

Valocchi, Albert J., Diogo Bolster, and Charles J. Werth (2018). "Mixing-Limited Reactions in Porous Media". In: *Transport in Porous Media*. ISSN: 15731634. DOI: 10.1007/s11242-018-1204-1. URL: https://doi.org/10.1007/s11242-018-1204-1.

Villermaux, E. and J. Duplat (2006). "Coarse grained scale of turbulent mixtures". In: *Physical Review Letters* 97.14, pp. 4–7. ISSN: 00319007. DOI: 10.1103/PhysRevLett.97.144506.

Villermaux, Emmanuel (2012). "Mixing by porous media". In: *Comptes Rendus - Mecanique* 340.11-12, pp. 933–943. ISSN: 16310721. DOI: 10.1016/j.crme.2012.10.042. URL: http://dx.doi.org/10.1016/j.crme.2012.10.042.

— (2019). "Mixing Versus Stirring". In: August 2018, pp. 245–273.

Volker, R E and K R Rushton (1982). "AN ASSESSMENT OF THE IMPORTANCE OF SOME PARAMETERS and location of this zone must be known and they can be predicted by com- bining a convective-dispersion equation for salt transport

with a groundwater flow equation . Relations between fluid properties a". In: 56, pp. 239–250.

Voss, C. I. and A.M Provost (2002). *A model for saturated-unsaturated variable-density ground-water flow with solute or energy transport*. Tech. rep., p. 250.

Voss, Clifford I and William R Souza (1987). "Variable density flow and solute transport simulation of regional aquifers containing a narrow freshwater-saltwater transition zone". In: *Water Resources Research* 23.10, pp. 1851–1866.

Wang, Jun Zhi et al. (2014). "An analytical study on groundwater flow in drainage basins with horizontal wells". In: *Hydrogeology Journal* 22.7, pp. 1625–1638. ISSN: 14350157. DOI: 10.1007/s10040-014-1146-9.

Weiss, John (1991). "The dynamics of enstrophy transfer in two-dimensional hydrodynamics". In: *Physica D: Nonlinear Phenomena* 48.2-3, pp. 273–294. ISSN: 01672789. DOI: 10.1016/0167-2789(91)90088-Q.

Werner, Adrian D. and Craig T. Simmons (2009). "Impact of sea-level rise on sea water intrusion in coastal aquifers". In: *Ground Water* 47.2, pp. 197–204. ISSN: 0017467X. DOI: 10.1111/j.1745-6584.2008.00535.x.

Werner, Adrian D et al. (2012). "Seawater intrusion processes, investigation and management: Recent advances and future challenges". In: *Advances in Water Resources*. ISSN: 0309-1708. DOI: 10.1016/j.advwatres.2012.03.004. URL: http://dx.doi.org/10.1016/j.advwatres.2012.03.004.

Werth, Charles J, Olaf A Cirpka, and Peter Grathwohl (2006). "Enhanced mixing and reaction through flow focusing in heterogeneous porous media". In: 42.August 2005, pp. 1–10. DOI: 10.1029/2005WR004511.

Willingham, Thomas W., Charles J. Werth, and Albert J. Valocchi (2008). "Evaluation of the effects of porous media structure on mixing-controlled reactions using pore-scale modeling and micromodel experiments". In: *Environmental Science and Technology* 42.9, pp. 3185–3193. ISSN: 0013936X. DOI: 10.1021/es7022835.

Wooding, R. A. et al. (1997). "Convection in groundwater below an evaporating salt lake: 2. Evolution of fingers or plumes". In: *Water Resources Research* 33.6, pp. 1219–1228. ISSN: 00431397. DOI: 10.1029/96WR03534.

Wright, Stuart F, Ivan Zadrazil, and Christos N Markides (2017). *A review of solid – fluid selection options for optical - based measurements in single - phase liquid , two - phase liquid – liquid and multiphase solid – liquid flows*. Vol. 58. 9. Springer Berlin Heidelberg, pp. 1–39. ISBN: 0034801723. DOI: 10.1007/s00348-017-2386-y.

Xiaolong Geng, James W. Heiss, Holly A. Michael, Michel Boufadel (2017). "Subsurface Flow andMoisture Dynamics in Response to SwashMotions: Effects of Beach Hydraulic Conductivity and Capillarity". In: *Water Resources Research* 2001, pp. 317–335. DOI: 10.1002/2017WR021248.

Xin, Pei et al. (2015). "Nonlinear interactions of waves and tides in a subterranean estuary". In: *Geophysical Research Letters* 42. DOI: 10.1002/2015GL063643.Received.

Ye, Yu et al. (2015). "Experimental investigation of compound-specific dilution of solute plumes in saturated porous media: 2-D vs. 3-D flow-through systems". In: *Journal of Contaminant Hydrology* 172, pp. 33–47. ISSN: 18736009. DOI: 10.1016/j.jconhyd.2014.11.002.

Yoshihiro Oda, Tamio Takasu, Hirashi Sato, Atsushi Sawada, Takanori Watahiki (2010). "Optical measurement of the salinity distribution by saltwater intrusion experiment". In: *Japan Society of Civil Engineers* 67.2, pp. 186–197.

Zhang, Qi, Ray E Volker U, and David A Lockington (2002). "Experimental investigation of contaminant transport in coastal groundwater". In: *Advances in Environmental Research* 6, pp. 229–237.

Zhao, Lijun et al. (2007). "A sensitive chemiluminescence method for determination of hydroquinone and catechol". In: *Sensors* 7.4, pp. 578–588. ISSN: 14248220. DOI: 10.3390/s7040578.

Zheng, Yanling et al. (2016). "Tidal pumping facilitates dissimilatory nitrate reduction in intertidal marshes". In: *Scientific Reports* 6, pp. 1–12. ISSN: 20452322. DOI: 10.1038/srep21338. URL: http://dx.doi.org/10.1038/srep21338.

Zinn, Brendan and Charles F. Harvey (2003). "When good statistical models of aquifer heterogeneity go bad: A comparison of flow, dispersion, and mass transfer in connected and multivariate Gaussian hydraulic conductivity fields". In: *Water Resources Research* 39.3, pp. 1–19. ISSN: 00431397. DOI: 10.1029/2001WR001146. URL: http://doi.wiley.com/10.1029/2001WR001146.